ACADEMIA MILITAR
MILITARY ACADEMY

FACULTY OF CIVIL ENGINEERING
CTU IN PRAGUE

Analysis of the performance of laminated glass against explosions

João António Lages Picão dos Penedos

Dissertation to obtain the Master of Science Degree in

Military Engineering

Advisors:	Lt. Col. Eng. Pedro José da Silva Gonçalves Matias
	Prof. Ing. Bc. Radoslav Sovják, Ph.D., LL.M.
	Ing. Petr Hála, Ph.D.

Examination Committee

Chairperson:	Prof. Associada Paula Manuela Dos Santos Lopes Do Rego Figueiredo
Course Director and Advisor:	Lt. Col. Eng. Pedro José da Silva Gonçalves Matias
Advisor:	Ing. Petr Hála, Ph.D.
Committee Member:	Prof. Dr. Hugo Bento Rebelo

December 2024

Declaration

I declare that this document is an original work of my own authorship and that it fulfils all the requirements of the Code of Conduct and Good Practices of the Military Academy.

Acknowledgements

First and foremost, I would like to express my deepest gratitude to my supervisors—Lieutenant Colonel Engineer Pedro José da Silva Gonçalves Matias, Professor Ing. Bc. Radoslav Sovják, Ph.D., LL.M., and Ing. Petr Hála, Ph.D.—for their invaluable guidance and support throughout this project.

Lieutenant Colonel Engineer Pedro Matias made the field experiments possible and provided approval and encouragement for my participation in the Erasmus program for my MSc dissertation. His leadership and support were instrumental in the success of this project.

Professor Radoslav Sovják warmly welcomed me and accepted me as his student at the Czech Technical University, facilitating my stay in Prague and strengthening the partnership with the Military Academy.

Ing. Petr Hála hosted me in Prague and was a major contributor to this research by providing extensive knowledge in the field of glass and numerical simulations. His support during my stay motivated and encouraged me to continue pursuing research in this area.

My appreciation goes to the entire team at CCPI - Captain Engineer José Matos, Staff Sergeant Engineer Alexander Oliveira, Professor Hugo Rebelo, and Second Lieutenant Engineer Francisco Novais - for supporting me during the experimental campaign, especially considering the highly complex systems and specialized high-end software used.

I would also like to acknowledge the work done by Lieutenant Engineer Martins and Lieutenant Engineer Machado for their assistance at the beginning of this project. Their combined efforts in numerical simulations and experimental campaigns during their MSc dissertations laid the foundation upon which I built my own work, helping me understand the crucial aspects that needed to be addressed.

I am thankful to the Faculty of Civil Engineering at the Czech Technical University for welcoming me as a student and providing the necessary resources for my research.

I am grateful to the Military Academy Erasmus office, particularly Colonel Infantry Paulo Machado and Professor Sofia Menezes, for approving and accrediting the partnership between these two institutions and facilitating communication between them.

To all my fellow engineers of the FOXTROT 18/19 class, thank you for your companionship and the shared struggles during our course.

I am also grateful to all those who crossed paths with me, understood my work, and offered their support.

Finally, my deepest gratitude goes to my family and my girlfriend for teaching me to be a good person, supporting me through challenging times, and continually pushing me to achieve excellence throughout my life. Their unwavering support has allowed me to be where I am today.

Abstract

This dissertation investigates the performance of laminated glass against explosions, focusing on the dynamic response of glass panels subjected to blast loads. The study aims to assess the behaviour of glass panels under the effect of blast waves and is part of the project "SAERFA - Energy Absorption Systems Using Additive Manufacturing". Then, in a subsequent phase of the project a system that can absorb energy and mitigate the effects of the blast wave will be developed.

For this work, two experimental campaigns were conducted. First, an experimental campaign using a shock tube to characterize the action of the blast wave, where pressure and impulse data were collected. Then, an experimental campaign was conducted using the same shock tube with laminated glass samples of different thicknesses to determine their behaviour under blast waves.

Afterwards, with all the data collected, numerical models using finite element analysis tools were built. These models helped create pressure-impulse diagrams, providing insights into the failure behaviour of glass subjected to explosions. The agreement between experimental data and numerical results confirms the model's accuracy. The final outcomes demonstrate that laminated glass panels, particularly with increased thickness, can effectively withstand higher blast loads.

Keywords: Blast resistance, Laminated glass, Finite element analysis, Shock tube testing

Resumo

Esta dissertação de mestrado investiga o comportamento do vidro laminado face a explosões, com enfâse na resposta dinâmica de painéis de vidro sujeitos a cargas explosivas. O estudo tem como objetivo avaliar e compreender o comportamento de painéis de vidro sob o efeito de ondas de choque e faz parte do projeto "SAERFA - Sistemas de Absorção de Energia Utilizando Fabricação Aditiva".

Para isso, foram realizadas duas campanhas experimentais. Primeiro, uma campanha experimental que recorreu a um tubo de choque para caracterizar a ação da onda de choque, onde foram recolhidos dados de pressão e impulso. De seguida, foi realizada uma campanha experimental com o mesmo tubo de choque e amostras de vidro laminado de diferentes espessuras para determinar o seu comportamento sob ondas de explosão no tubo de choque.

Posteriormente, com todos os dados recolhidos, foram construídos modelos numéricos usando ferramentas de análise de elementos finitos. Estes modelos ajudaram a criar diagramas de pressão-impulso, fornecendo informações sobre o comportamento de falha do vidro sujeito a explosões. A concordância entre os dados experimentais e os resultados numéricos confirma a precisão do modelo. Os resultados finais demonstram que painéis de vidro laminado, particularmente com maior espessura, podem aguentar com cargas de explosão mais elevadas.

Palavras-chave: Resistência a explosões, Vidro laminado, Análise de elementos finitos, Testes com recurso a tubos de choque.

Content

List of Figures

List of Tables

Abbreviations

CCPI	Centre of Competence for Infrastructure Protection
DIC	Digital Image Correlation
EDST	Explosion Driven Shock Tube
EPDM	Ethylene Propylene Diene Monomer
FAB	Free Air Blast
FEA	Finite Element Analysis
LVDT	Linear Voltage Differential Transducers
OSB	Oriented Strand Board
PVB	Polyvinyl Butyral
SHS	Square Hollow Section
TNT	Trinitrotoluene

Nomenclature

Latin Nomenclature

a	Speed of sound in an ideal gas
b	Waveform parameter
C	Constant for the Kingery and Bulmash equation
C_r	Reflection coefficient
D	EDST equivalent diameter
H^d_{EXP}	Heat of detonation of the explosive
H^d_{TNT}	Heat of detonation of TNT
i_s	Impulse produced by the shock wave
K	Constant for the Kingery and Bulmash equation
M	Mach number
M_x	Mach number for the incident shock
n	Order of the polynomial
p_0	Ambient pressure
p_s	Incident overpressure
p_{s0}	Peak incident pressure
p_{s0}^-	Peak negative overpressure
R	Distance from the centre of detonation
S	EDST cross-sectional area
t_0^-	Negative phase duration
t_0	Positive phase duration
t_a	Arrival time of the shock wave
t_d	Duration of the linear decay
u	Velocity of an ideal gas
W	Charge mass
W_E	Effective charge weight
W_{EXP}	Weight of the explosive
Z	Scaled distance

Greek Nomenclature

α	Incident angle of the blast wave on the reflecting surface
α_i	Incident angle
α_r	Reflected angle
β_{max}	Limiting angle for Mach stem formation

1. Introduction

From ancient medieval castles to modern fortifications, the primary role of construction throughout history has always been, and continues to be, defence. In contemporary society, the increasing prevalence of terrorist activities and accidental explosions has necessitated the design of large civil structures - such as offices and airports - that can accommodate significant numbers of people, with the capacity to protect against a variety of potential threats.

In this context, structural engineers are increasingly focusing on the development of advanced systems designed to protect individuals from explosions. A major concern today revolves around the use of glazing in buildings. In the event of an explosion, glass can shatter, posing severe risks to human safety, including injuries or fatalities.

The use of glazing in construction has become ubiquitous in modern architecture. For instance, the facade of The Shard in London, seen in **Figure 1**, is primarily composed of glass panels, making it a prominent example of contemporary glass architecture. Similarly, the Louvre Pyramid in Paris seen in **Figure 2** serves as an iconic structure demonstrating the widespread use of glass in modern construction. The primary goal of such designs is to enhance the quality of life and well-being of building occupants by providing visual connectivity with the exterior environment, which is recognized as an important psychological benefit [1].

Figure 1: The Shard [2]

Figure 2: The Louvre Pyramid [3]

Throughout history, various types of glass have been developed, including float glass, which is the most widely used today due to its affordability; heat-strengthened glass; and the more expensive tempered glass, which requires a more complex manufacturing process. The development of different types of interlayers, such as Polyvinyl Butyral (PVB), SentryGlass®, and Ethylene Vinyl Acetate (EVA), has also led to the advancement of laminated glass, which is now a highly effective technical solution. Laminated glass, comprising multiple glass panes bonded together by an interlayer, is currently the most robust solution available for withstanding blast loads, notably when tempered glass panels are used [4].

The knowledge gained from research in this field is crucial for improving the safety and resilience of structures against terrorist attacks and accidental explosions. It informs the development of advanced protective systems, innovative materials, and design guidelines that are essential for mitigating the destructive effects of explosions.

1.1. Proposed problem and motivation

The present study is part of the project "SAERFA - Sistemas de Absorção de Energia com Recurso ao Fabrico Aditivo" ("Energy Absorption Systems Using Additive Manufacturing"), which is under the CINAMIL - Centro de Investigação, Desenvolvimento e Inovação da Academia Militar ("Center for Research, Development, and Innovation of the Military Academy") Projects and is overseen by the Military Academy. The goal of this project is to investigate and propose new solutions for energy absorption systems using additive manufacturing techniques.

To achieve this goal, it is essential to first understand the behaviour of the primary system - laminated glass panels - under explosive loads. These panels are a key component in many structures and are particularly vulnerable to blast effects. By analysing the response of laminated glass to explosions, it becomes possible to identify the specific energy absorption requirements necessary for protection. This master's thesis focuses on analysing the dynamic behaviour of glass panels when subjected to explosive loads.

In future work, the insights gained from this study will be used to develop strategies that employ additive manufacturing to create customized energy-absorbing structures. These structures can be integrated with laminated glass panels, the primary system, to mitigate and absorb the impact of explosions, thereby minimizing damage. Additive manufacturing offers the flexibility to design complex geometries and adaptive material properties, making it an ideal approach for creating innovative energy absorption solutions.

Most of the data required for this study is not publicly available, as much of the information regarding explosions and explosive materials is classified and highly specialized. Handling such materials requires specific qualifications and facilities, making it challenging to obtain experimental data. Additionally, laminated glass, being an innovative material with many variables that can affect its behaviour, poses further difficulties in acquiring the necessary data for numerical simulations.

In light of these challenges, this master's thesis aims to conduct an experimental campaign on glass and develop a numerical simulation to better understand and improve knowledge, thereby enhancing the overall project.

1.2. Objectives and methodology

This dissertation aims to significantly enhance the understanding of the dynamic behaviour of glass panels subjected to blast loads, with the following key objectives:

1. Conduct an Experimental Investigation: Perform a detailed experimental study to observe and quantify the response of laminated glass panels under blast waves. This will involve designed experiments to capture data on the behaviour of glass during explosions.
2. Develop a Numerical Simulation Framework: Create a numerical simulation framework using finite element analysis (FEA) techniques. The framework will be used to simulate the dynamic response of laminated glass panels under various blast scenarios, allowing for the prediction of damage patterns and structural performance.

3. Compare Experimental and Simulated Data: Analyse the consistency and accuracy of the numerical simulations by comparing them with the experimental results. This comparison will help validate the model and identify any discrepancies or areas for improvement, especially in the boundary conditions of the structure that holds the glass.

The methodology of this study begins with the characterization of explosion effects in a controlled laboratory environment using shock tubes. In the next phase, glass panels are subjected to blast loads under the same controlled laboratory conditions. In the third phase, numerical models are developed using predefined parameters and state of the art techniques. In the final phase, the results from the experimental and numerical simulations are compared to validate the numerical models.

1.3. Dissertation outline

This dissertation consists of six chapters. In the first chapter, which includes this subchapter, the framework of the study is presented, along with the methodology and objectives. The second chapter provides a state-of-the-art review, including a brief summary of prior work on the main subject, the characteristics of laminated glass, and the characterization of explosions. The third chapter introduces the numerical analysis program and the definitions applied in the simulations. The fourth chapter describes the experimental campaigns conducted and the results obtained. In the fifth chapter, a comparison is made between the simulation and experimental results, and the findings are thoroughly discussed. Finally, the sixth chapter presents final considerations, conclusions, and proposals for future investigations.

1.4. Dissertation outcomes

During the course of this work, Lt. Colonel Pedro Matias, one of the project's supervisors, presented some of the results from the numerical simulation and experimental campaign at the International Physical Security Forum (IPSF) 2024, held in Brussels in April 2024.

This project helped strengthen the partnership between the Military Academy and the Czech Technical University through the ERASMUS+ program. It also facilitated broader cooperation between institutions, fostering the exchange of knowledge on key themes related to the dissertation.

2. State of the art

2.1. Literature Review

The facade of a building holds significant importance for designers aiming to enhance the security of structures against explosions. The outer layer of the affected building must deter blast waves from penetrating the building interior. Windows are often represented as vulnerable points in a building.

Windows, typically made of glass, are susceptible to potential hazards from glazing during an explosion. Without a proper design, they can fail suddenly, causing fragmentation [5]. Therefore, it is crucial anticipate the effects of a blast wave on glazing. Preserving the integrity of the facade and glazing is paramount, as it ensures the safety of the internal space within the building [6].

In Hopper et al. [4], four open air blast experiments were described, involving laminated glass windows measuring 1500 mm x 1200 mm, composed of two 3 mm annealed glass plies and a 1.52 mm PVB interlayer. The samples were subjected to peak reflected pressures and positive reflected impulses ranging from 91.2 kPa to 155 kPa and 284 kPa ms to 413 kPa ms, respectively. Furthermore, the displacement of the entire glazing was measured using digital image correlation and compared to numerical calculations.

Larcher et al. [7], also conducted experiments on a laminated glass window 890 mm x 1090 mm, composed of two 6 mm heat-strengthened glass plies and a 2.28 mm PVB interlayer. These experiments were carried out in a shock tube, measuring the pressure-time function and the displacement-time function with the assistance of high-speed cameras. The results were then compared to a numerical model performed in EUROPLEXUS, a finite element code for nonlinear dynamic analysis.

In Pelfrene et al. [8], experiments were conducted on the post-breakage performance of different types of PVB interlayers on laminated glass under blast load in a shock tube. Three adhesion levels of common PVB interlayer and one stiffer PVB were tested. The laminate assembly, measuring 900 mm x 1100 mm, consists of two 6 mm annealed glass plies and a 1.52 mm PVB interlayer. The samples were loaded with peak reflected pressures and positive reflected impulses ranging from 47 kPa to 155 kPa and 350 kPa ms to 2000 kPa ms, respectively. The experiments were measured using laser sensors, strain gauges, and high-speed cameras. A numerical model in LS-DYNA [9] was used to reproduce the results obtained from the experiment.

In Zhang et Hao [10], laminated glass panes were tested with different weights of TNT, Trinitrotoluene, at various distances. In this study, were carried on full scale field blasts on glass panes with 1500 mm x 1200 mm constructed with 2 plies of 3mm annealed glass with a 1.52 mm PVB interlayer. The objective was to monitor the failure process and to study the failures modes of laminated panes at joints with window frames. The experimental data was recorded using pressure sensors, mechanical linear voltage differential transducers (LVDT), and high-speed cameras. The responses of laminated glass windows also were examined using a numerical simulation in LS-DYNA.

In Kumar et Shukla [11], a controlled study was conducted on glass panels subjected to an air blast. Five different glass panels were utilized, each measuring 305 mm x 305 mm with a thickness of

6.5 mm. These types included plain, sandwiched, wired, tempered, and sandwiched glass with film on both faces. The latter variant had a thickness of 7.5mm due to the protective film on both faces. To apply the air blast load to the glass panels, a shock tube was employed, that consisted of a long rigid cylinder, with an overall length of 8 meters and a diameter of 0.15 meters, with a final muzzle diameter of 0.07 meters. All glass specimens were subjected to the same incident pressure load of 0.5 MPa. As the laminated sandwich glass panel survived the initial test, it was also tested for a higher incident pressure, 1 MPa, and it was demonstrated that it also withstood this increased pressure. There were transducers inside the shock tube to measure the pressure. Additionally, digital image correlation (DIC) technique was used to analyse the full-field shape and deformation of the glass panels.

In Chen et al. [12], a theoretical method is proposed for establishing iso-damage curves for different levels of damage for framed monolithic glass. The method is verified through comparison with published experimental data and numerical simulation results made by Hooper at al. [4] and Zhang et al. [13]. Based on the observed failure modes from finite element simulations, the pressure asymptote and the impulse asymptote are derived analytically, and the dynamic segment of the curve is established using an empirical approach based on the numerical simulation.

In Zhang et al. [14], a empirical formulae is presented after a parametric study is done to examine the influence of window dimension, interlayer thickness, glass thickness, and boundary conditions on the P–I diagrams for laminated glass. A numerical model in LS-DYNA is used to assess the dynamic response of the laminated glass, and it used experimental results to verify the accuracy of the models.

In Chen et al. [15], there is a development of pressure-impulse diagrams for framed PVB-Laminated glass windows. The diagrams were confirmed based on numerical simulation study and the energy method proposed by Timoshenko and Woinowsky-Krieger [16] with the large deflection of plates. The method was validated through comparison with the published data from Hooper et al. [4].

In Hejazi et Sari [17], an investigation into the failure and post-breakage response of laminated glass with different panels under blast load is conducted. Different modelling techniques of the finite element method were used and compared with field blast tests performed by Larcher et al. [7] and Hooper et al. [4]. This comparison aimed to highlight the capability to predict cracking and its propagation with different modelling techniques.

In Hála et al. [18], a study is conducted to test the behaviour of free-hanging laminated glass subjected to blast loads. This setup allows testing laminated glass without the complications introduced by boundary conditions, providing a stress-free environment. Crack formation and propagation were monitored during the experimental study. This research was undertaken to improve future numerical models of laminated glass under blast load.

In Meyland and Nielsen [19], ongoing research on glass under high strain rates - namely, impact and blast loads - is presented. It also includes numerical models of glass fracture, and a simulation of a small ring-on-ring test setup compared to experimental results, demonstrating their ability to predict fracture strength.

2.2. Laminated Glass

Glass is a material whose use has significantly increased over recent years due to its special characteristics, such as colour, translucency, and transparency. The possibility of creating translucent facades that provide visual contact between building users and the external environment is a very important psychological factor that has a positive impact on the health and quality of life of building users. In recent decades, its scope of application as a structural material has expanded [1,20].

Glass can come in a variety of forms in function of the chemistry and process but most glass used in construction is soda lima silica glass, particularly because silica is one of the most common and inexpensive materials on the planet. Conceptually, glass is a inorganic product of fusion of the raw materials heated and mixed to a melting temperature of approximately 1600ºC, then the molten glass spreads across a tin surface until it reaches the desired thickness at approximately 600ºC, and moves to the annealing lehr, in which the material cools to a rigid condition without crystallization, by a controlled cooling process that minimizes internal material stresses caused by uneven and rapid cooling, as seen in **Figure 3** [20,21].

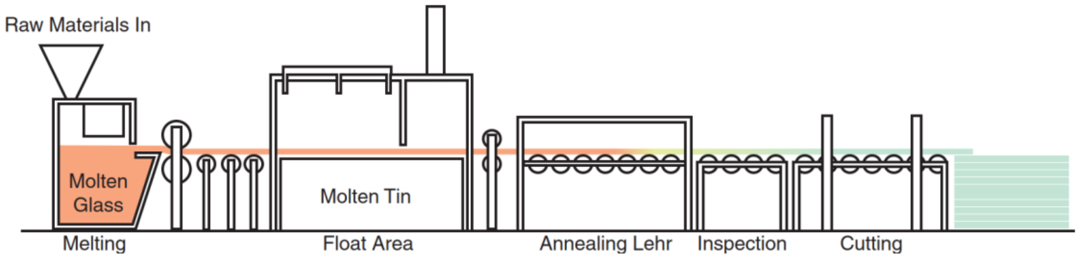

Figure 3: Diagram of the annealed glass process (adapted from [20])

The use of large-area glass panels in areas traditionally reserved for other materials, such as roofs, floors, stairs, and partitions, along with the availability of a wide selection of glass products with enhanced properties and a broad range of new support and connection details, including bolted glass, represent recent architectural trends and technological developments. These provide unprecedented opportunities and significant changes in the use of glass in buildings. As a consequence of these applications, glass is often subjected to complex stress states [21].

For situations where there is a risk of people colliding with the glass, it is necessary to specify the use of glass with special characteristics. This type of glass is characterized by its impact resistance and type of fracture. For glass to be designated as "safety glass", it must meet certain criteria during impact testing. These criteria are: the glass should not break, or if it does break, it should disintegrate into a large number of relatively harmless particles. Alternatively, fractures may occur, but the fragments should not separate, no significant openings should appear, and the amount of detached fragments should be limited [22]. The potential hazards from glazing in an explosion arise from the fragments created when a high blast load meets glass panels. However, with proper design, glass can be manufactured and combined in a way that minimizes fragmentation, ensuring the safety of individuals behind it [5].

2.2.1. Types of Glass

Currently, structural engineers have access to a wide range of glass products and configurations, as well as a broad range of normal and exceptional loading conditions [21]. The subsequent sections provide a comprehensive overview of the different glass types available.

2.2.1.1 Annealed glass

Annealed glass is the standard glass without any tempering on the postprocessing, characterized by brittle fracture due to microscopic irregularities along its surface. This irregularity leads to a wide variation in strength and random crack propagation. Cracking can initiate at a critical flaw anywhere on the surface, resulting in sudden breakage into angular and irregular fragments, posing a high hazard to anyone nearby [5,20].

2.2.1.2 Toughened glass

Toughened glass is produced by reheating annealed glass to a plastic state, followed by controlled cooling. During the thermal tempering process, the glass is heated to approximately to 650ºC in a furnace and then quenched (cooled rapidly) by jets of cold air, as seen in **Figure 4** [5,21].

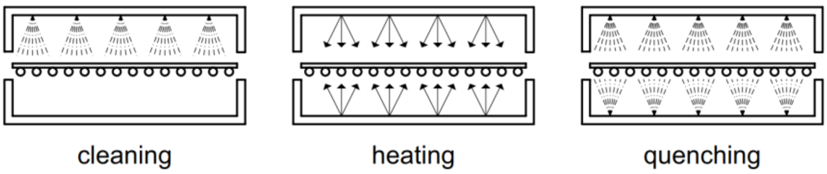

Figure 4: Tempering process adapted from [21]

This process induces permanent stress distribution across the thickness, with compressive stress in both outer faces counterbalanced by tensile stress in the core by solidifying first the surface and then the interior of the glass. This results in a four to six times increase in effective strength compared to annealed glass. However, it still presents a risk to nearby individuals as it breaks into small and edged fragments suddenly [5,21].

2.2.1.3 Heat-strengthened glass

Heat-strengthened glass undergoes a process similar to toughened glass but with reheating at lower temperatures. This reduces compression on the surfaces and material strength compared to toughened glass. Upon fracture, heat-strengthened glass breaks into sharp-edged fragments similar to those of annealed glass, although smaller and more numerous in comparison [5].

2.2.1.4 Laminated glass

Laminated glass is a composite of alternating layers of glass and interlayer material. The interlayer material commonly used for blast resistance is polyvinyl butyral (PVB), a highly ductile plastic layer with significant tensile strength when subjected to high strain rates, except in sub-zero temperatures. PVB exhibits excellent bonding properties to glass, even after the glass fractures, as the fragments of it remain bonded to the PVB. Eventually, PVB failure occurs due to tearing caused by puncturing of the glass fragments or by reaching its failure strength. Due to this mechanism, the performance of PVB laminated glass surpasses that of both annealed and toughened monolithic glass.

The nomenclature of laminated glass specifies the thickness of each glass ply and the number of PVB layers. For example, in the designation "66.4" the first "6" indicates that the first glass ply is 6 mm thick, and the second "6" indicates the same thickness for the second ply. The ".4" signifies four layers of PVB, each 0.38 mm thick, totalling 1.52 mm for the interlayer.

The process of manufacturing laminated glass with PVB is divided into two phases. In the first phase, the glass panels are individually washed, the PVB layer is placed between the panels, and the assembly is heated and pressed (pre-lamination). Subsequently, the bonding of the entire surface is completed in an autoclave, through the use of high pressures and temperatures around 140ºC [23].

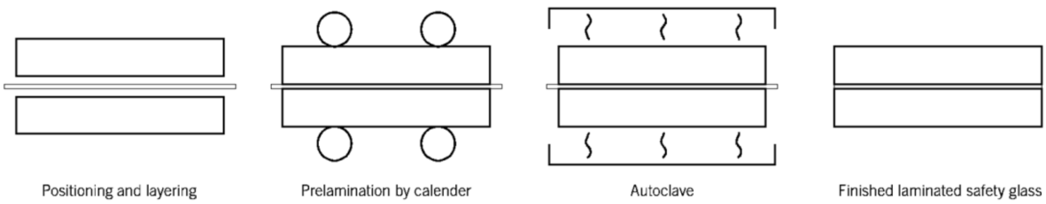

Figure 5: Laminated glass manufactreing process (adapted from [23])

Laminated glass proven to be effective at mitigating risks and is frequently employed to protect building occupants by retaining glass fragments on a PVB interlayer upon fracture, as seen in **Figure 6** [4,5].

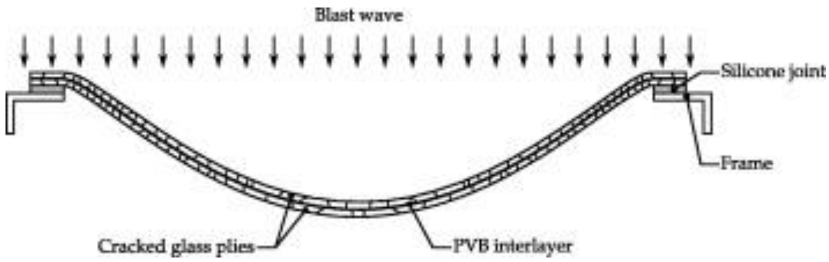

Figure 6: Postcrack deformation in laminated glass due to blast loading (adapted from [4])

Various interlayers can be used in specific applications where PVB may have drawbacks. One example is the use of polyurethane in aircraft windshields, as polyurethane offers similar ductility and strength properties while remaining ductile at sub-zero temperatures, though as a more costly option [5].

The behaviour of a laminated glass sheet is described by a five phase step, as seen in **Figure 7**:

(1) Elastic behaviour of the glass plies.
(2) The first glass ply is broken, while the other remains intact; the interlayer is undamaged.
(3) The second glass ply fails; the interlayer behaves elastically.
(4) The interlayer behaves plastically, keeping the fragments together due to the bonding properties of the interlayer.
(5) The interlayer fails by reaching its failure strength or by being cut by the splinters.

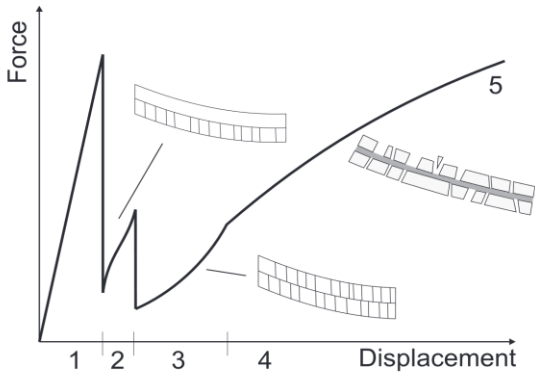

Figure 7: Schematic failure of laminated glass (adapted from [7])

2.2.2. Glass Connections

Connecting glass to other materials requires careful consideration to avoid direct contact with harder substances that could damage the glass. Intermediate materials such as plastics, resins, neoprene, or gaskets are typically used to protect the glass surface. Recent developments have introduced new connection methods that allow higher loads to be transmitted to glass. There is also the possibility to use chemical or glued connections in glass, although issues like durability of the adhesive joints remain a concern. These connections are generally categorized into mechanical fixings and adhesive fixings [21].

Mechanical fixings affect the stress distribution in glass, and it is recommended to distribute the load evenly to use the glass efficiently. A common method is linearly supported glazing, which is mostly used in framed constructions, where glass panels are supported along two or four edges using materials like neoprene or Ethylene Propylene Diene Monomer (EPDM) rubber [24]. This system allows for movement due to temperature changes and distributes lateral loads through the supporting frame. Another mechanical fixing is the use of clamped or friction grip fixings that can significantly reduce the visual impact of linearly supported frames or pressure cap profiles because the glass panel edges are fixed to the substructure at discrete locations with clamps [21].

Adhesive fixings offer a more uniform load distribution, reducing stress concentrations. Soft elastic adhesives like structural silicone sealants bond the glass to other materials, providing flexibility and energy absorption. These sealants have a low modulus of elasticity, which reduces stress concentrations but are not suitable for transferring high shear forces. Rigid adhesives, such as modified acrylics cured with ultraviolet light, offer strong bonds with minimal visual impact but have limited capacity to absorb deformation [21,25].

2.3. Explosions

This chapter defines an explosion and the environment in which it occurs. An explosion is the rapid release of energy that generates a pressure wave in the surrounding medium, such as air. The disturbance caused by this energy release results in high-pressure waves that spread outward, leading to varying levels of impact depending on the surroundings [26].

Explosions can originate from various energy sources. A physical explosion occurs when compressed gas is suddenly released, generating pressure waves. Similarly, nuclear explosions result from the redistribution of protons and neutrons in an atomic nucleus, releasing a violent amount of energy and creating powerful pressure waves. Each source contributes to the different types of explosive events, all of which involve the rapid propagation of pressure through a medium [5,26].

As for the rapid oxidation of fuel elements, composed of carbon and hydrogen atoms, primarily results in the evolution of heat and the production of gas, which rapidly expands and generates shock pressure waves. This type of explosion is known as a chemical explosion, which is a high-speed chemical reaction that generates blast waves through rapid changes in air pressure [5]. That chemical reaction induces changes on the surrounding ambient depending on the type of explosive used and the distance from the objects close to it. The type of explosive material affects directly the magnitude of the explosion and it is usually measured in equivalent weight of TNT, although it is not an exact way of estimating blast for explosives [26].

2.3.1. Chemical explosion

For a chemical reaction to occur, oxygen needs to be present, however, it is already within the compound, so there is no need for the presence of air. This compound is mostly condensed, existing either in a solid state or liquid [5]. This reaction can be classified into three different types: combustion, deflagration, and detonation.

Combustion generally occurs when there is an oxidation reaction, either with air from within the compound or from the external environment. In general terms, it happens when electrons transfer from one atom to another, without being gained back.

Deflagration is when the explosive material decomposes at a speed lower than the speed of the sound of the material. It propagates by realising heat to the surroundings, in the opposite direction of the decomposition. Explosives that deflagrate are termed as propellants or low explosives. One example is cordite, a mixture of nitrocellulose and nitro-glycerine .

Detonation occurs when the combustion waves are faster than the speed of the sound of the material [30]. This produces a high-pressure shock wave with high temperatures. This chemical reaction passes through the exploding material at speeds of 1 to 10 km/s, exceeding the sonic velocity (0.343 Km/s) [29]. Explosives that usually detonate are named as high explosives, with one example being TNT.

2.3.2. TNT equivalent

The use of TNT as the standard reference to obtain the scaled distance in equation (2.1) is the first step in converting sources other than TNT to the actual mass of the chare into a TNT equivalent mass, using a conversion factor based on its specific energy [5].

To obtain Z, the scaled distance in meters, it is necessary to use R, the distance from the centre of the detonation in meters, and W, the charge mass expressed in kilograms of TNT in the standard atmosphere [5].

$$Z = \frac{R}{W^{\frac{1}{3}}} \tag{2.1}$$

One approach is to follow the equivalency factors proposed by Baker et al. [31], as shown in **Table 1**. There is a significant difference between the TNT equivalence regarding its evaluation, since if the objective is to assess the overpressure usually the values for the TNT equivalent are bigger than if the objective was to assess the impulse [32].

Table 1: Conversion factors for explosives adapted from [31,33,34]

Explosive	Mass specific energy (Q_x: (kJ/kg))	TNT equivalent: ($Q_x = Q_{TNT}$)	
		Peak Pressure	**Impulse**
PE-4A	5800	1.40	1.20
PETN	5800	1.27	1.11
HMX	5680	1.02	1.03
RDX (cyclonite)	5360	1.14	1.09
Compound B (60% RDX 40% TNT)	5190	1.11	0.98
C4 (91% RDX)	4870	1.37	1.19
TNT	4520	1.00	1.00

Another approach described by the US Army Corps of Engineers [35] makes use of the heat detonation of various materials. The following equation is associated mostly with the shock effects of unconfined detonations and spherical charges [35]:

$$W_E = \frac{H_{EXP}^d}{H_{TNT}^d} W_{EXP} \tag{2.2}$$

where W_E (kg) is the effective charge weight, W_{EXP} (kg) is the weight of the explosive in question, H^d_{EXP} (J/kg) is the heat of detonation of the explosive in question, and H^d_{TNT} (J/kg) is the heat of detonation of TNT.

If the charge is not spherical, the explosive should be subdivided into several segments of equal size. Then, the effect of the reflected impulse must be determined by multiplying the individual impulse by the total number of segments [35].

There can be multiple unknown factors, especially in improvised explosives, such as unexpected shock wave reflections, variability of formulation, and the quality of control used in manufacturing. To compensate for these unknown, the US Army Corps of Engineers [35], recommends that the TNT equivalent weight be increased by 20%.

2.3.3. Type of explosions

Blast loads on structures induced by high explosives can be categorized according to their confinement including confined and unconfined, as well as the location of the explosion relative to the acceptor structures [35–37].

A free-air burst explosion is an unconfined explosion where the blast wave happens in the open-air and spreads from the detonation source to the acceptor structure without significant wave amplification. Reflected waves occur when blast wave front strikes the building [36,37], as illustrated in **Figure 8**.

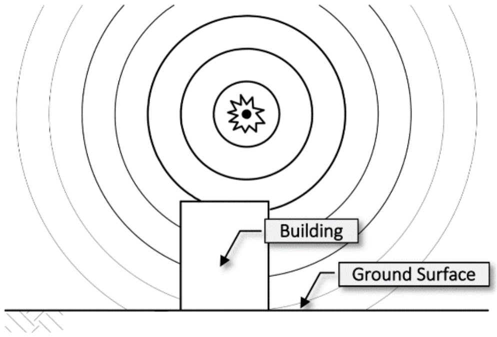

Figure 8: Free-air burst explosion [37]

An air burst occurs explosion's height is limited to two or three times the height of a one-storey or two-storey structure [35]. In this case, blast wave amplification occurs due to the ground reflecting the initial wave before it reaches the structure [36], as shown in **Figure 9**. When the initial wave interacts with the reflected wave, they form a joint front wave called the Mach stem. The height of the Mach stem increases as the wave moves away from the detonation centre [37].

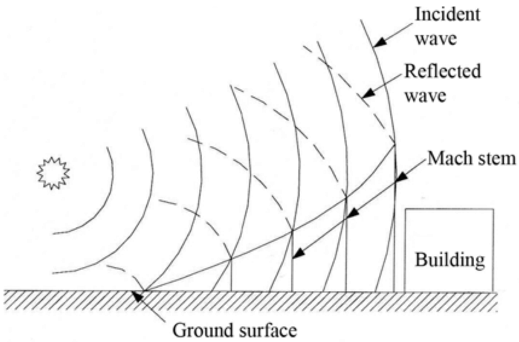

Figure 9: An air burst with ground reflections [37]

A surface burst explosion occurs when the detonation happens close to or on the ground, causing significant amplification of the initial due to ground reflections, as depicted in **Figure 10**. In contrast to an air burst, the incident and reflected waves converge at the point of detonation, forming a single wave, akin in nature to the Mach stem of an air burst [37].

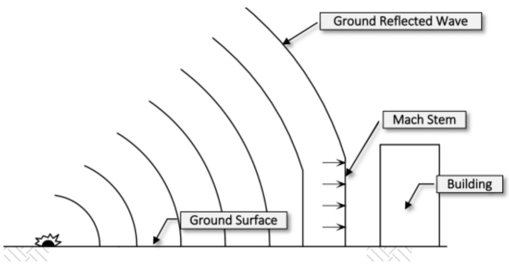

Figure 10: Surface burst explosion adapted from [37]

In the event of an explosion occurring inside a building, the peak pressure of the initial wave will be amplified by reflections within the structure. Depending on the degree of confinement, the high temperatures and gas products from the chemical process involved in the detonation will cause additional pressures and increase the load duration within the building [35–37].

A fully vented confined explosion occurs when the detonation takes place adjacent to a barrier with one or more surfaces open to the atmosphere. The initial shock wave, amplified by reflections on the barrier, is almost instantaneously vented to the atmosphere, propagates away from the structures [35,37], as depicted in **Figure 11**.

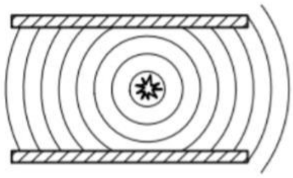

Figure 11: Fully vented confined explosion adapted from [37]

A partially vented confined explosion occurs when the surfaces open to the atmosphere are more limited compared to the fully vented confined explosion. The products of this detonation take longer to be vented to the atmosphere, resulting in a high buildup of pressure over a finite period of time [35,37], as illustrated in **Figure 12**.

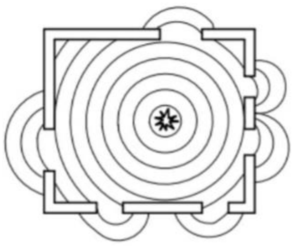

Figure 12: Partially confined explosion adapted from [37]

A fully confined explosion corresponds to complete or near-total containment of the explosion by a barrier. The shock wave will have prolonged duration, dependent on the degree of confinement [35,37], as shown in **Figure 13**.

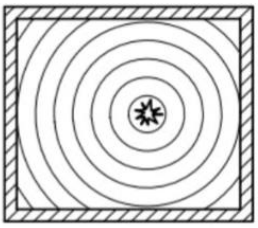

Figure 13: Fully confined explosion adapted from [37]

2.3.3.1 Shock wave reflection

Shock wave reflection occurs when a blast wave encounters a solid surface made of a denser material than the transmitting wave, leading to reflections. These reflections, particularly in built-up environments, create complex conditions that can amplify the shock fronts, resulting in high-magnitude shock waves. Reflection is a complex behaviour in the characterization of an explosive shock wave, and this phenomenon can manifest in three types [37–39]: face-on, regular and Mach reflections.
These types are depend on factors such as the incident angle of the blast wave on the reflecting surface, (α), the incident overpressure of the blast wave, the ambient pressure of the air, and the type of reflecting

surface. By convention, the angle of incidence is defined as zero when the blast impinges normally upon the surface, referred to as face-on reflection. When α is at 90º, there is no reflection, and the surface experiences the incident overpressure, or side-on pressure. Regular reflection occurs between and incident of 0º and approximately 40º in air, beyond which Mach reflection takes place [5].

2.3.3.2 Face-on reflection

This type of reflection occurs when a blast wave strikes an unyielding surface with the plane of shock front parallel to that surface, as shown in **Figure 14** [37].

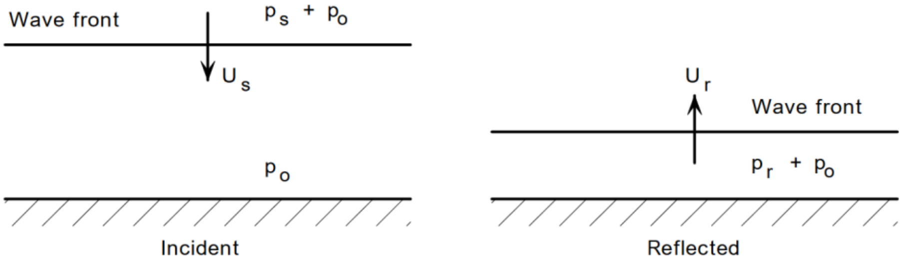

Figure 14: Normal or face-on reflection of a blast wave adapted from [37]

When this happens, the movement of particles at the shock plane is abruptly terminated. These molecules are compressed by the trailing pressure wave, leading to reflected overpressure greater in magnitude than the incident [37,39]. The pressure-time profile for a reflected wave is depicted in **Figure 15**.

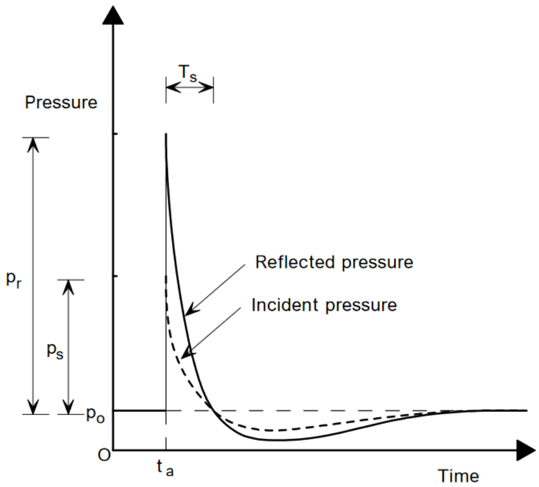

Figure 15: Pressure-time profile for a face-on reflected wave adapted from [37]

It can be observed that the increase in blast overpressure causes an increase in the impulse of the blast wave. On the other hand, time durations remain unaltered [37].

2.3.3.3 Regular reflection

Regular or oblique reflection occurs when the shock wave impinges at near head-on incidence onto an unyielding surface, as shown in the **Figure 16**.

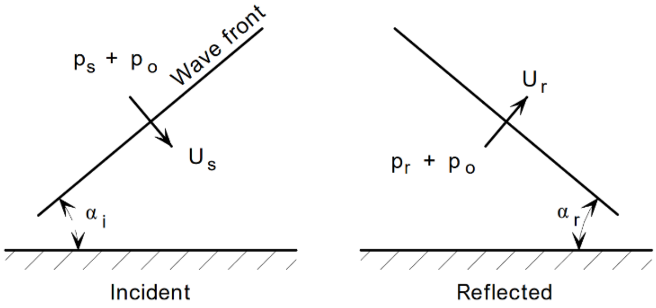

Figure 16: Regular reflection of a blast wave [37]

The reflected angle, α_r, does not equal the incident angle, α_i. However, if the incident angle increases, the reflected angle also increases, behaving similarly to sound waves, hence the term "regular" [37–39]. Regular reflection exhibits reflection coefficients, C_r, dependent on the incident overpressure, p_s, and the reflected overpressure , p_r, as illustrated in **Figure 17** and given by the equation (2.3).

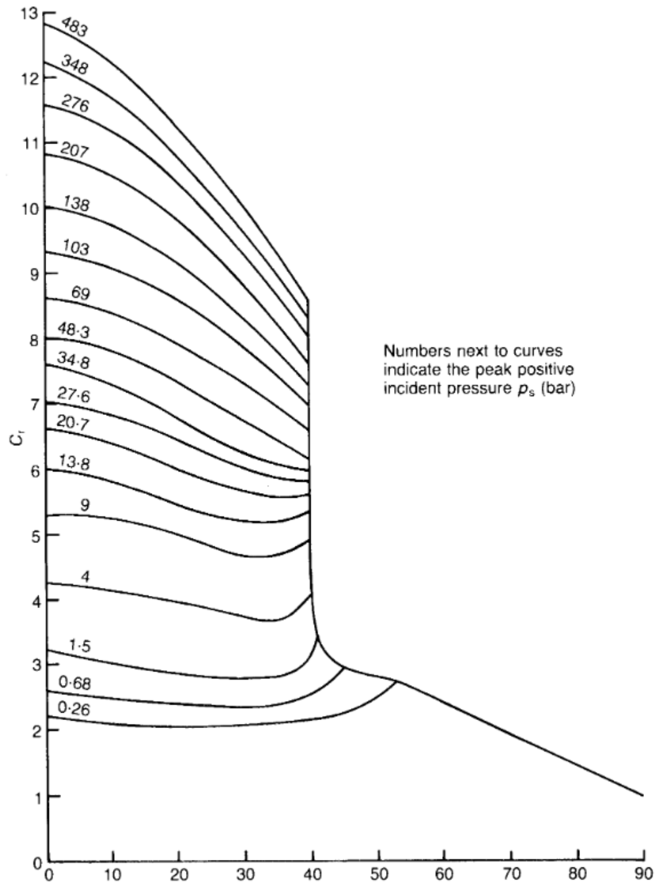

Figure 17: Reflection coefficient vs angle of incidence for varying values of incident overpressure [37,39]

$$C_r = \frac{p_r}{p_i} \tag{2.3}$$

The peak reflected overpressure on equation (2.3) depends on the magnitude of the peak incident overpressure. As seen in **Figure 17**, for values of α_i up to 40º, the peak incident overpressure lies between 2 and 13 times [37].

2.3.3.4 Mach reflection

As mentioned before, when the incident angle exceeds the limiting angle in air of 40º, regular reflection is replaced by Mach reflection. The mechanism behind this reflection is the result of the reflected wave catching up with the incident wave. Because the reflected wave cannot overtake the incident wave, it creates a third wavefront called the Mach Stem. The point where the three waves converge is called the triple point, and the region behind it is a slipstream region where different densities and particles velocities exist, despite having the same pressure, as seen in **Figure 18** [37,39].

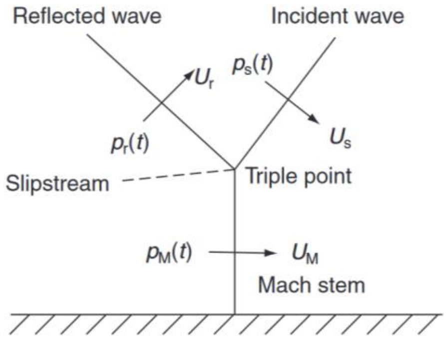

Figure 18: Mach stem triple point formation [37]

The minimum angle of incidence that permits a shock front to form a Mach stem also corresponds to the maximum deflection angle for the reflected angle. **Figure 19** illustrates a graphical solution to this problem.

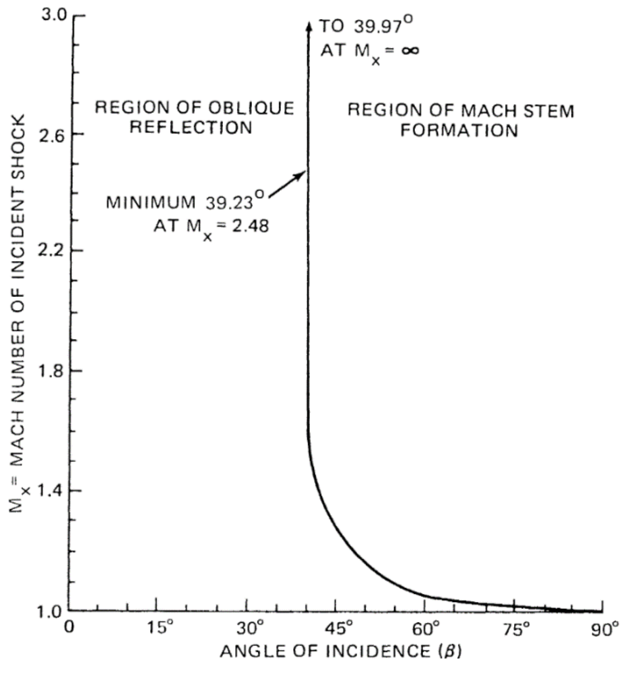

Figure 19: Angle of transition from oblique relection to Mach stem formation [38]

Before introducing the analytical solution for the graph in **Figure 19**, it is needed to introduce the notion of Mach number. The Mach number, denoted as *M*, is dimensionless index that relates the speed of an ideal gas moving at velocity *u* to the speed of sound in an ideal gas, denoted as *a*, in the surrounding medium. It can be expressed as the following equation [38]:

$$M = \frac{u}{a} \tag{2.4}$$

An analytical solution can be portrayed by the following empirical hyperbolic equation, where M_x is the Mach number for the incident shock, and β_{max} is the liming angle in degrees for Mach stem formation [38]:

$$\beta_{max} = \frac{1.75}{(M_x - 1)} + 39 \tag{2.5}$$

2.3.4. Blast wave characterization

In an explosion reaction, the first event is the generation of hot gas, which can reach pressures of 10-30 GPa and temperatures of about 3000-4000ºC. During this rapid expansion, the surrounding air is displaced from the volume it occupies. Consequently, the layer of air surrounding the gaseous products becomes compressed, containing most of the energy released from the explosion in the form of pressure. The blast wave propagates outwards from the detonation centre since there is undisturbed air ahead of it. The pressure at the blast wavefront decreases as the wavefront travels farther from the explosion source. As the gas expands excessively, the pressure at the tail of the blast wave falls below normal atmospheric pressure, creating a negative or suction effect, resulting in a reversal of the flow back towards the explosion centre [5].

The idealized pressure profile over time for a free-air blast wave from the moment of detonation is depicted in **Figure 20**.

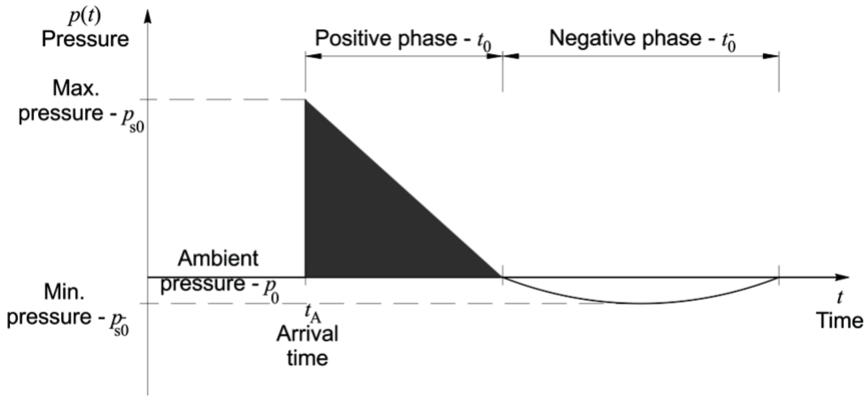

Figure 20: Pressure-time profile of the explosion wave [36]

Blast waves, as illustrated in **Figure 20**, can be characterized by three independent factors. One of these is the initial shock intensity, also known as peak overpressure, p_{s0}. Another is the duration of the blast wave. The third characteristic is the specific impulse per unit area for the pressure forces in the blast [38].

Prior to the arrival time of the shock wave, t_A, the pressure equals the atmospheric pressure, p_0. Upon its arrival, seconds after the explosion, the pressure rapidly escalates to a peak overpressure value . Subsequently, the incident pressure diminishes towards ambient pressure during the positive phase, t_0. Following the positive phase is a negative phase lasting t_0^-, typically much longer than the positive phase, characterized by pressures below the ambient pressure. The minimum value during this negative phase is referred to as the peak negative overpressure, p_{s0}^- [5,35,36,38].

When a finite pressure disturbance occurs in the air, the compressible nature of air causes the front of this disturbance to steepen as it passes through the air until it exhibits discontinuous increases in pressure, density, and temperature. As a result, the shock wave moves supersonically, meaning it moves faster than the speed of sound in the air ahead of it [26]. The pressure-time profile as well as the ideal positive phase and an approximate linear decay, can be seen in **Figure 21**.

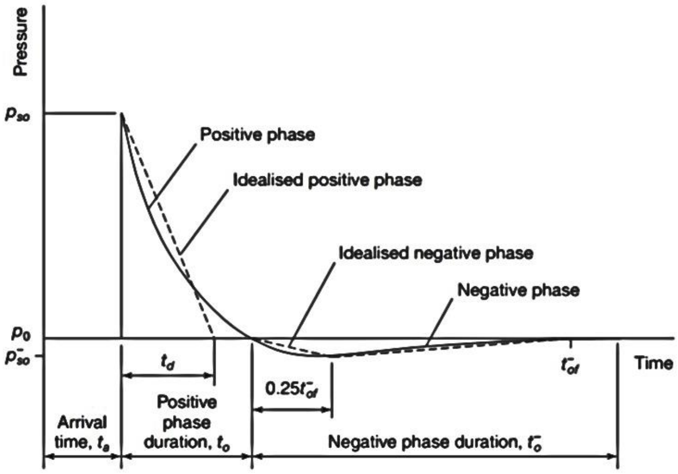

Figure 21: Idealisation of positive phase pressure-time profile [35]

The pressure-time profile can be described by the modified equation of Friedlander (Equation (2.6)), at the atmospheric pressure [5,31,39]:

$$p(t) = p_{s0}\left[1 - \frac{t}{t_0}\right] e^{-b\frac{t}{t_0}} \tag{2.6}$$

where *b* is the waveform parameter, a function of shock strength of the blast wave, which contains values derived from the scaled distance.

The impulse produced by the shock wave, i_s, is the integration of the overpressure curve from equation (2.6) for the positive phase, and can be analytically calculated as in equation (2.7):

$$i_s = \int_{t_a}^{t_a+t_0} p(t)\,dt = \frac{p_{s0}t_0}{b^2}(b - 1 + e^{-b}) \tag{2.7}$$

However, the variation of overpressure is often approximated by a linear decay as shown in **Figure 21**, as the negative phase of a shock or pressure wave is typically weaker than the positive phase, hence it can be disregarded for a blast resistant design purpose. Ignoring it is also considered conservative [40]. The duration of this decay in milliseconds is denoted as t_d. Then, the impulse can be obtained as in equation (2.8):

$$i_s = \frac{1}{2}t_d p_{s0} \tag{2.8}$$

There is a distinction between peak reflected overpressure and incident overpressure. The incident overpressure is the initial wave that reaches the structure unobstructed. When this shockwave strikes the structure, it reflects off the surface, amplifying the pressure - this is known as the reflected overpressure. The reflected wave has a higher overpressure because of the interaction with the surface. The reflected overpressure can be calculated using the Hugoniot equation [41], provided the incident overpressure is known, as described in equation (2.9).

$$P_r = 2P_i\left(\frac{7+4\frac{P_i}{P_0}}{7+\frac{P_i}{P_0}}\right) \tag{2.9}$$

2.3.5. Empirical formulation to obtain blast parameters

Since 1950, the scientific community has been investigating equations for peak overpressure and associated parameters in blast loads. This pursuit has been greatly influenced by pivotal studies dating back to 1915, notably the pioneer work of Hopkins and Cranz, who introduced the scaling method, elucidated in equation (2.1), which laid a foundational framework for subsequent research endeavours in this domain [42].

2.3.5.1 Brode [43]

Brode [43] contributed advancements by proposing peak overpressure formulations in bars to the scaled distance, as delineated in equations (2.10) and (2.11) adapted from [5]:

$$p_{s0} = \frac{6.7}{Z^3} + 1\ (p_{s0} > 10bar/1000\ kPa) \tag{2.10}$$

$$p_{s0} = \frac{0.975}{Z} + \frac{1.455}{Z^2} + \frac{5.85}{Z^3} - \ 0.019\ (0.1\ bar/10\ kPa < p_{s0} < 10\ bar/1000\ kPa) \tag{2.11}$$

2.3.5.2 Henrych [44]

Henrych [44] introduced refined expressions for peak overpressure across various scaled distance regimes in equations (2.12), (2.13) and (2.14):

$$p_{s0} = \frac{14.072}{Z} + \frac{5.54}{Z^2} - \frac{0.375}{Z^3} + \frac{0.00625}{Z^4}\ \left[\frac{kgf}{cm^2}\right] (0.05 \le Z < 0.3) \tag{2.12}$$

$$p_{s0} = \frac{6.194}{Z} - \frac{0.326}{Z^2} + \frac{2.132}{Z^3}\ \left[\frac{kgf}{cm^2}\right] (0.3 \le Z \le 1) \tag{2.13}$$

$$p_{s0} = \frac{0.662}{Z} + \frac{4.05}{Z^2} + \frac{3.288}{Z^3}\ \left[\frac{kgf}{cm^2}\right] (1 \le Z \le 10) \tag{2.14}$$

Henrych [44] also introduced an empirical expression for the maximum reflection overpressure as shown in the following equation:

$$p_r = 10 \times Z^{-\frac{3}{2}}\ \left[\frac{kgf}{cm^2}\right] \tag{2.15}$$

2.3.5.3 Kingery and Bulmash [45]

Kingery and Bulmash [45] provided comprehensive equations (2.16) and (2.17) facilitating the calculation of parameters for both free-air and surface bursts:

$$u = k_0 + k_1 \times \log(Z) \tag{2.16}$$

$$p_{s0} = 10^{C_0 + C_1 \times u + C_2 \times u^2 + \cdots + C_N \times u^n} \tag{2.17}$$

where *C* and *K* are constants are dependent on the type of burst, the range of scaled distance, and the parameters to be calculated, and *n* is the order of the polynomial [46]. The number of the constat *K* is 2, while that of the constant *C* ranges from 4 to 15 [47]. **Table 16** in the Appendix, provides a list of constants for a specific explosion.

Following the equations (2.16) and (2.17), Kingery and Bulmash [45] also provide parameters for the calculation for a free-air blast for the peak reflected overpressure, as shown in **Table 17** in the Appendix.

2.3.5.4 UFC [35]

The Kingery and Bulmash [45] proposals enable calculations for the free-air and to surface burst parameters in a scaled distance range of 0.05 to 40 m/kg$^{1/3}$. Its integration into influential manuals such as UFC 3-340-02 [35], by the U.S. Department of Defence underscores its significance both academic and practical spheres, one of the charts produced by that manual can be seen in **Figure 22**. Moreover, its incorporation into commercial software programs like Abaqus, Autodyn, and LS-Dyna has further solidified its status as a standard in blast load analysis [47].

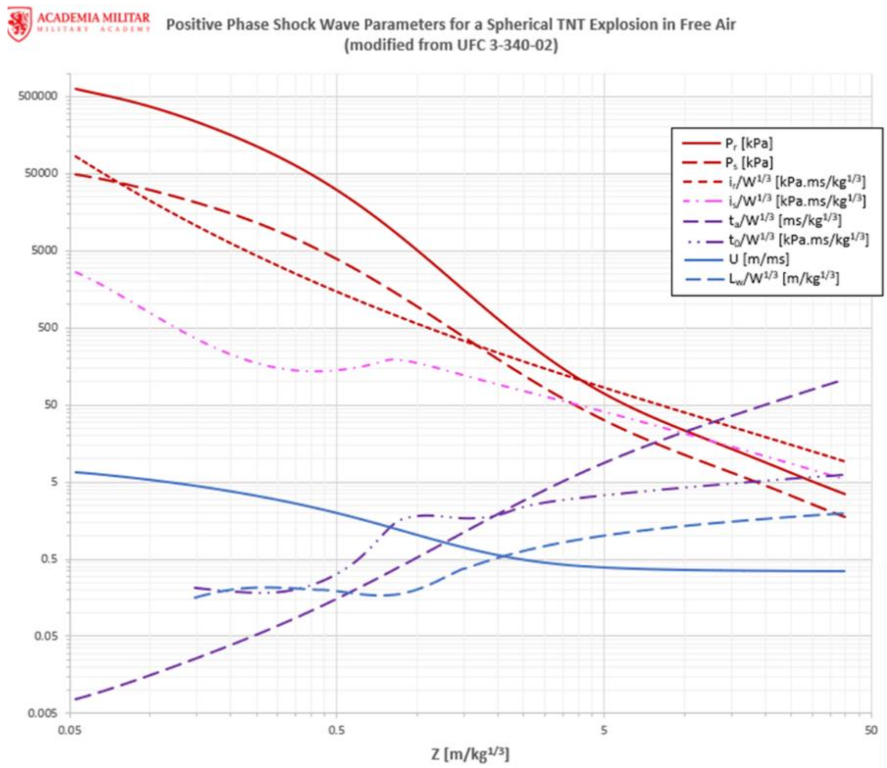

Figure 22: Positive phase shock wave parameters for a TNT explosion in free air at sea level, adapted by Lt. Col. Eng Pedro Matias from [35]

2.3.5.5 Kinney and Graham [38]

Kinney and Graham's [38] proposal of the overpressure (2.18) factors in the ratio of explosion overpressure to ambient pressure, p_{s0}/p_0:

$$\frac{p_{s0}}{p_0} = \frac{808\left[1+\left(\frac{Z}{4.5}\right)^2\right]}{\sqrt{1+\left(\frac{Z}{0.048}\right)^2}\sqrt{1+\left(\frac{Z}{0.32}\right)^2}\sqrt{1+\left(\frac{Z}{1.35}\right)^2}} \tag{2.18}$$

The positive impulse per unit area serves as an indicator of the impulse characteristics for the entire blasts wave system, given that the blast wave is primarily associated with the positive pressure phase [38]. This positive impulse per unit area can be described by the empirical equation below:

$$\frac{i_s}{\mathrm{A}} = \frac{0.067\sqrt{1+\left(\frac{Z}{0.23}\right)^4}}{Z^2\sqrt[3]{1+\left(\frac{Z}{1.55}\right)^3}} \tag{2.19}$$

The time duration of the blast wave is a crucial aspect of its ability to cause damage, as mentioned before. The duration of the positive pressure can be measured more precisely, and it is during this phase that the blast wave is most damaging. The duration of the blast wave is the time between the passing shock front and the end of the positive pressure phase, marked by zero overpressure. Hence, the duration of the blast wave increases with distance from the centre of detonation and reaches its maximum value when the shock front degenerates into a sound wave. The duration for the positive overpressure phase can be obtained by the following equation [38]:

$$\frac{t_d}{\mathrm{W}^{\frac{1}{3}}} = \frac{980\left[1+\left(\frac{Z}{0.54}\right)^{10}\right]}{\sqrt{1+\left(\frac{Z}{0.02}\right)^3}\sqrt{1+\left(\frac{Z}{0.74}\right)^6}\sqrt{1+\left(\frac{Z}{6.9}\right)^2}} \tag{2.20}$$

where $t_d/W^{1/3}$ is the duration in milliseconds for a one kilogram TNT explosion [38].

2.3.6. Explosion Driven Shock Tube (EDST)

There are two ways to study the dynamic and impulsive behaviour of explosives: through free air blast (FAB) experiments or in the laboratory, using shock tubes that propagate the action of an explosion, known as explosion driven shock tube (EDST).

FAB can produce a larger range of pressure-impulse variations by varying the explosive mass and/or stand-off distance. However, it is more difficult to reproduce consistent pressure profiles, and it is susceptible to the local conditions of the environment in which the explosion occurs.

Current shock tubes include compression-driven and blast-driven designs of varying dimensions. A compression-driven shock tube is divided into two sections: the driver (where the high-pressure gas is maintained) and the driven section (which can be air or a low-pressure gas), separated by a diaphragm. When the diaphragm suddenly bursts, a shock wave propagates through the driven section because the shock wave increases the pressure and moves from a high-pressure zone to a low-pressure zone, inducing a flow in the direction of the shock wave. This method produces significant variations in peak pressure, and the pressure waves have longer durations than real ones. Additionally, they do not accurately reproduce the Friedlander waveform of free-field blast waves. To rupture the diaphragm, it can be pierced by a mechanically driven plunger or by using diaphragms with specific bursting pressures, as seen in **Figure 23** [48,49].

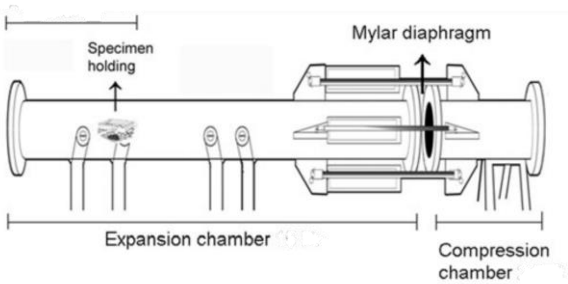

Figure 23: Compressed air-driven shock tube [50]

Blast-driven shock tubes consist of a simple tube with varying cross-sectional geometries between the explosive charge and the main target. They can be either half-open, with a closed entrance side where the charge is placed and the blast wave directed to the open side, or open in both sides, where the explosive charge is placed at a certain distance from the entrance, and the blast wave is directed through the tube toward the other open side, as seen in **Figure 24**. This method produces more realistic pressure-time profiles, like the Friedlander waveform, but it requires additional equipment and facilities [49,51].

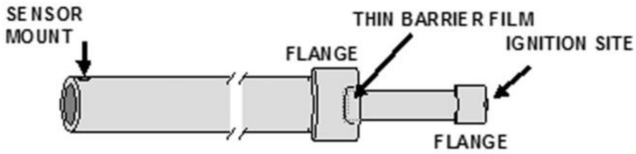

Figure 24: Blast driven shock tube [48]

2.3.6.1 Blast wave properties using EDST

For FAB, the equations mentioned in subchapter 2.3.4 can be used.

To obtain the blast wave properties using EDST, experimental campaigns must be conducted to assess the blast wave characteristics of the specific shock tube in use. Some authors have developed analytical equations to obtain the incident pressure at a specific section in terms of the tube length, diameter, explosive mass, and the stand-off distance.

To develop the analytical procedure, there is a need to identify the main parameters of the dimensional analysis. The first one to define is the EDST equivalent diameter, *D*, which is dependent on the EDST cross-sectional area, *S*, as follows [49]:

$$D = 2\sqrt{\frac{S}{\pi}} \tag{2.21}$$

There is also a need to obtain a reduced equivalent mass, W_r, dependent on the stand-off distance of the distance of the explosive charge to entrance of the shock tube, *d*, the mass, *W*, and the EDST sectional area, *D*, as follows [49]:

$$W_r = \left(1 - \frac{d}{\sqrt{d^2 + \frac{D^2}{4}}}\right) W \tag{2.22}$$

It is also important to mention that, for explosions carried out using a shock tube, according to the conditions defined previously, the reduced distance Z_{EDST} [49], is obtained through expression (2.23)

$$Z_{EDST} = \frac{LD^2}{W_r} \quad (2.23)$$

Liu et al. [52] developed an analytical formula for the incident overpressure at the end of a tunnel characterized by a specific section geometry, as shown in **Figure 25**. This formula is given in equation (2.24).

$$P_i = 1.4 \times \left(\frac{LS}{W}\right)^{-0.846} \times \left(\frac{D}{W^{\frac{1}{3}}}\right)^{0.563} \quad (2.24)$$

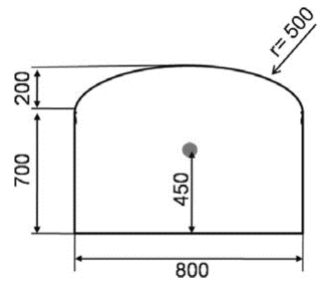

Figure 25: Liu et al. [52] tunnel section (units in mm) [52]

2.3.7. Pressure impulse diagram

The fundamental natural period of a structure and its relation to the positive phase duration of an excitation play an important role in its behaviour. If the duration of the excitation is longer than the natural period of the structure, then its maximum deflection takes place before the excitation ceases, and a dynamic analysis should be used, as is often the case for earthquake loading. If the duration of the positive phase of the excitation is much shorter than the natural period of the structure, then it is considered impulsive loading.

For a particular structure and load type (pressure), these considerations can be depicted schematically by an iso-response curve in pressure-impulse (P-I) diagram, as shown in **Figure 26**. For very short duration loads (relative to the natural period of vibration of the structure, T), the structural response is sensitive to the associated impulse rather than the maximum pressure (vertical asymptote). However, as the load duration increases towards a quasi-static, the response becomes sensitive to the maximum value of pressure rather than the impulse (horizontal asymptote).

This can be summarized by the ratio between the duration of the idealized triangular blast load, t_d, and the natural period of vibration of the structure by the equation (2.25) [5,53].

$$\frac{t_d}{T} < 0.1 \qquad \text{Impulsive}$$

$$0.1 < \frac{t_d}{T} < 10 \qquad \text{Dynamic} \quad (2.25)$$

$$10 < \frac{t_d}{T} \qquad \text{Quasi-static}$$

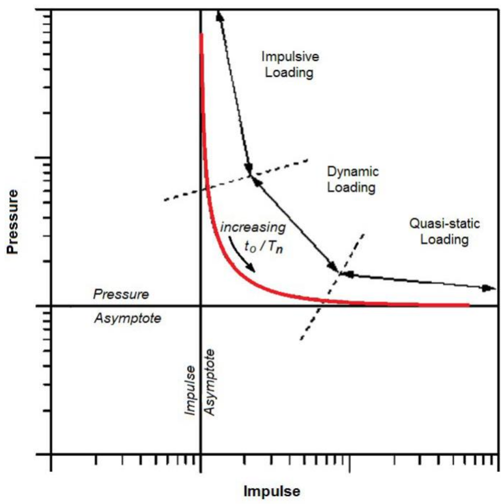

Figure 26: Typical Pressure-Impulse diagram [53]

An iso-response diagram can be associated with an iso-damage diagram when the pressure-impulse combination will cause a specified level of damage. This graph format allows easy assessment of the structural response to a specified load. Once a damage level is defined, the curve indicates the combination of load and impulse that will cause failure. Combinations of pressure and impulse that fall to the left and below the curve will not induce failure, while those to the right and above the graph will produce damage in excess to the established limit [5].

The theoretical method from Chen et al. [15] proposes creating an iso-damage curve under different blast loading combinations to address damage levels of laminated glass, namely: (1) the glass crack limit, (2) the PVB rupture limit, and (3) overall detachment with a specific velocity after PVB rupture. These levels are based on GSA-TS01 [54], a test standard primarily focused on estimating the performance of window systems subjected to blast loads.

In laminated glass, the limit of tearing is the most important criterion for assessing hazards. Loading beyond this limit increases the hazard, as even large tears may not allow significant blast pressure to enter. However, if the rupture is sufficiently violent, separated glass panels can be detached and thrown.

According to Shi et al. [55], a P-I curve for a structure can be expressed by the following equation, where p is the peak overpressure, *I*, is the impulse, i_{cr} denotes the impulse value of the impulsive asymptote, p_{cr} is the overpressure value of the overpressure; α and β are parameters related to the properties of the structure, which determine the shape of the curve in the dynamic zone:

$$(p - p_{cr})(i - i_{cr}) = \alpha \left(\frac{p_{cr}}{2} + \frac{i_{cr}}{2}\right)^{\beta} \tag{2.26}$$

3. Numerical analysis

The development of numerical models plays a crucial role in modern engineering, offering detailed insights and precise solutions to complex problems. This chapter presents an overview of these models, beginning with an introduction to the relevant concepts and methodologies. It then delves into the tools and characteristics considered, explaining the decisions behind their development.

Traditional engineering approaches often rely on simplified physical models and basic equations to obtain solutions. While these methods provide conservative estimates, they tend to oversimplify problems, limiting their applicability to a narrow range of scenarios. As a result, only a small fraction of engineering challenges can be solved analytically [56,57].

3.1. Finite Element Method

Finite element methods (FEM) offer a more detailed analysis, leading to precise and accurate results across a wide range of applications, from heat transfer to stress analysis. FEM involves discretizing a geometry into finite elements connected by nodes, which are then used in a solver to obtain approximate solutions. Although no FEM solution is ever entirely accurate, these methods have proven highly effective, especially for analysing complex structural elements like laminated glass under blast loads [57,58].

This approach can be summarized in the **Figure 27**, where a body is subject to a force, P. The objective of the study is to determine the mechanical response of the system under the effect, P, this is the physical problem. Then there is the need to idealize the problem within the computation platform and to discretize the system into small solvable units. Based on the finite elements method, the next step is to applicate the principles of engineering mechanics to solve for any unknow parameters associated with the mechanical response of the physical system, the principles of mechanics can also mean as governing equations for a given problem. The final step involves the application of numerical methods to determine a solution to the physical problem, and to obtain approximate solutions. The assembly step involves integration of solution from each finite element into a global output which defines the desired solution to the physical problem [57].

The solution from the finite element process depends on the size of the finite elements, more resolution or predictive fidelity can be done by adding more nodes or elements to the discretization of the geometric domains, however it leads to greater computational effort [57].

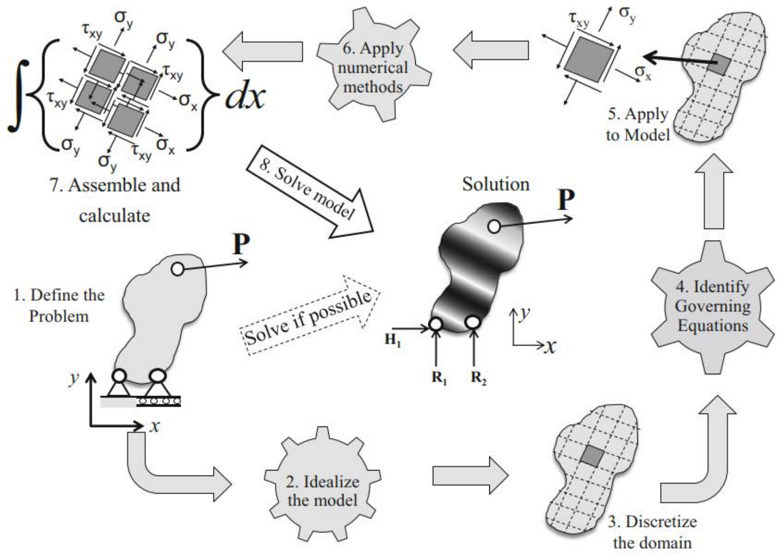

Figure 27: Schematic representation of the key processes t to the finite elemnet method [57]

3.2. Methodology

The definition of the laminated glass and the blast load into a mathematical problem, started with the creation of the different individual bodies geometries that constitute the system. LS-Prepost was used as a pre-processor to create the 3d model, the mesh grid and to define the problem parameters. The analyses were conducted through the solver LS-DYNA, achieving the problem approximate solution. Following the analyses, the results were imported once again to LS-Prepost. In this step, the latter was used as a post-processor to convert the output into a visual form, as represented by the **Figure 28**.

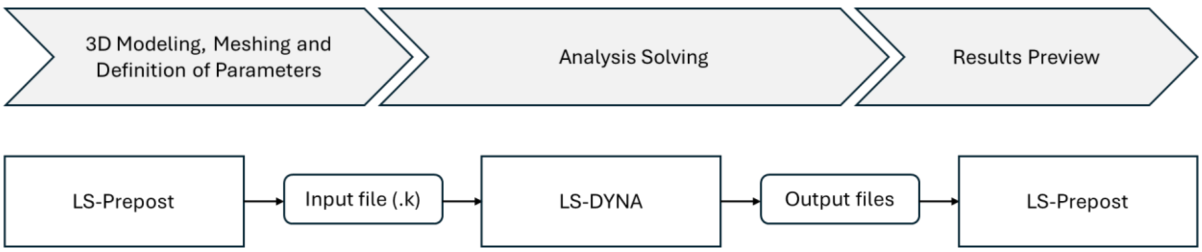

Figure 28: Diagram used for the numerical analysis

3.3. Software

All simulations were conducted using a laptop with Windows 64-bit operating system, powered by an Intel® Core ™ i7-8550U (4 Core) 1.80 GHz Processor. The LS DYNA version utilized was LS-DYNA Suite R14 and the LS PrePost version was 4.10.5.

3.3.1. LS-Prepost

LS-PrePost is an advanced pre-processor and post-processor provided free of charge with LS-DYNA. The process with LS-PrePost encompasses two distinct actions. As a pre-processor, essential steps include defining materials, loads, boundary conditions, element types, among other parameters incorporated into the LS-DYNA input file. As a post-processor, it allows exploration and analysis of results through various possibilities such as visual animations and data history plotting, among others [59].

3.3.2. LS-DYNA

LS-DYNA, developed by Livermore Software Technology Corporation (LSTC), is a finite element analysis software known for handling highly non-linear problems with great accuracy. Widely used in automotive, aerospace, and civil engineering. LS-DYNA excels in simulating structural responses to dynamic loads, such as impacts and explosions. The software utilizes empirical equations to simulate air blast pressures, eliminating the need to model the air or explosive directly when needed [57,60].

In addition to LS-DYNA, several other FEM software packages are prominent in the industry. These include IDEAS®, SAMCEF®, NASTRAN®, ABAQUS®, FIDAP®, MARC®, ANSYS®, ADINA®, ASTER®, and CASTEM®. Each of these tools offers unique capabilities and is used across various engineering disciplines to simulate complex material behaviours and structural responses [61].

LS-DYNA as a solver, uses a card system, called keywords, where variables within the model input file are denoted by classification (e.g., *PART, *MAT, *LOAD). All the input files are in simple ASCII format and thus can be prepared using any text editor [9].

Like most FEM calculation software, LS-DYNA requires the use of consistent set of units, as the set units in **Table 2**.

Table 2: Set of units for the numerical model

Mass	Length	Time	Force	Stress	Energy	Speed	Density
kg	mm	ms	kN	GPa	$kN \times mm$	$\frac{mm}{ms}$	$\frac{Kg}{mm^3}$

3.4. Model characterization

Initial models were created to study two possible boundary conditions for the glass fixing system: simply supported and fully fixed. These models consisted only of the glass and the PVB interlayer. Later, a more detailed model was developed, incorporating the metal support and a rubber layer to prevent direct contact between the glass and the metal, as presented in **Figure 29**.

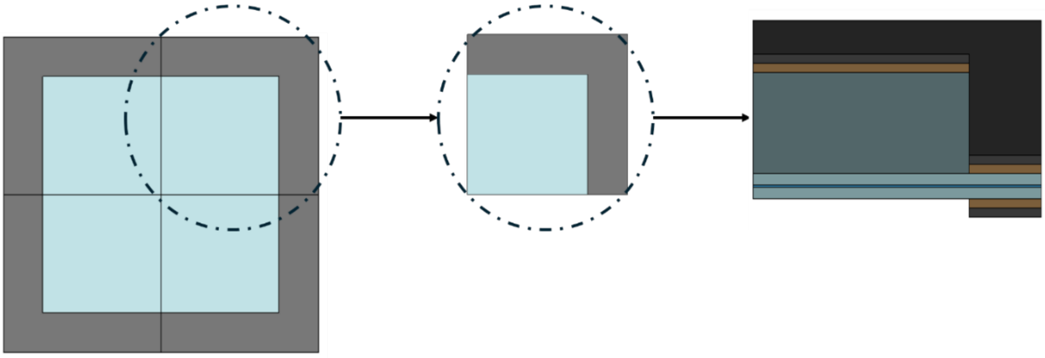

Figure 29: Set up model with the working parts - the full glass panel, the quarter glass panel, and the model's components (black for metal, light brown for rubber, light blue for glass, and blue for PVB)

3.4.1. Optimization and Simplification

Due to the high computational cost of this analysis, every effort was made to simplify and improve cost-efficiency. When considering the model, geometry simplification was made possible by leveraging the symmetry of the glass pane. Analyses used this simplification, modelling only one-quarter of the glass panel. LS-PrePost's post-processing capabilities include a reflection method, which allows for the creation of the complete model afterward.

Another simplification involved the blast wave generated by the explosion, for which the Friedlander (Equation (2.6)) was used.

3.4.2. Element types

Defining the elements can be done in different ways, namely section-wise with solid, shell, and beam elements. Furthermore, it can be chosen its formulation and integration rule. In this model, only solid elements (constant stress solid element, element type 1) were used. Shell elements are commonly used to simplify and speed up the analysis whenever they are adequate. Solid elements are three-dimensional finite elements that can model solid bodies and structures without any prior geometric simplification. It benefits from the fact that it does not require geometric, constitutive, and loading assumptions; boundary conditions are treated more realistically (compared to shells or beams); finite element mesh looks like the physical system. Nevertheless, it requires higher effort: mesh preparation, CPU time, post-processing, among others [62].

3.4.3. Contacts

LS-DYNA has hundreds of different contacts, and it is necessary to define them. They are important to avoid errors, elements penetrations, and even unreliable results (like negative volume elements). Accurately modelling the interactions between different components in finite element analysis is crucial for realistic simulation results.

The contact between the glass and the PVB was modelled by merging nodes at the interface, mirroring the actual laminated glass assembly where the PVB is adhesively bonded to the glass layers. Similarly, the rubber and metal support interface were also modelled with merged nodes to simulate a tight fit that prevents slippage and ensures efficient load transfer.

In contrast, the contact between the rubber and the glass was defined using an "Automatic Surface to Surface" contact. This accounts for potential slippage between the rubber and glass, as they are not bonded but merely in contact, which is essential for capturing realistic interactions under dynamic loading conditions like blasts.

3.4.4. Hourglass

In finite element analysis, hourglass control is crucial to prevent the occurrence of non-physical zero-energy modes, commonly referred to as hourglassing. LS-DYNA offers various hourglass control algorithms that can be applied depending on the type of elements used and the specific requirements of the analysis. To ensure stability and accuracy in the simulation results, the stiffness form of Type 2 (Flanagan-Belytschko) was employed in this study, with an hourglass coefficient of 0.1.

3.4.5. Output Database

The output files which contain the results information are defined previously in the database keyword group. It can be done in several formats and options. In this case, the options used were as follows: the **ASCII** format, which was primarily used for hourglass and energy data, as well as for nodal time history data elements (stresses, strains, energy, velocities, among others) using GLSTAT, MATSUM, and NODOUT. The **BINARY_D3PLOT** format was used for complete graphic states output (stresses, strains, energy, velocities, among others). An **EXTENT_BINARY** format used for additional output data not covered by standard binary files. Additionally, the **HISTORY_NODE** option was used to specify the recording of data for a particular node, in this case, the centre of the glass panel.

The time interval between outputs was chosen to match the frame capture rate of the cameras (0.05 ms) and lasers (0.9 ms) from the experiment, with the shortest interval of 0.05 ms being selected.

3.4.6. Termination Time

In LS-DYNA, the analysis is stopped at a specified time, called the termination time, which is determined by the keyword *CONTROL TERMINATION. Termination time greatly influences the analysis runtime. Therefore, the analyses were specified to be stopped. The aim was to be able in each model analysis, to achieve the maximum deformation within this period while simultaneously registering all the needed results. A termination time of 10 milliseconds was used.

3.4.7. Mesh quality

Similar to the termination time, mesh quality is also an important parameter that influences runtime significantly. A simple mesh with good quality elements or a refined mesh with bad quality elements can create a slower analysis than expected.

To obtain the best results, the mesh defined for all the elements was a cube of 2 mm by 2 mm by 2 mm, except for the PVB layer, which was 2 mm by 2 mm by 1.52 mm. This means that there is only one layer for the PVB.

3.4.8. Boundary conditions

The primary constraint applied in all models to save computational time was the reflection constraint, which allowed data to be obtained from only one quarter of the model, since LS-PrePost has reflection capabilities. **Figure 30** presents a legend with the respective constraints for each side, an axis for orientation, and the centre of the glass panel.

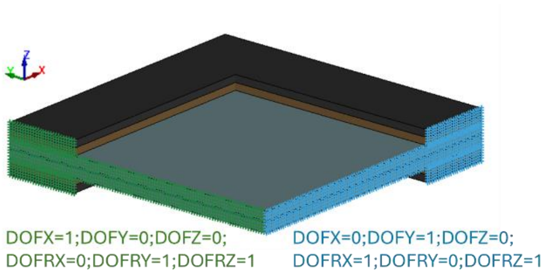

Figure 30: Quarter of the 66.4 glass panel with constrains for the reflection

As explained previously, different simulations were conducted to achieve the desired objective. The fully fixed model presupposes no translational or rotational movement in any direction. This ensured that the glass panel would be more rigid in response to the shock wave. The constraints are applied to a quarter of the panel, specifically to both the top and bottom layers of the laminated glass, and only on the two sides constrained by the structure, as shown in **Figure 31**.

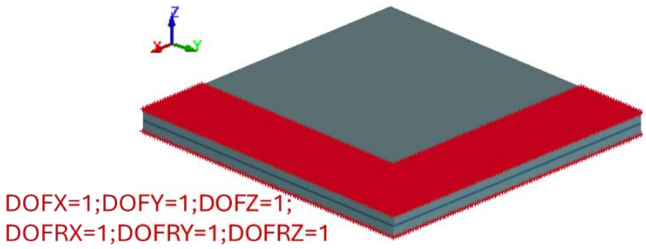

Figure 31: Quarter of the laminated 66.4 glass panel with fully fixed constraints marked in red

The simply supported model was used to allow greater displacement freedom. Translational movement was permitted, but rotational movement was not. These constraints were applied only to the PVB layer, which was positioned between the glass layers regardless of thickness. The constraints were applied only on the two sides constrained by the structure, as shown in **Figure 32**.

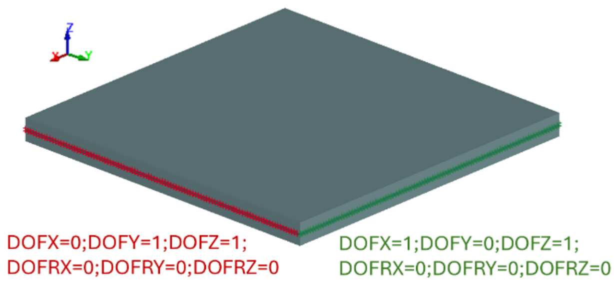

Figure 32: Quarter of the laminated 66.4 glass panel with simply supported constraints

The set-up models have constraints similar to a simply supported boundary, since it was the closest to the experimental results. The constraints were applied to the metal support and to the rubber; the constraints were also applied to the rubber to try to control its behaviour, since in reality the only object that was constrained was the metal support, as seen in **Figure 33**.

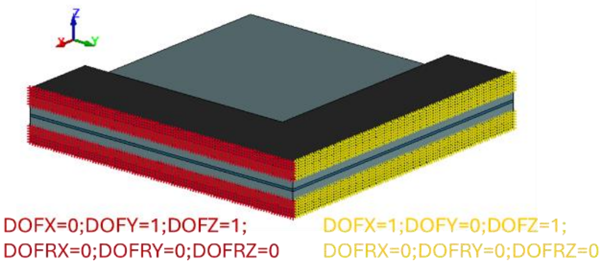

Figure 33: Quarter of the laminated 66.4 glass panel contrains for the set up model

3.4.9. Material type

3.4.9.1 Glass

To model the laminated glass, different materials were tested using a solid element. The materials tested were MAT_001_ELASTIC, which represents the complete elastic behaviour of the glass and MAT_110_JOHNSON_HOLMQUIST, a plasticity damage model for modelling ceramics, glass, and other brittle materials subjected to large strains, high strain rates, and high pressures. For the elastic model MAT_001_ELASTIC, the following properties were used: density 2.50E-06 kg/mm³, Young's modulus 70 GPa, and Poisson's ratio of 0.2.

MAT_110_JOHNSON_HOLMQUIST was developed for brittle materials under impact conditions, e.g., ballistic impact [19,63]. The parameter sets provided by Hidallana et al. [64], Holmquist et al. [65], Zhang et al. [66], Zhou et al. [67] were considered. An adjustment was made to the parameters provided by these authors: the maximum tensile strength was set to 200 MPa for all models. This change was necessary because the references consider annealed glass, which has a lower tensile strength. Since the glass modelled in this study is toughened glass, which has a higher tensile strength due to its manufacturing process, this adjustment ensures the model reflects the correct material properties. The four sets of parameters are listed in **Table 18** of the Appendix.

3.4.9.2 PVB

For the PVB, the material used was MAT_098_SIMPLIFIED_JOHNSON_COOK with the following parameters, which is a plasticity model to describe the effects of strain rate and temperature on the plastic deformation of metals [68]. This simplified model ignores thermal effects and damage. The parameters are in **Table 19** of the Appendix.

3.4.9.3 Rubber

Several models were tried, from the elastic model to MAT_024_PIECEWISE_LINEAR_PLASTICITY. However, the model that worked well was MAT_027_MOONEY-RIVLIN_RUBBER constitutive model, considering a rubber hardness of 75. This is a two-parameter material model for rubber, whose constants are listed in **Table 20** of the Appendix.

3.4.9.4 Metal

For the metal part an elastic model with following properties was used: density 7.90E-06 kg/mm³, Young's modulus 210 GPa, and Poisson's ratio of 0.3.

3.4.10. Blast Load

The blast load used for the simulations was categorized by charge, with values obtained from the experimental campaign as described in subchapter 4.1, namely average pressure, duration of linear decay, and decay parameter.

The blast loads were applied using the *DEFINE_CURVE definition and applied to the glass layer that first received the shock wave generated by the shock tube. Since only one quarter of the glass panel (200 mm by 200 mm) was modelled, and the shock tube delivered the shock wave to a 150 mm by 150 mm square, only this area received the blast load, with the remaining 50 mm of the panel edges being within the structure. Even though the 50 g charge was not used in the numerical simulations, it is still presented because it provides insight into the pressure trends for larger charges.

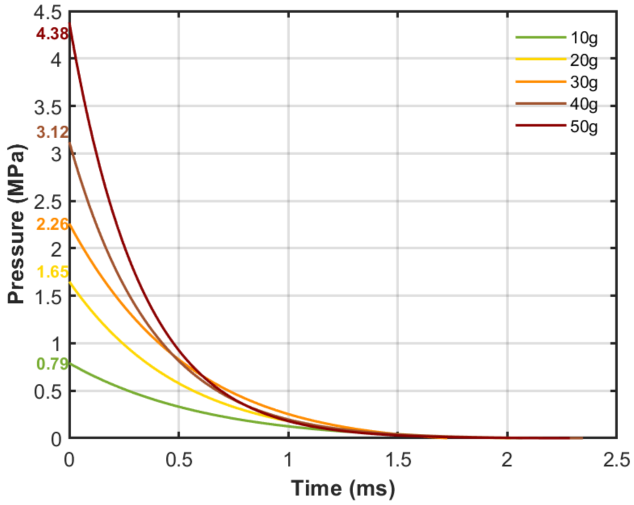

Figure 34: Blast load used on the simulations

3.4.11. Model Validation

To simulate the cracking of the glass, the option MAT_ADD_EROSION was used, since some constitutive models do not allow failure and erosion, as is the case with MAT_ELASTIC. This option can be applied to constitutive models that already include failure criteria, as is the case with the Johnson-Holmquist models. After analysing the maximum strain data from the experimental results, a maximum strain was initially chosen as 0.0045 for all the models. However, after performing the numerical simulations, there was a need to adjust these values to 0.0045 for 66.4, 0.0035 for 88.4, and 0.0028 for 1010.4 glass. These thresholds were applied using the MXEPS variable, which triggers failure based on maximum principal strain and was used exclusively in the setup models to validate displacement predictions. It is important to note that glass strength is probabilistic, with considerable uncertainties in crack and microcrack propagation, influencing the rupture criteria and varying strain and stress responses.

3.5. Obtained Results

The numerical simulations conducted in this study yielded comprehensive insights into the behaviour of laminated glass under various blast loads. The results encompass maximum displacement, maximum principal strain, and minimum principal strain for different glass thicknesses and charge weights.

3.5.1. 66.4 Laminated Glass

In figures **35** to **38**, present the simulation results for the 66.4 laminated glass type. The analysis in **Figure 37** was terminated early when the first glass nodes were eroded.

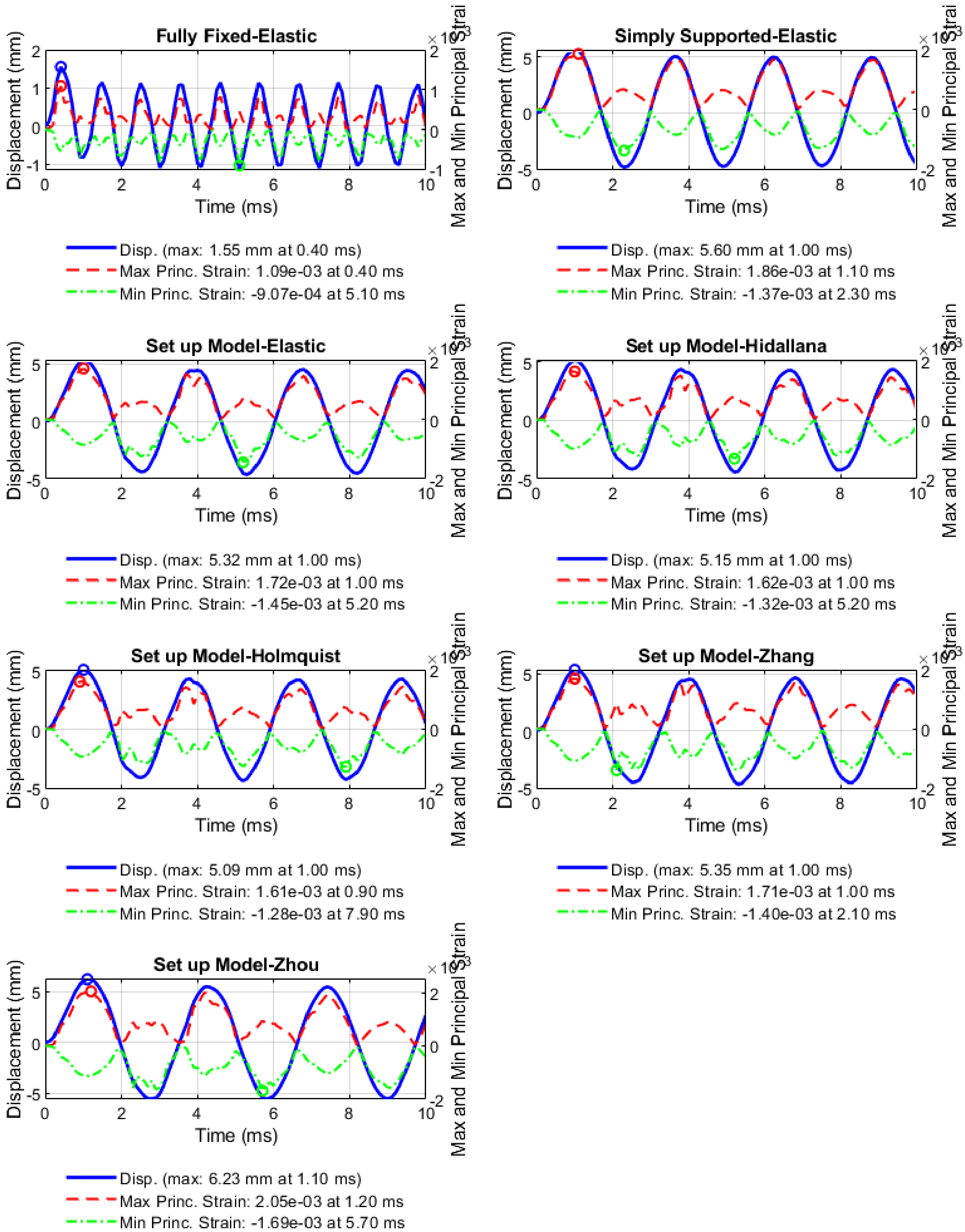

Figure 35: 66.4 Laminated glass with a 10g charge

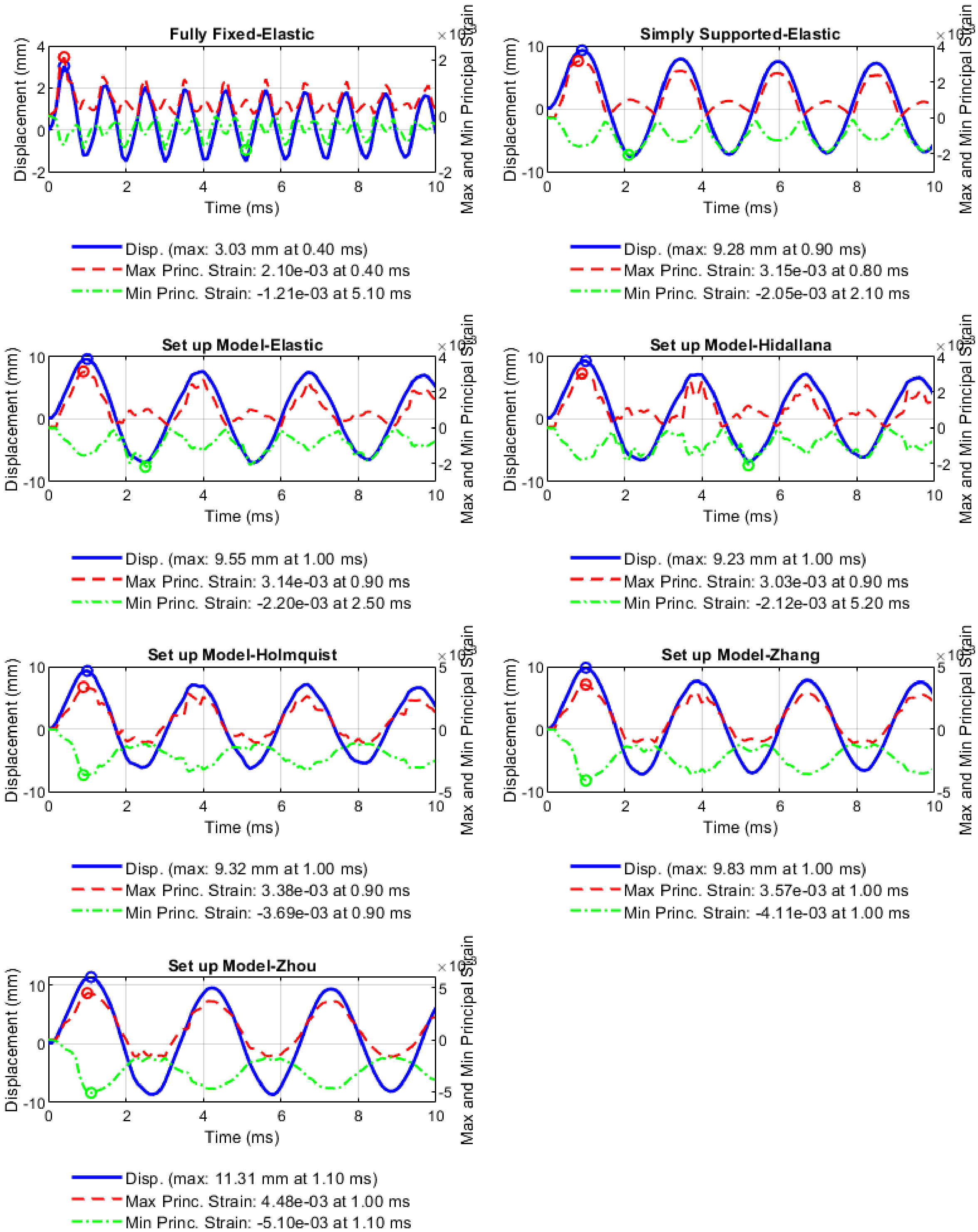

Figure 36: 66.4 Laminated glass with a 20g charge

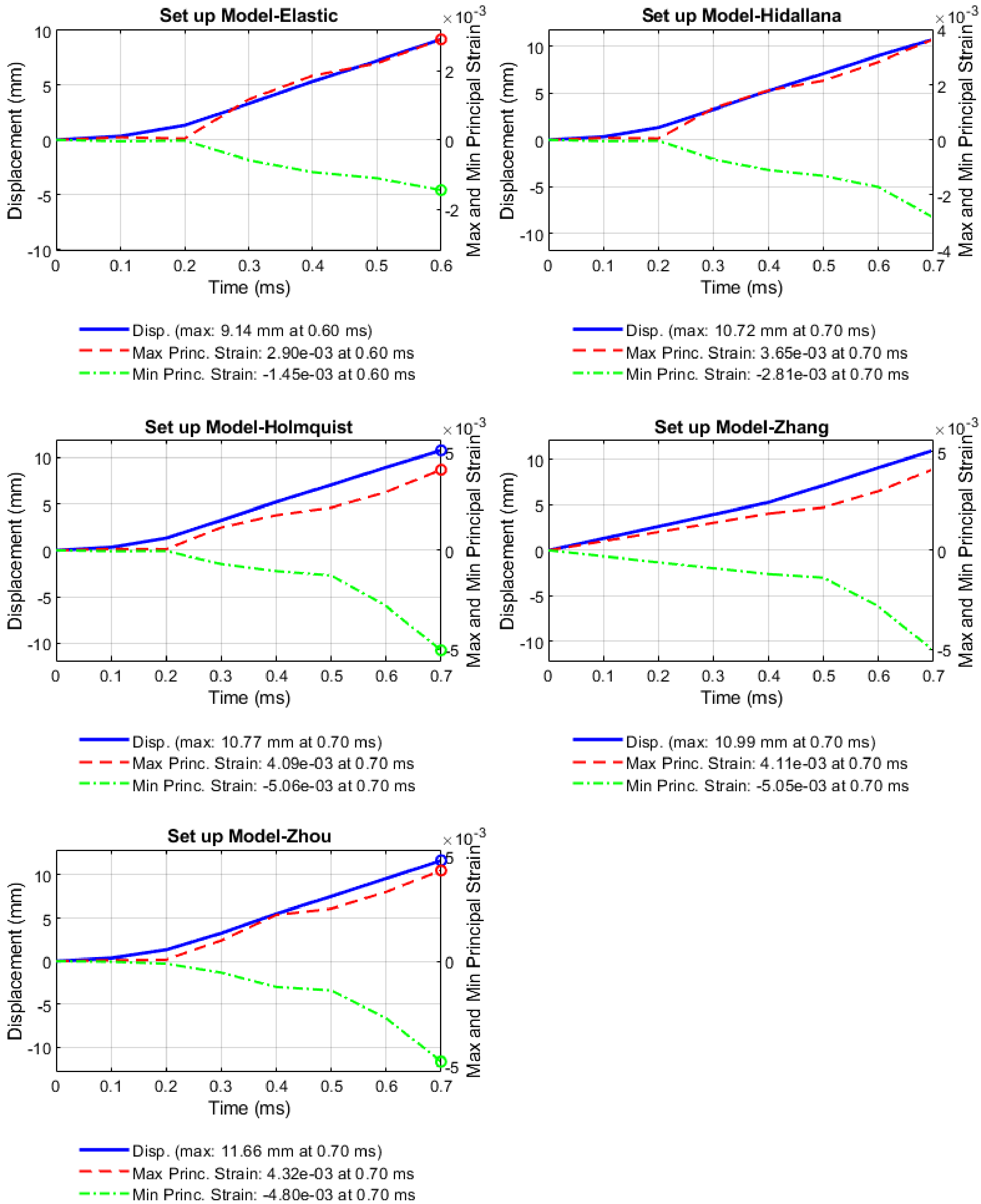

Figure 37: 66.4 Laminated glass with a 30g charge

The result of the cracking criteria can be seen in **Figure 38**.

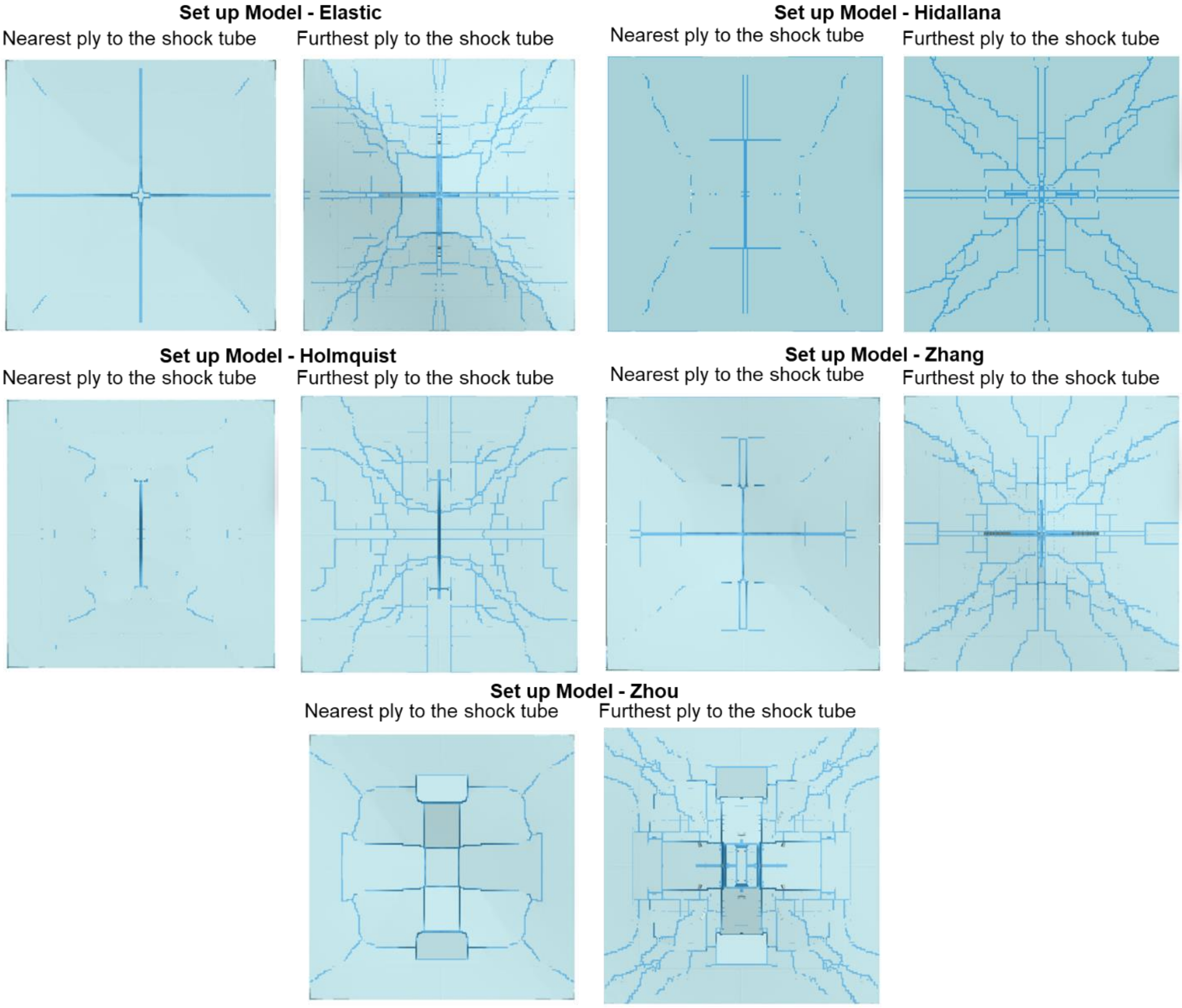

Figure 38: Destructive tests from numerical simulations for 66.4 laminated glass with a 30 g charge

3.5.2. 88.4 Laminated Glass

The simulations for the 88.4 laminated glass type are illustrated in **39** to **42**. In **Figure 41**, in the Zhang et al. [14] and Zhou et al. [67] model setups, the erosion criteria were disabled to assess maximum strain without element deletion due to failure, since it was higher than the threshold of 0.0035.

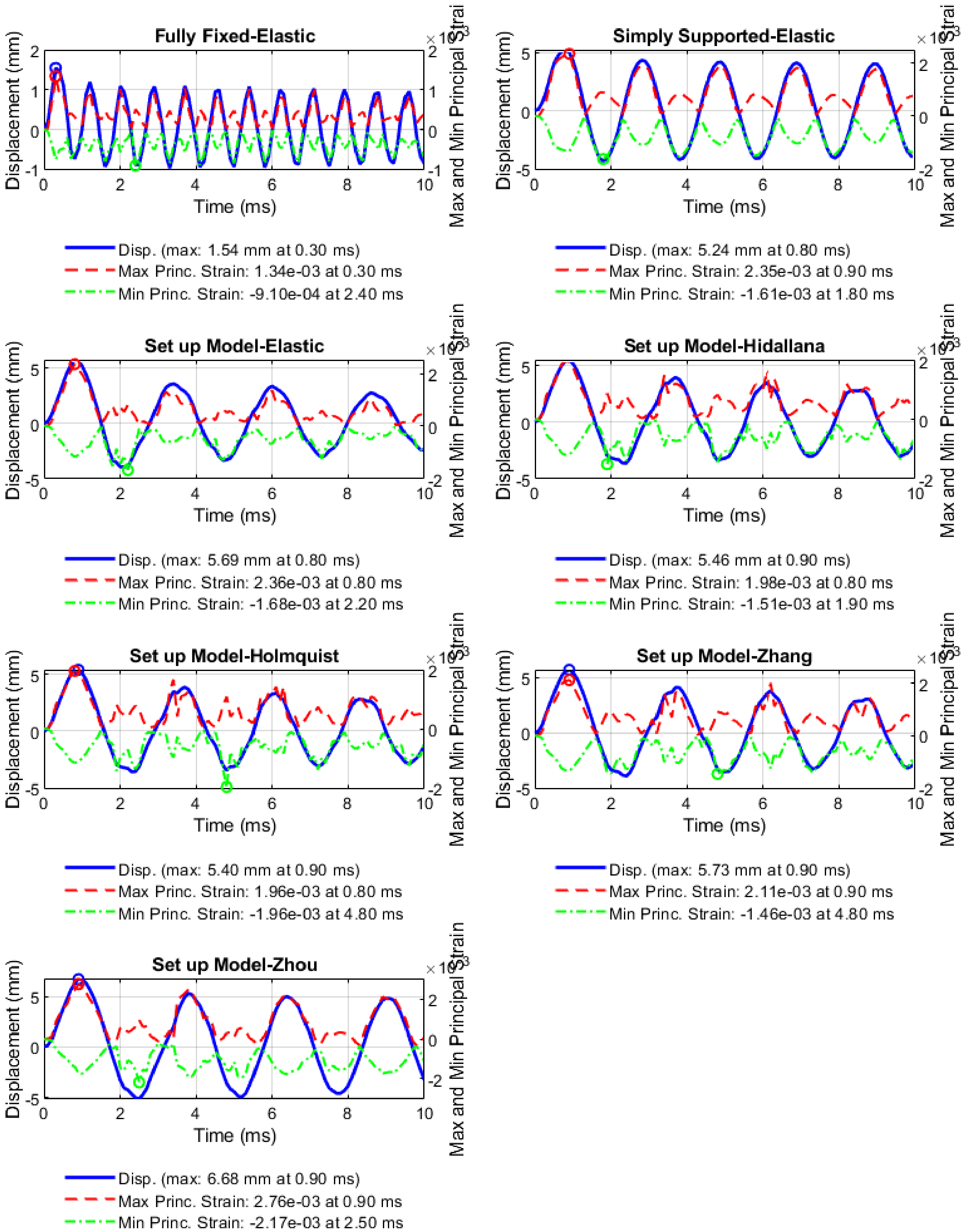

Figure 39: 88.4 Laminated glass with a 20g charge

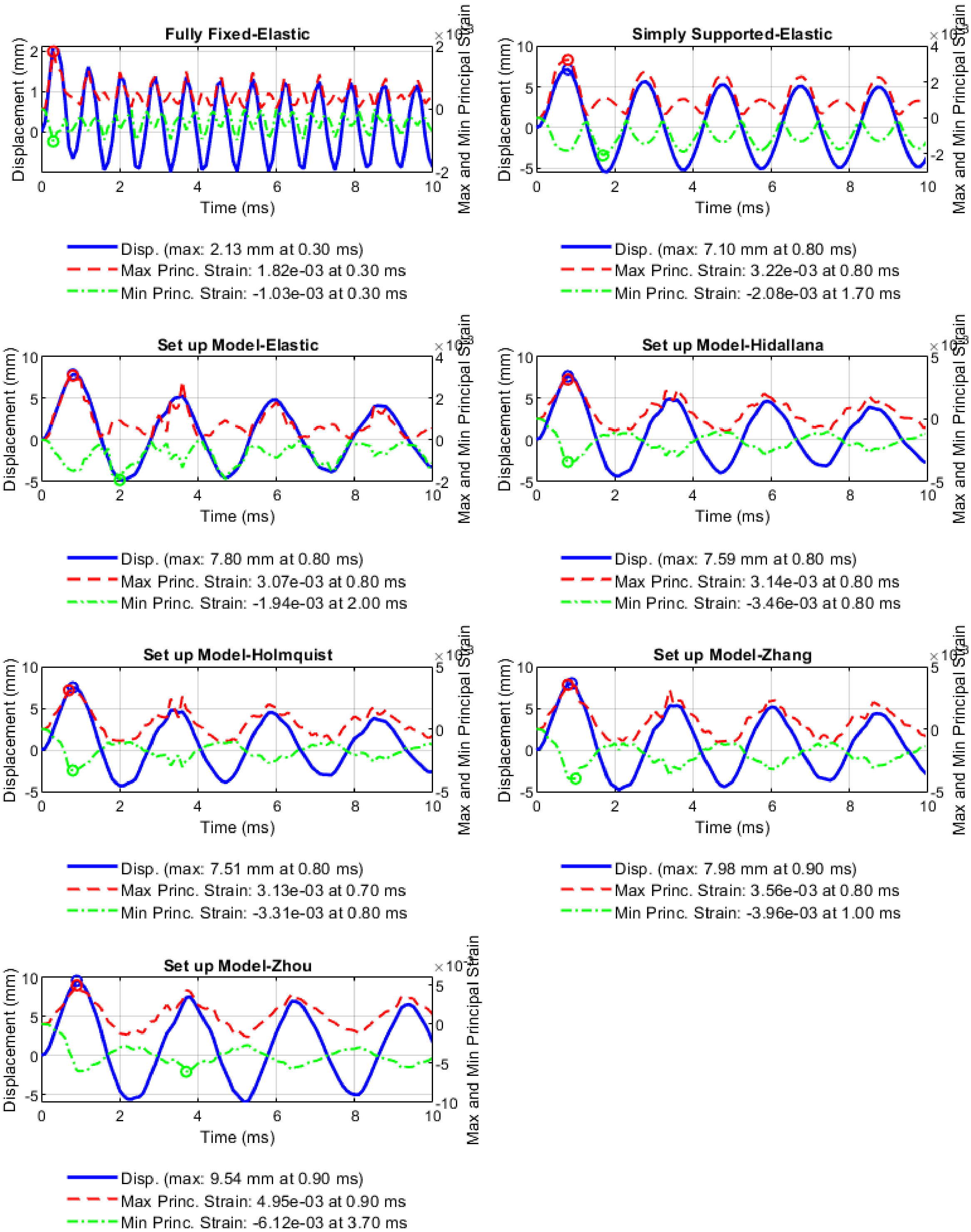

Figure 40: 88.4 Laminated glass with a 30g charge

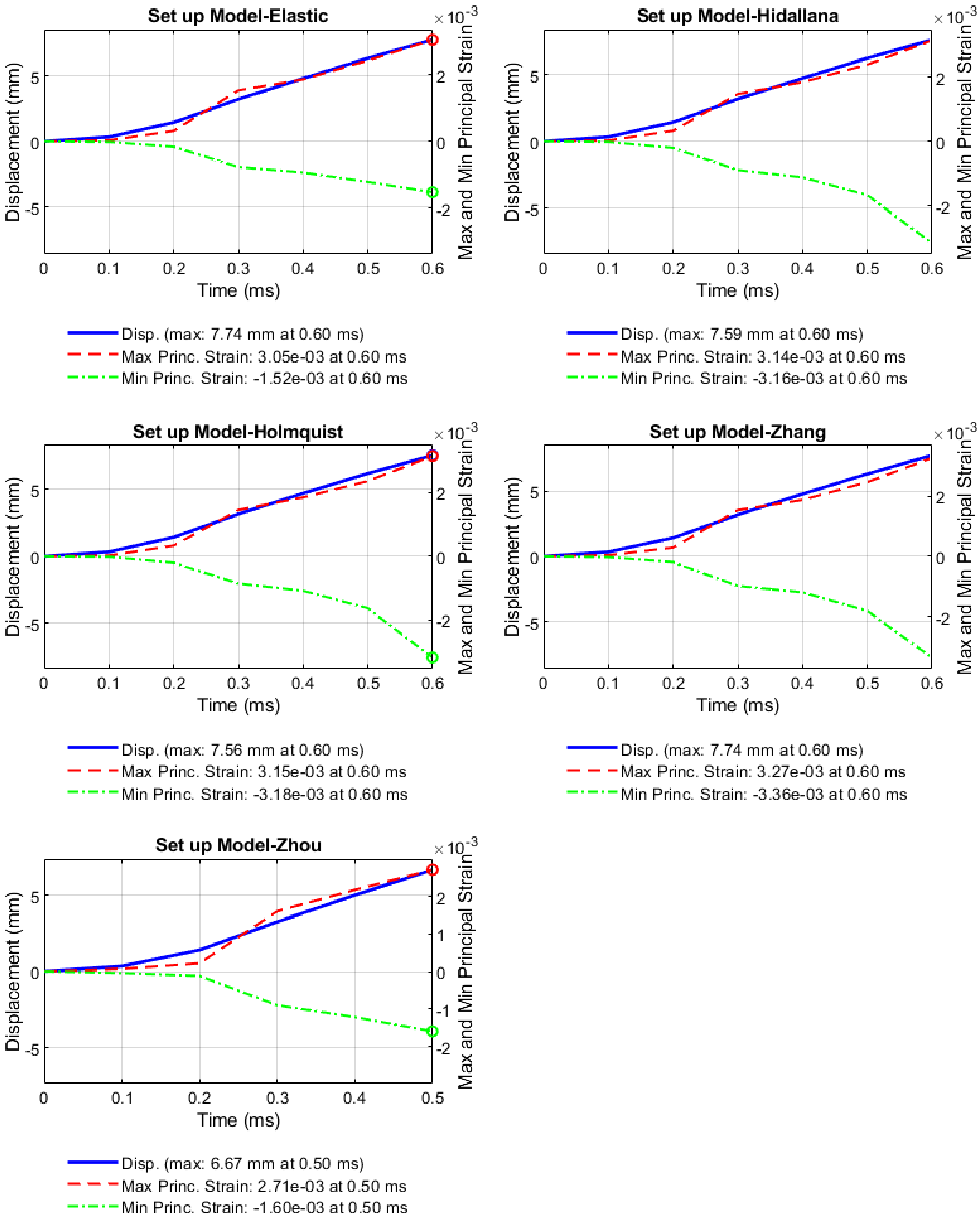

Figure 41: 88.4 Laminated glass with a 40g charge

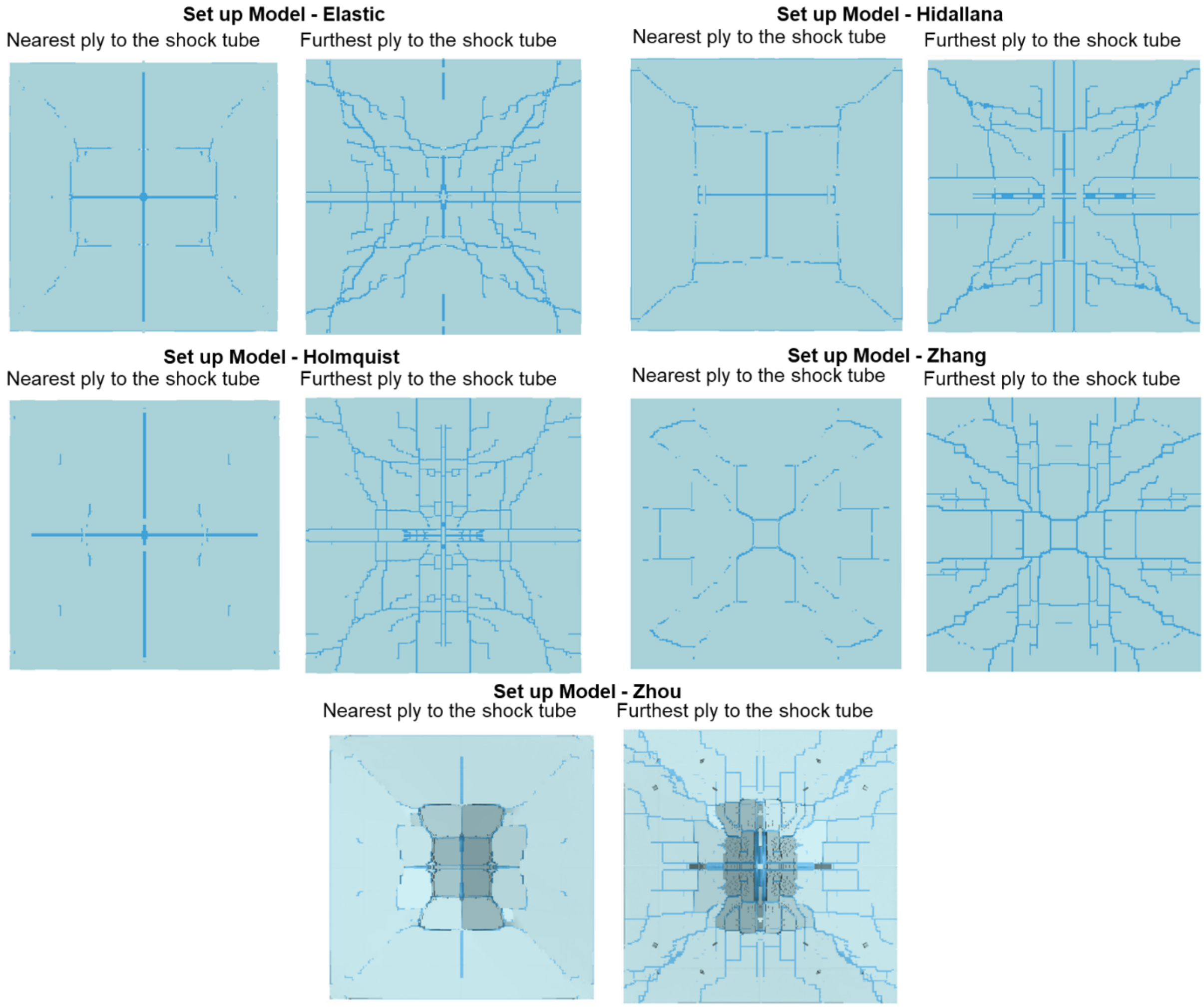

Figure 42: Destructive tests from numerical simulations for 88.4 laminated glass with a 40 g charge

3.5.3. 1010.4 Laminated glass

Figures **43** to **46** display the results for the 1010.4 laminated glass type. In **Figure 44**, similar to the 88.4 glass type, the Zhou et al. [67] model setup for 1010.4 had the erosion criteria disabled.

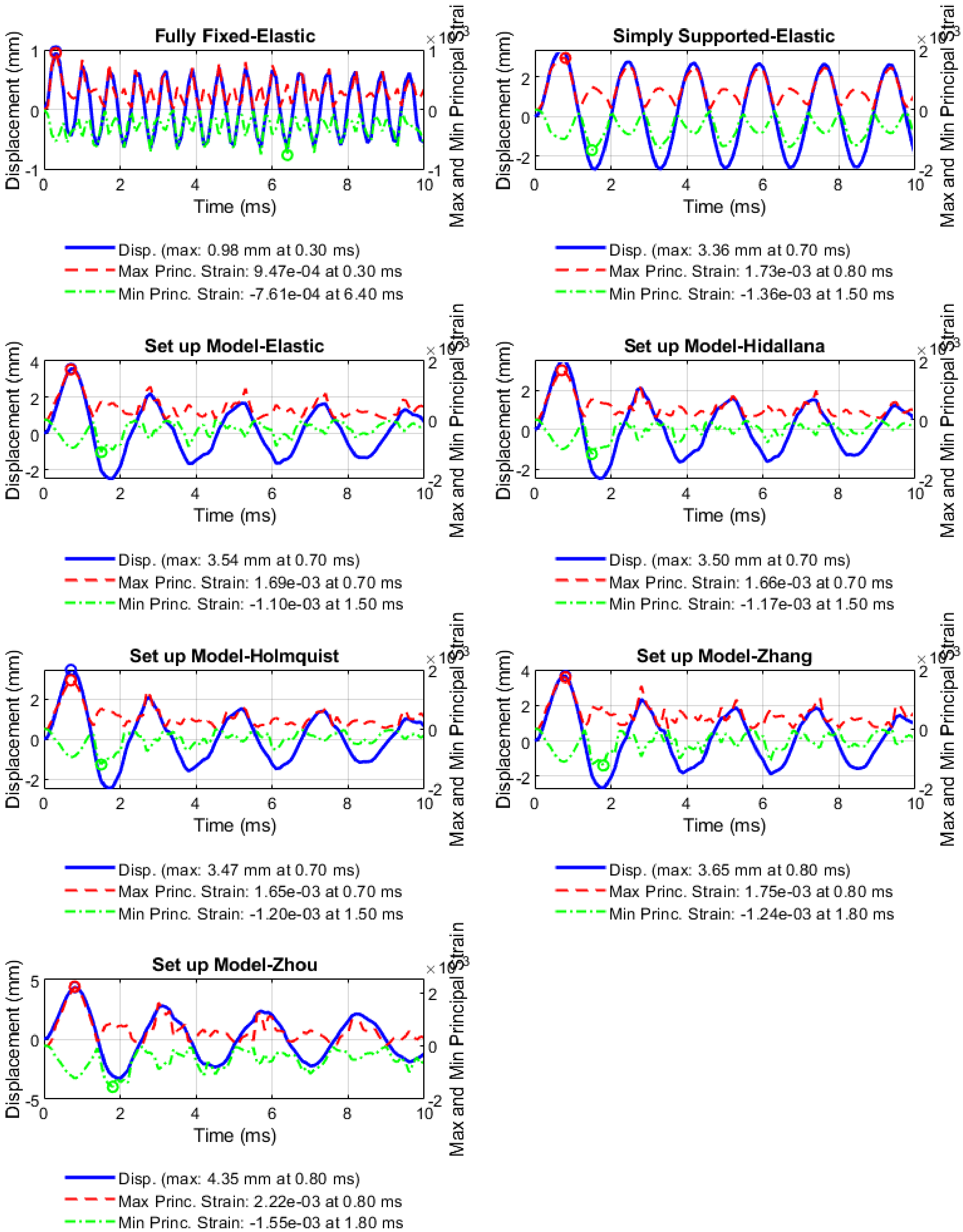

Figure 43: 1010.4 Laminated glass with a 20g charge

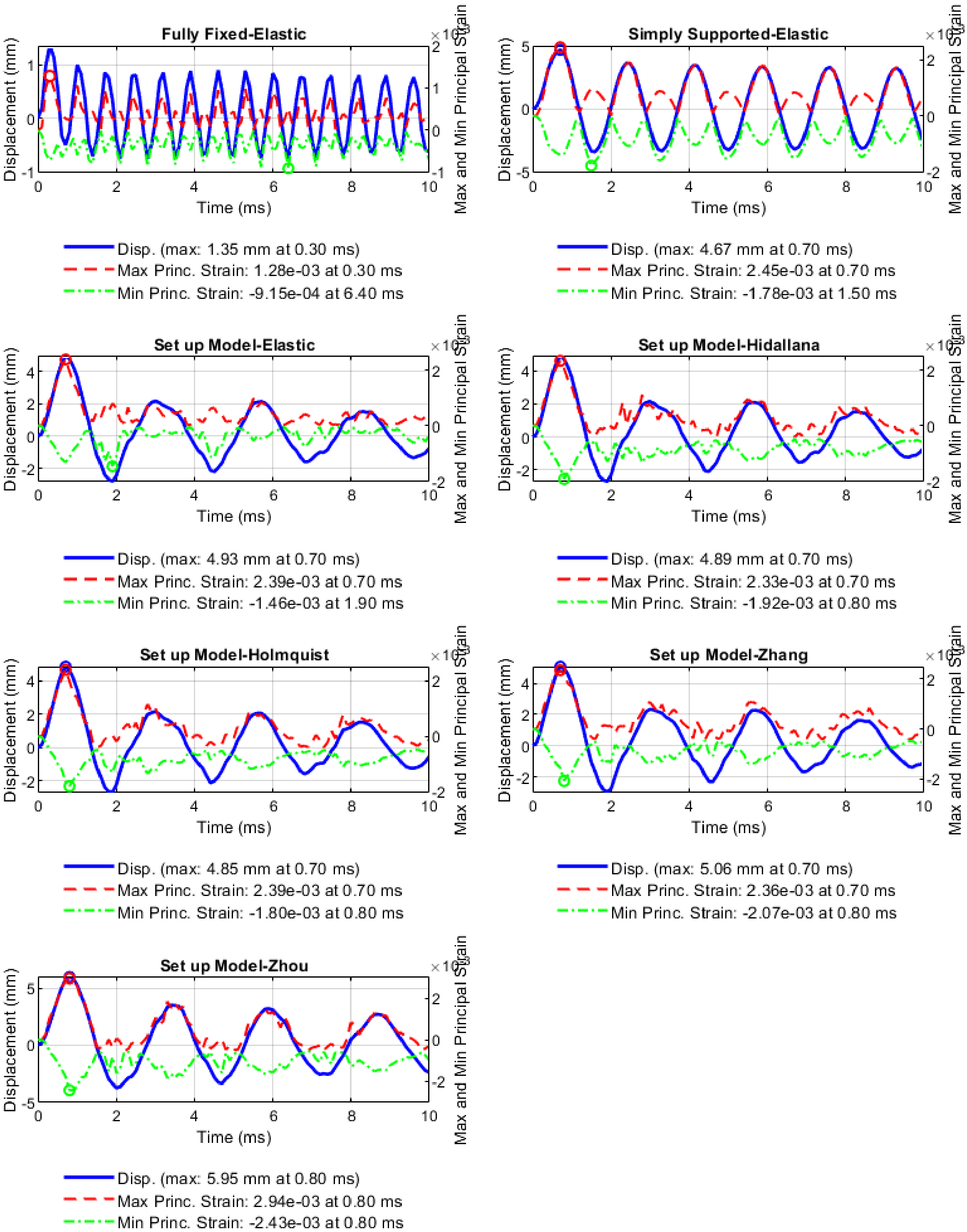

Figure 44: 1010.4 Laminated glass with a 30g charge

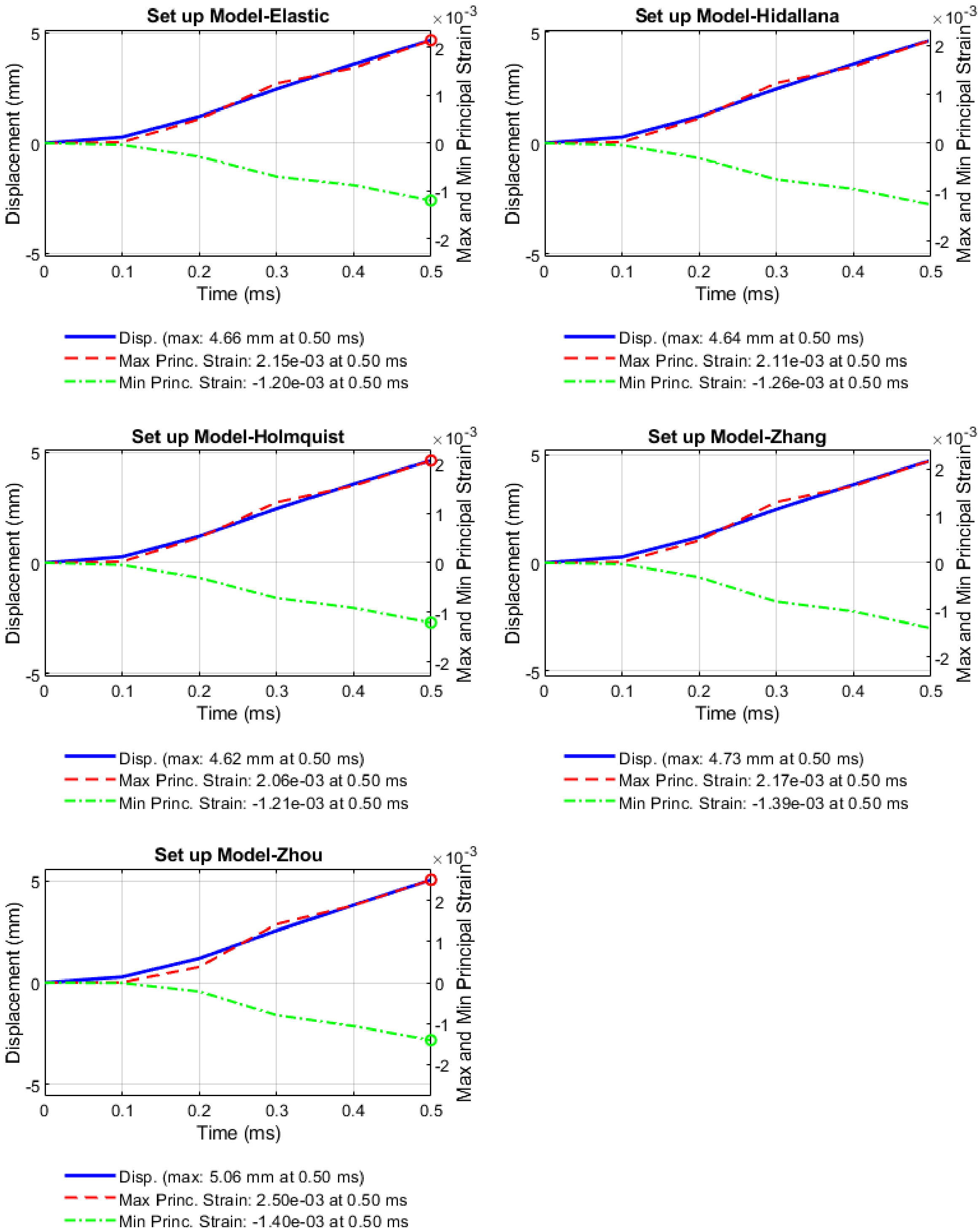

Figure 45: 1010.4 Laminated glass with a 40g charge

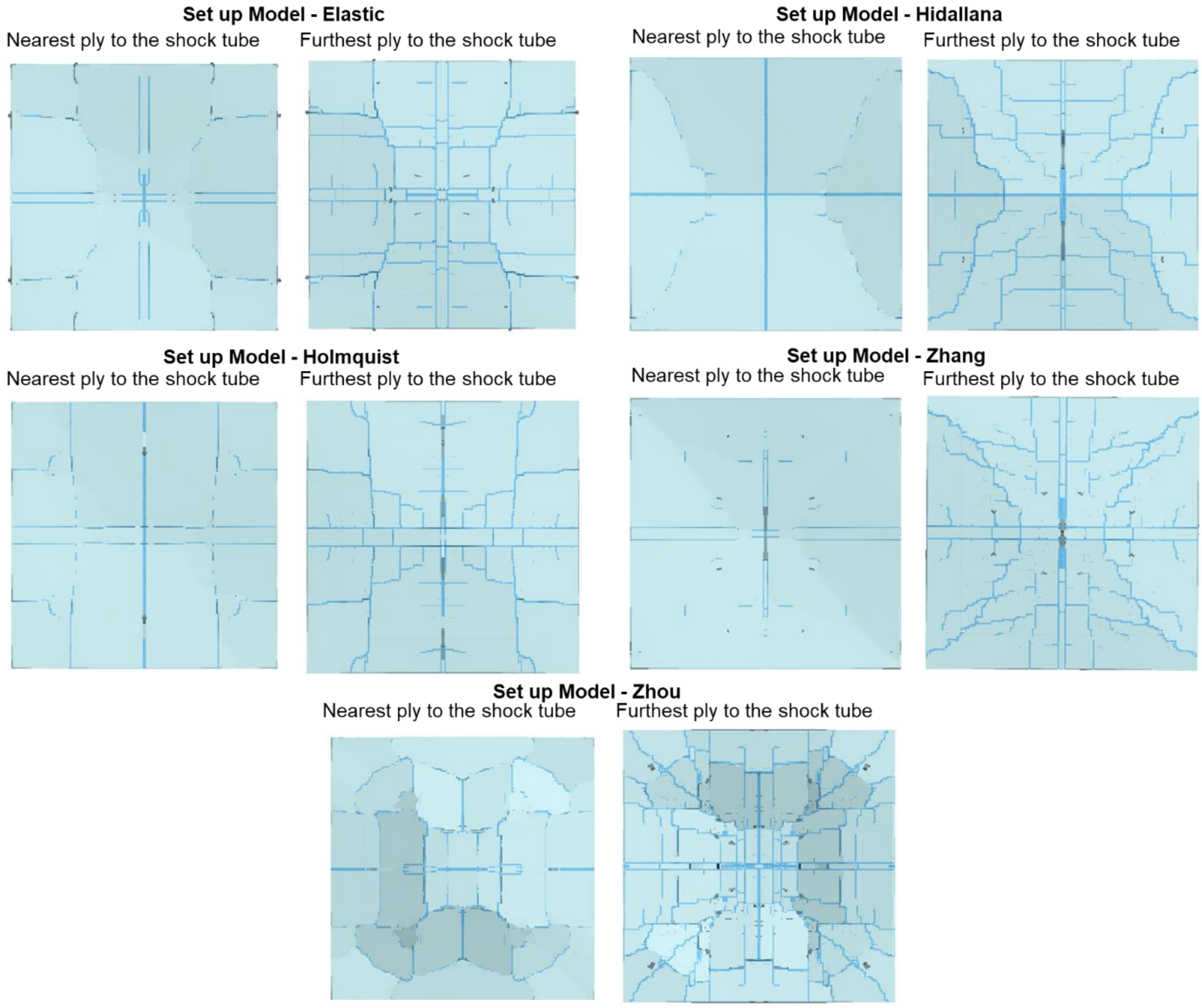

Figure 46: Destructive tests from numerical simulations for 1010.4 laminated glass with a 40 g charge

4. Experimental Tests

The testing campaign was carried out at the Competence Centre for Infrastructure Protection (CCPI), located at the Military Academy in Amadora. Explosive materials were always transported, stored, and handled by qualified military personnel in accordance with the safety standards of the Portuguese Army. The experimental program presented below aims to contribute to the development of the project SAERFA.

4.1. Characterization of the Explosion

This experimental campaign aimed to characterize the action of the explosion by defining the peak reflected pressure, p_r, duration of the positive phase, t_0, and the decay coefficient of the curve, *b*.

The main objective was to assess the analytical methods developed for characterizing explosion effects in the laboratory using an EDST and to define the associated parameters.

Thus, tests were carried out, aimed at characterizing the reflected pressure using the EDST, with dimensions 300x300x1500 mm³. Several tests were conducted, varying the explosive charge with weights of 10 g, 20 g, 30 g, 40 g and 50 g at a distance of the tube entrance of 0 cm.

The explosive used consists of PE-4A, a malleable plastic explosive based on RDX, supplied in 230 g sticks. It is characterized by a detonation velocity of 7000 m/s and a density of 1.4 g/cm³ [69]. The firing system is composed of an instantaneous electric detonator N.º8, as seen in **Figure 47**, which contains approximately 1 g of TNT equivalent [70]. The detonators and all test cables were tested using an AM573EUR digital multimeter to ensure the safety of the tests and proper circuit connections.

Figure 47: Box with eight instantaneous electric detonator N.º8

The explosive was weighed using a KERN® EWJ 6000-1SM precision balance, as seen in **Figure 48**, with a maximum weighing range of 6000g and a readability and repeatability of 0.1g, resulting in a measurement uncertainty of ± 0.05g [71]. To better maintain the round shape and keep all the explosive in place, it was inserted into a piece of latex glove, with a hole made to allow the detonator to be inserted, as seen in **Figure 49**.

Figure 48: 10g of PE-4A weighed on a precision balance

Figure 49: 10g, 20g, 30g and 40g of PE-4A enveloped in latex

4.1.1. Measurement of reflected pressure – EDST 300x300x1500 mm^3

The experimental setup consists of an EDST with a quadrangular cross-section, having dimensions of 300x300x1500 mm³. It includes four high-frequency ICP® pressure sensors - three model 113B24 and one model 113B22 – mounted on an aluminium reaction plate with dimensions of 586x506x10.2 mm³. This reaction plate has precisely placed holes for sensor placement and is supported by 14 extruded aluminium profiles, 80x80 mm², forming a supporting structure. The sensors, mounted on the reaction plate, are positioned 2 mm from the shock tube's exit while the explosive charge is located at the entrance (0 cm), supported by an auxiliary structure. The 2 mm distance between the EDST and the reaction plate was chosen to prevent the EDST from being projected against the plate during the explosion, which could damage the setup. A larger distance could cause part of the shock wave to dissipate before reaching the sensors. These details are illustrated in **Figure 50**.

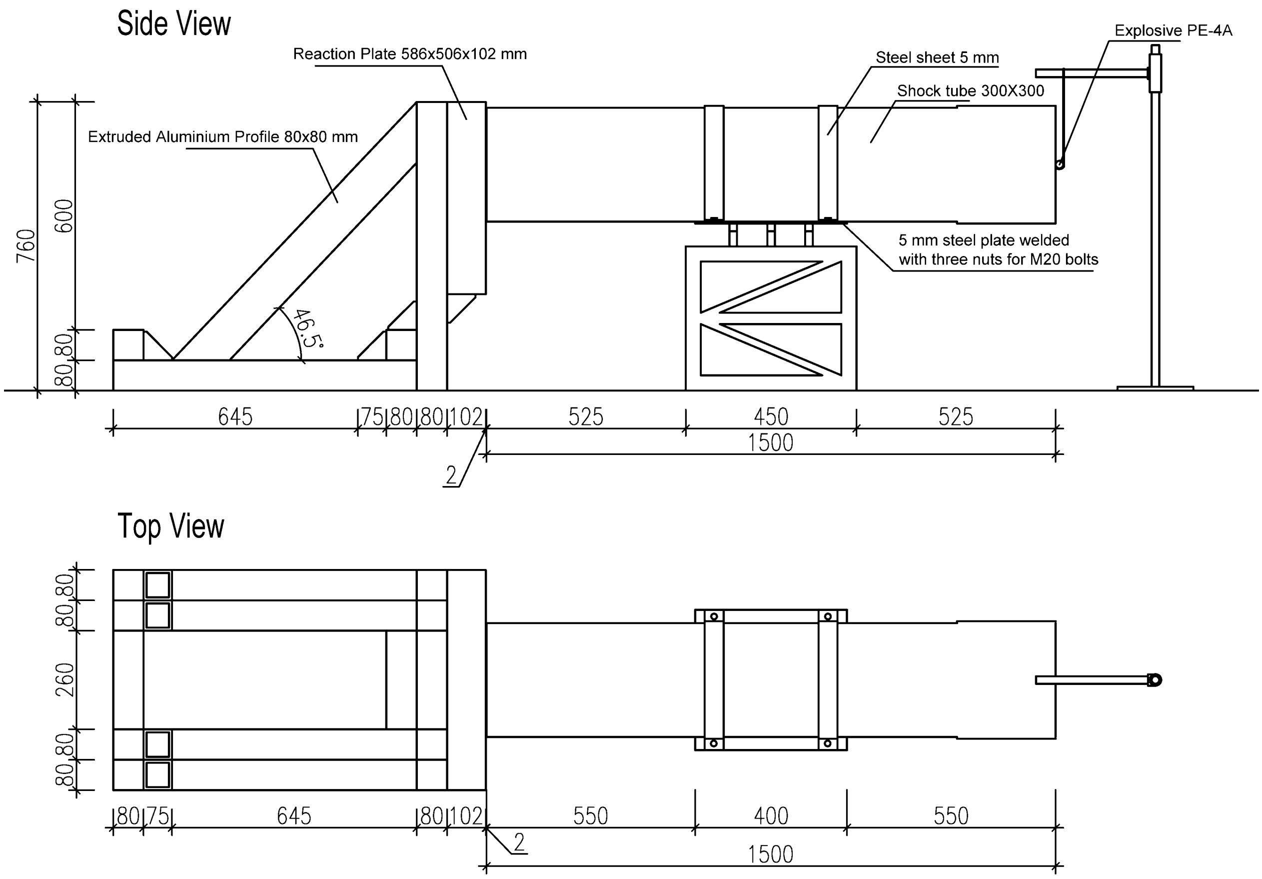

Figure 50: Scheme with side and top view of the reflected pressure test, at a scale 1:20; all measurements are in millimeters

Figure 51: Reflected pressure test setup

Regarding the placement of the sensors on the reaction plate, the holes aligned with the tube's section, as shown in **Figure 52** were chosen. This positioning was intended to ensure that the shock wave at the EDST exit was as close to a flat shock wave as possible.

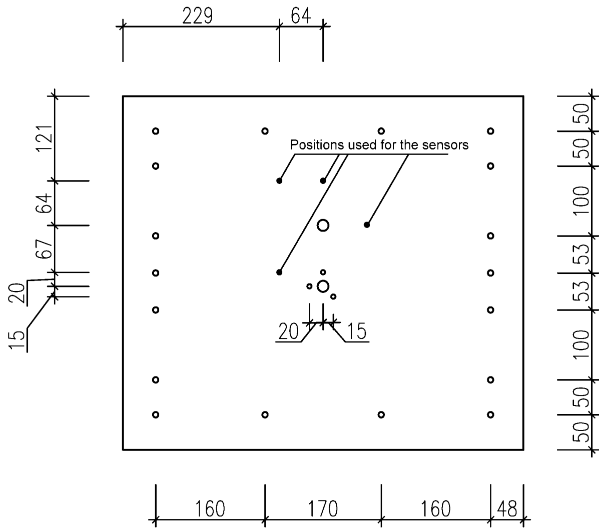

Figure 52: Scheme of the front side of the reaction plate and sensor placement, at a scale of 1:10; all the measurments are in millimeters

Figure 53: Backside of the reaction plate with sensors in place

For this test, both ICP® pressure sensors models 113B22 and 113B24 were used to measure the reflected pressure caused by the explosion. These sensors are specifically designed for high-frequency applications, such as measurements in shock tubes. They both utilize a quartz piezoelectric element from series 113, with acceleration compensation coupled to a miniature electronic source follower. The sensors' high natural frequency and frequency adaptation provide an extremely wide usable frequency range (greater than 100 kHz), and they feature an exceptionally fast response time (1 μs) and virtually non-resonant response characteristics.

The key difference between the two models lies in their sensitivity: the 113B22 model has a sensitivity of 0.145 mV/kPa, making it suitable for measuring higher pressure ranges, while the 113B24 model, with a higher sensitivity of 0.725 mV/kPa, is better suited for precise measurements at lower pressure levels. The higher sensitivity of the 113B24 allows it to detect smaller changes in pressure more accurately, making it ideal for capturing finer details in lower pressure environments [72,73]. The specifications for the ICP® pressure sensor models are listed in **Table 3**.

Table 3: Specifications of the ICP® Pressure Sensores adapted from [72,73]

Model	Sensitivity (± 10%) [mV/kPa]	Overrange (± 10V) [kPa]	Max. Pressure [kPa]	Arrival Time [μs]
113B22	0.145	68950	103425	≤1.0
113B24	0.725	13790	68950	≤1.0

The sensors were connected to a signal conditioner from PCB Piezotronics by BNC cables. As the tests were conducted in separate, the cables were routed through a wall using a junction box that facilitated the connection between the test room and the instruments room. The model used was a 482C15, designed to work with the ICP® Pressure sensors mentioned above. Its main function was to provide constant current to the sensors in the reaction plate and amplifying the output signals. It is connected to a data acquisition system and a power supply [74], as seen in **Figure 54**.

Figure 54: Connected signal conditioner, model 482C15

The Breach MC system is a small, lightweight, safe and reliable short range (~1km) radio firing system and consists of 1 Transmitter Controller (Breach MC TX) and up to 10 Remote Firing Devices (Breach MC RX-ST). The Transmitter Controller can control up to 10 remote firing devices either individually or as a group/all fire and it is battery-powered [75].

Figure 55: Breach MC system - remote firing device (Breach MC RX-ST) connected to the PXIe Platform at the top and the transmitter controller (Breach MC TX) at the bottom of the picture

The box is a PXIe Platform developed by “Bridgepoint – Sistemas de Engenharia” to the Portuguese Military Academy. It is a modular instrumentation platform used for measurement and precise data acquisition applications with high data transfer rates and synchronisation capabilities, as seen in **Figure 56** . It is directly connected to the remote firing device by a twisted pair cable.

Figure 56: PXIe Platform developed by “Bridgepoint – Sistemas de Engenharia”

To digitalize the data from signal conditioner, a data acquisition system device made by National Instruments was used, model NI6361 from the X Series DAQ line. This device can measure electrical signals from multiple analog inputs for example as the signal conditioner mentioned above, as seen in **Figure 57** by a BNC connector (coaxial cable), and output them as digital information, or vice-versa. It has a high sampling rate, which is essential for capturing fast-changing signals accurately without missing critical data. The system functions as an interface between the physical world and a computer. On the back side has an USB cable that connects to the computer [76].

To trigger the data acquisition system and provide power supply, an intermediate device, the Photron FASTCAM mini AX100, was used. The camera’s trigger switch is connected to the Bridgepoint trigger out, and the Output 2 (Trg TTL out) is connected to the digital input of the data acquisition system NI6361. This camera is a high-speed camera designed for capturing ultra-slow motion video with an high frame rate and light sensitivity. The sensitivity in low light conditions allows the camera to eliminate the rolling shutter effect in fast-moving objects [77]. The camera is also connected to a power supply.

Figure 57: Data acquistion system NI6361 and the Photron FastCam mini AX100 at the top

The scheme in **Figure 58** explains all the information mentioned before:

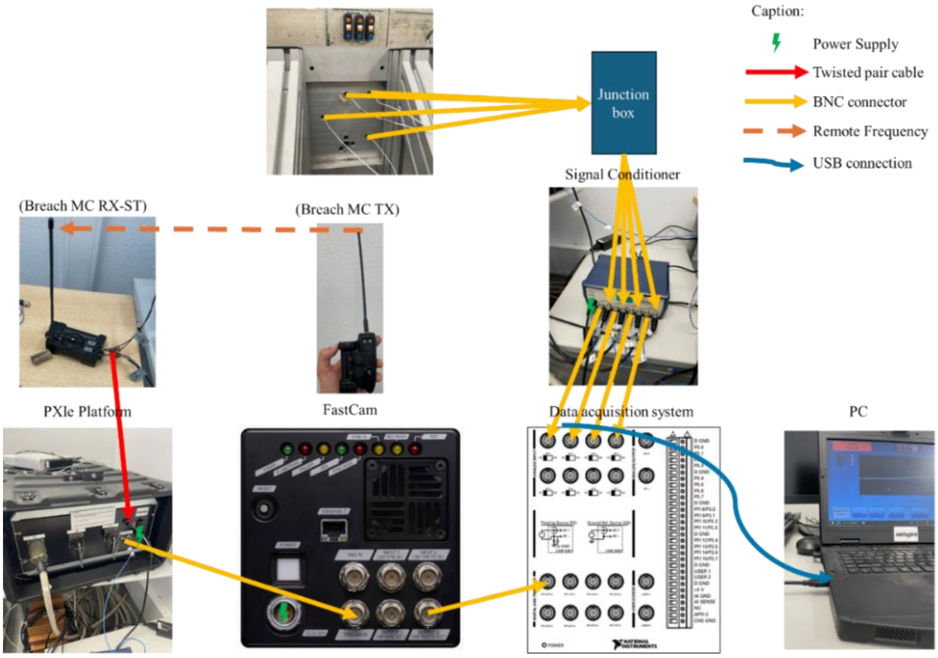

Figure 58: Scheme with a visual representation of connections for the reflected pressure test, some figures were adapted from [76,78]

4.1.2. Obtained results

The quantitative results of the reflected pressure measurements from the sensors are presented, along with an evaluation of their dispersion through relative uncertainty. The aim is to compare the obtained experimental results with the analytical expressions described in chapter 2.3, in order to infer their accuracy. The number of tests is presented in **Table 4**. For the 50g, only one test was conducted, as the first test with that weight caused damage to the structure.

Table 4: Number of tests done and valid results

Charge weight (g)	Number of tests done
10	4
20	4
30	4
40	3
50	1

The obtained data were processed and adjusted using the least square fit of the modified Friedlander equation (Equation (2.6)), with parameters obtained through this method. This approach allowed for determining the peak reflected pressure, p_r, the duration of the positive phase, t_0, and the curve decay coefficient, b. Using the average results from the experimental data, it is possible to calculate the reflected impulse using the Equation (2.7), as presented in **Table 5**:

Table 5: Average results from the experimental tests

Charge weight (g)	$\overline{P}_{max}$ (MPa)	$\overline{t}_0$ (msec)	$\overline{b}$	Reflected Impulse, i_s (MPa×msec)
10	0,79	2,07	2,45	0,42
20	1,65	2,02	3,09	0,74
30	2,26	1,73	2,29	1,04
40	3,12	2,35	5,19	1,14
50	4,38	2,29	5,99	1,40

To better understand the accuracy of the data obtained from the tests, it is important to evaluate the relative uncertainty of the data (the difference between the most extreme result and the mean) and their distribution. Regarding the uncertainty, it is noted that it is relatively high, which may be due to the placement of each specific sensors in the reactive plate.

Table 6: Relatitvely Uncertantly of the experimental tests

Charge weight (g)	$\overline{P}_{max}$ (MPa)	Relative Uncertainty (%)	Impulse (MPa×msec)	Relative Uncertainty (%)
10	0,79	27,00	0,42	32,00
20	1,65	24,36	0,74	40,34
30	2,26	29,62	1,04	34,53
40	3,12	18,24	1,14	15,53
50	4,38	5,64	1,4	9,73

Despite the high uncertainty, when computing the dispersion of the experimentally obtained values, it can be observed that most values fall within a 10% range of the average result. This indicates a reasonable level of consistency in the test accuracy. The graphs from figures **59** to **64** illustrate the distribution of the data for different charge weights.

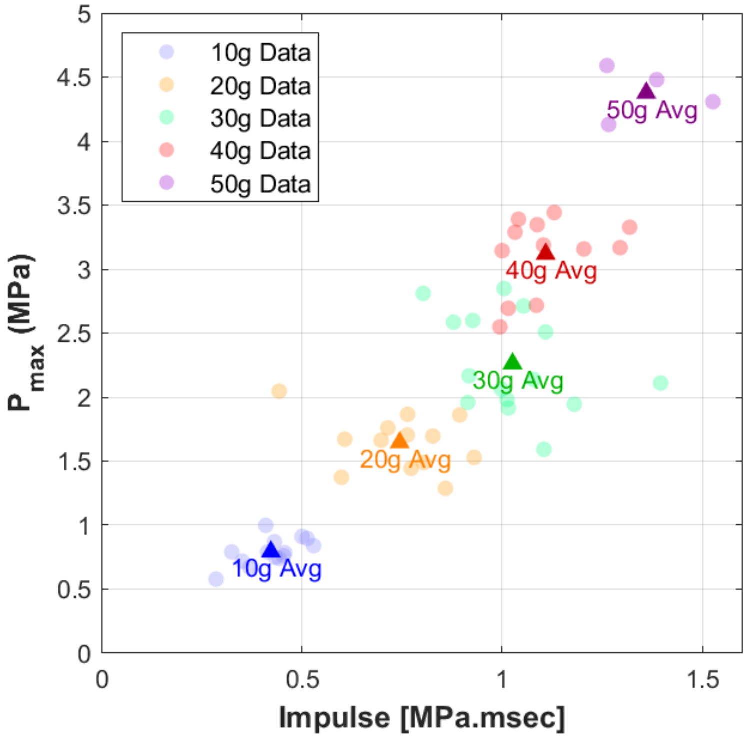

Figure 59: Reflected pressure test

The histogram for the 10g charge shows that the maximum pressure distribution is relatively centred, with most data points falling within 10% of the mean. This suggests a high level of consistency in the sensor readings for this charge weight.

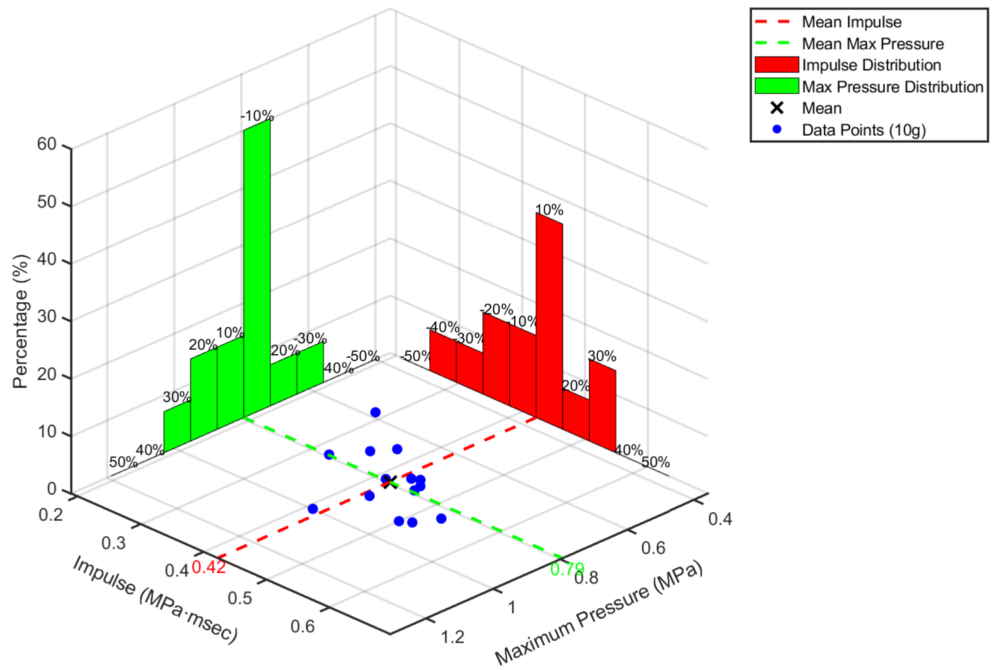

Figure 60: Histogram for 10g charge

For the 20g charge, the data points are more dispersed than those for the 10g charge, as the impulse and pressure distribution show a broader spread.

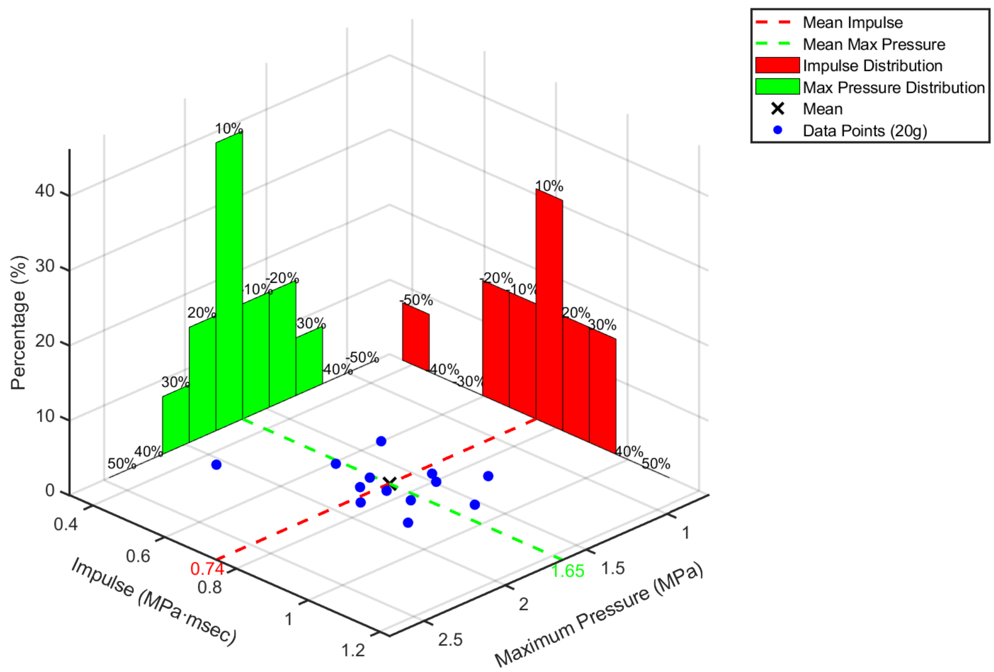

Figure 61: Histogram for 20g charge

The 30g charge histogram reveals a broader spread in the maximum pressure distribution, with more values deviating from the mean, even though, the impulse distribution remains relatively well-centred.

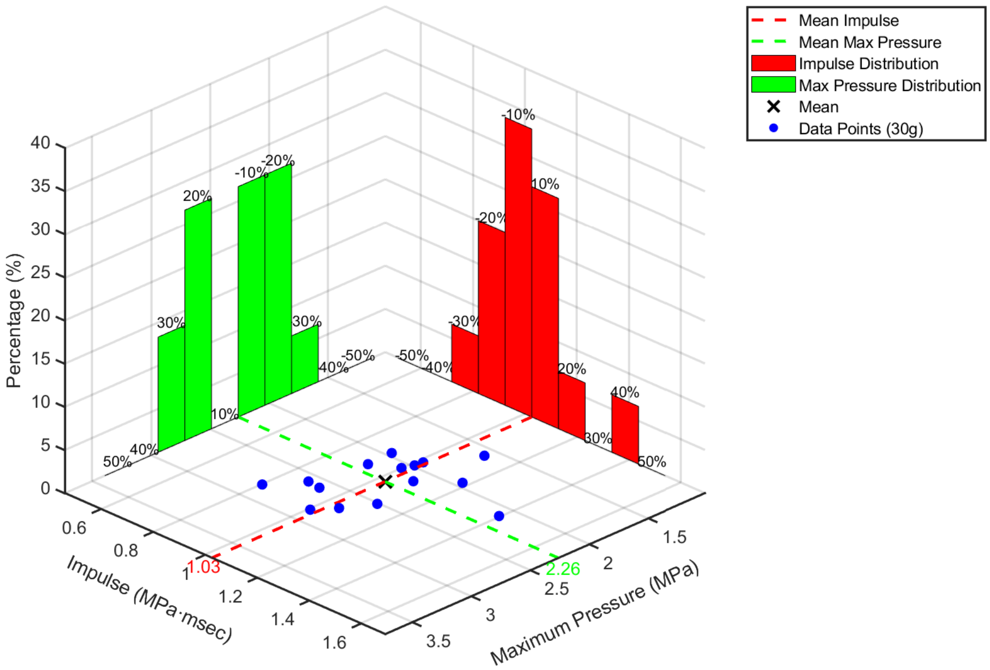

Figure 62: Histogram for 30g charge

The 40g charge shows a tighter grouping around the mean in the impulse and pressure distribution, with the majority of the data points being within 10% of the average.

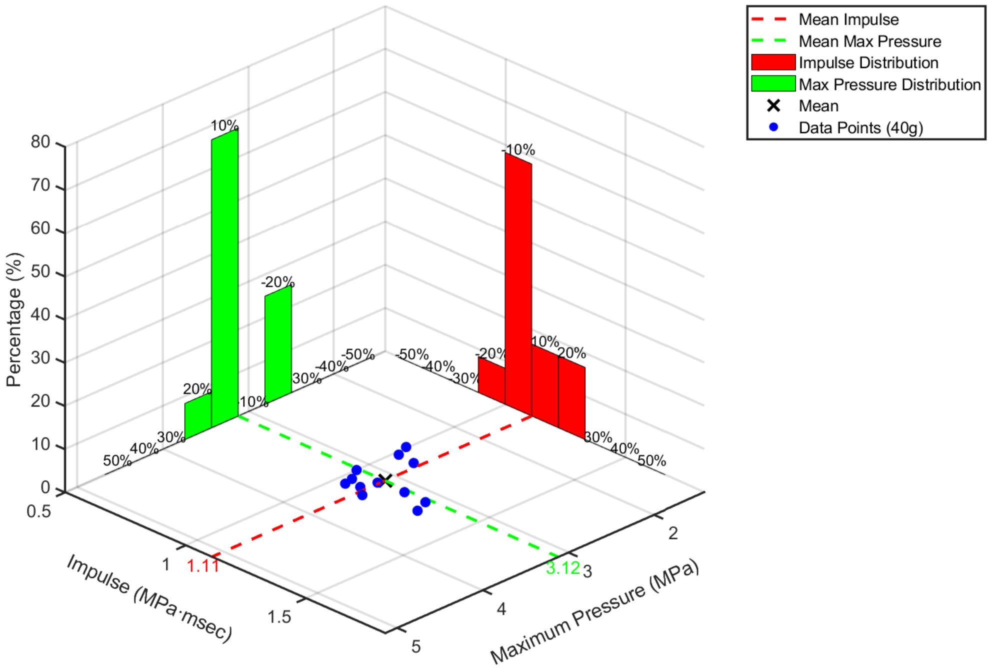

Figure 63: Histogram for 40g charge

The 50g charge, despite being limited to one test, shows a relatively narrow distribution for both maximum pressure and impulse, this may be due to the limited number of data points but suggests that the single test was consistent.

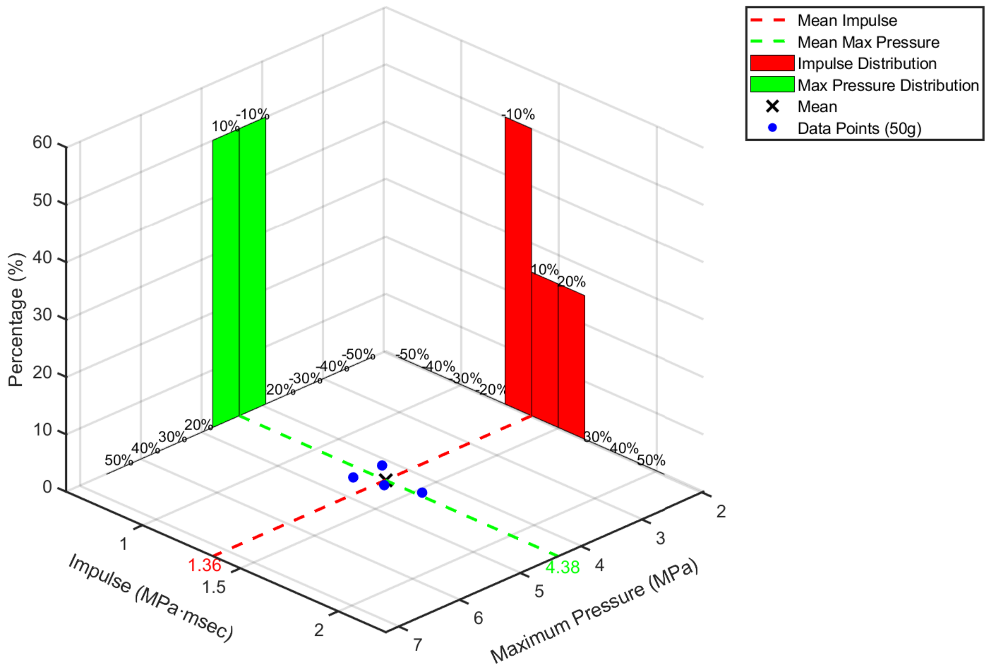

Figure 64: Histogram for 50g charge

Comparing the experimentally obtained values with the analytical predictions discussed in Chapter 2.3 allows for an assessment of the accuracy of the results. The first step involves converting the applied charge to an equivalent mass of TNT, considering both the charge used in the tests and the charge in the detonator. The analytical values for reflected pressure are derived from Liu et al. [52], which involve the combination of equations (2.24) and (2.9). This analytical model is then compared with the experimental results to evaluate its accuracy.

The values presented in **Table 7** illustrate the deviation between the analytical and the experimental results, expressed as a percentage of the experimental values. The model proposed by Liu et al. [52] appears to be consistent regarding the reflected pressure; however, it tends to overestimate the pressure up to a reduced distance of 3.5 m³/kg, after which it underestimates the pressure, as seen in **Figure 65**. This difference may be due to the fact that Liu's formula was developed for a specific tunnel geometry, which is not quadrangular.

Table 7: Comparison between analytical and experimental values for reflected pressure

Charge (g)	**W (g)**	**Z_{EDST} (m^3/kg)**	**$\overline{P}_{max}$ (MPa)**	**P_r Liu et al.** [52] **(MPa)**	**Error (%)**
10	15,00	11,46	0,79	0,96	-20,77
20	29,00	5,93	1,65	1,69	-2,91
30	43,00	4,00	2,26	2,38	-5,35
40	57,00	3,02	3,12	3,04	2,54
50	71,00	2,42	4,38	3,67	16,24

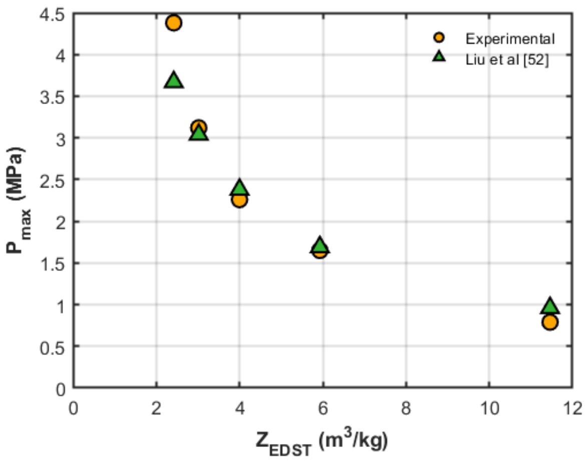

Figure 65: Comparison of analytical and experimental values for reflected pressure

4.2. Tests with the glass panels

The testing campaign aimed to characterize the dynamic behaviour of various laminated glass panels with different thicknesses against explosions. For this purpose, three geometries of laminated glass were used: laminates with 6mm, 8mm, and 10mm glass layers, all with a 1.52mm PVB interlayer. To obtain the dynamic response, the EDST with dimensions 300x300x1500 mm³ was used, whose study and characterization were detailed in the previous section (4.1).

The test glass panels were supplied by Vidreira Algarvia, part of the Climalit network under the Saint-Gobain Group. Saint-Gobain is one of Europe's leading glass manufacturers, with more than 180,000 employees, primarily focused on glass production. The group also operates in sectors such as insulation, construction materials, plumbing, packaging, reinforcing fibers, ceramics, abrasives, plastics, and specialized distribution. Some of their notable projects include the Louvre Pyramid, the European Parliament, and the Berlin Chancellery. Vidreira Algarvia is an industrial glass company based in Portugal, serving markets in both Portugal and Spain. With a workforce exceeding one hundred employees, it offers a wide range of possibilities for constructors or project designers [79,80].

The glass tested was thermally reinforced and designed to reduce the risk of injury by breaking into small, less harmful pieces in the event of fragmentation. This type of tempered glass has high flexural strength due to the strong compression treatment it undergoes. It was part of a laminated assembly with four PVB films, which hold the glass fragments together upon breaking. The components are tempered before being laminated [80].

According to the glass manual, the glass was made from soda-lime-silica, composed of 70 to 72% vitrifying component (silica) in the form of sand, 14% flux (soda in the form of carbonate and sulphate), 10% stabilizer (lime in the form of limestone), and other oxides such as alumina or magnesium to enhance its physical properties. These components give the glass a density of 2500 kg/m³, a compressive strength of 1000 MPa, and a flexural strength suggested to be between 120 and 200 MPa. The Young's modulus, representing tensile strength, is 70 GPa, and the Poisson's ratio is 0.2 [80].

The primary objective of this testing campaign was to analyse the deformation capacity of glass panels.

4.2.1. Experimental setup

The experimental setup consists of the EDST with a quadrangular section, measuring 300x300x1500 mm³, and a support structure for the glass panel defined by SHS (Square Hollow Section) 50x3 mm profiles bolted to an OSB (Oriented Strand Board) panel with M6 screws. Between the SHS 50x3 profiles, a 20mm steel plate is welded at the front (closest to the EDST), as seen in **Figure 66**. At the back of the structure, there are four 10mm thick steel plates bolted to the 20mm steel plate. The glass panels under study are placed between these two plates, with a rubber layer to cushion the contact, as seen in **Figure 67**. The propose of the OSB panel was to stop the light arising from the detonation of the explosive to interfere with the cameras and lasers.

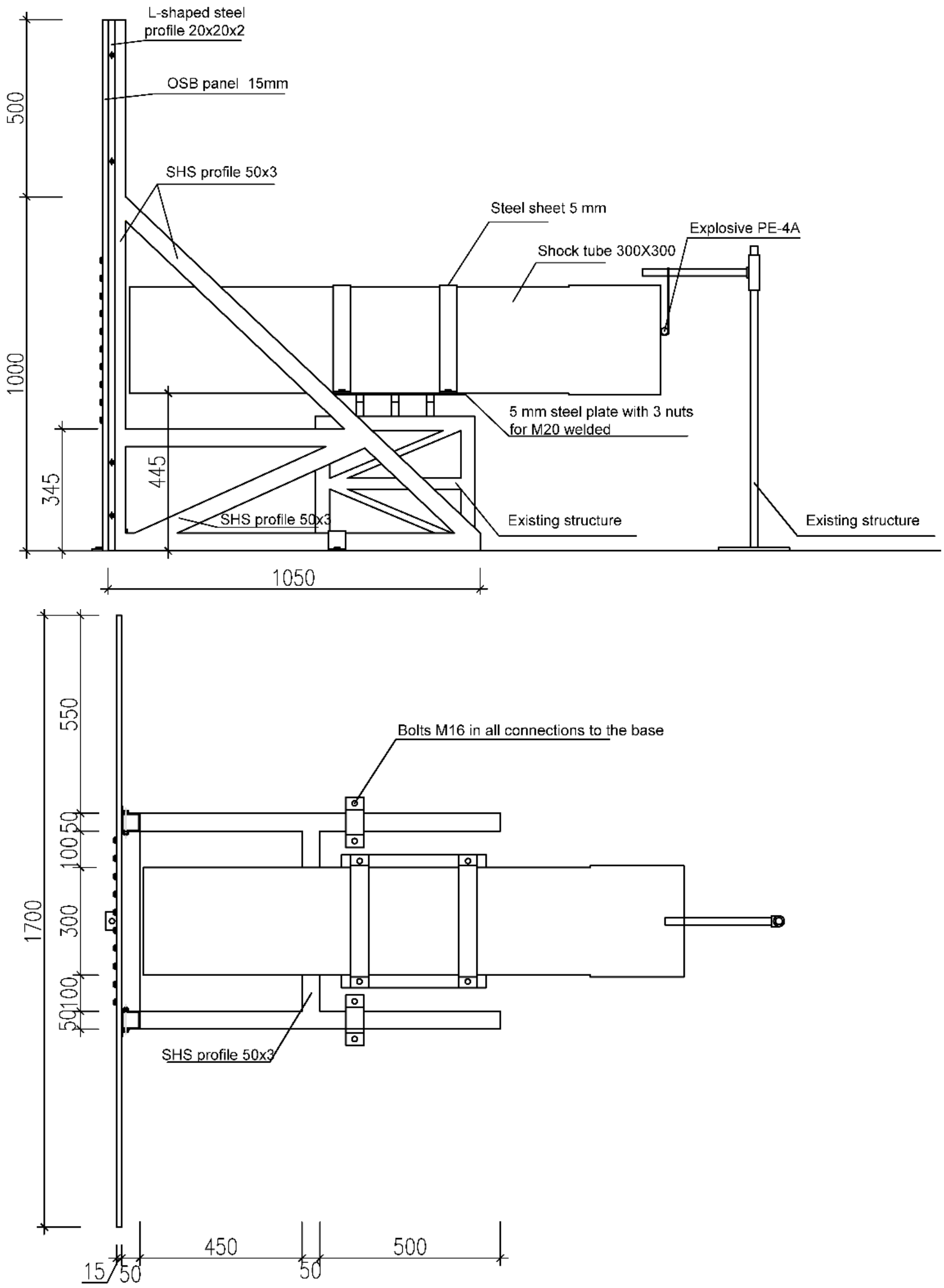

Figure 66: Schematic with side and top views of the glass panel test setup, scaled 1:20; all measurements are in millimeters

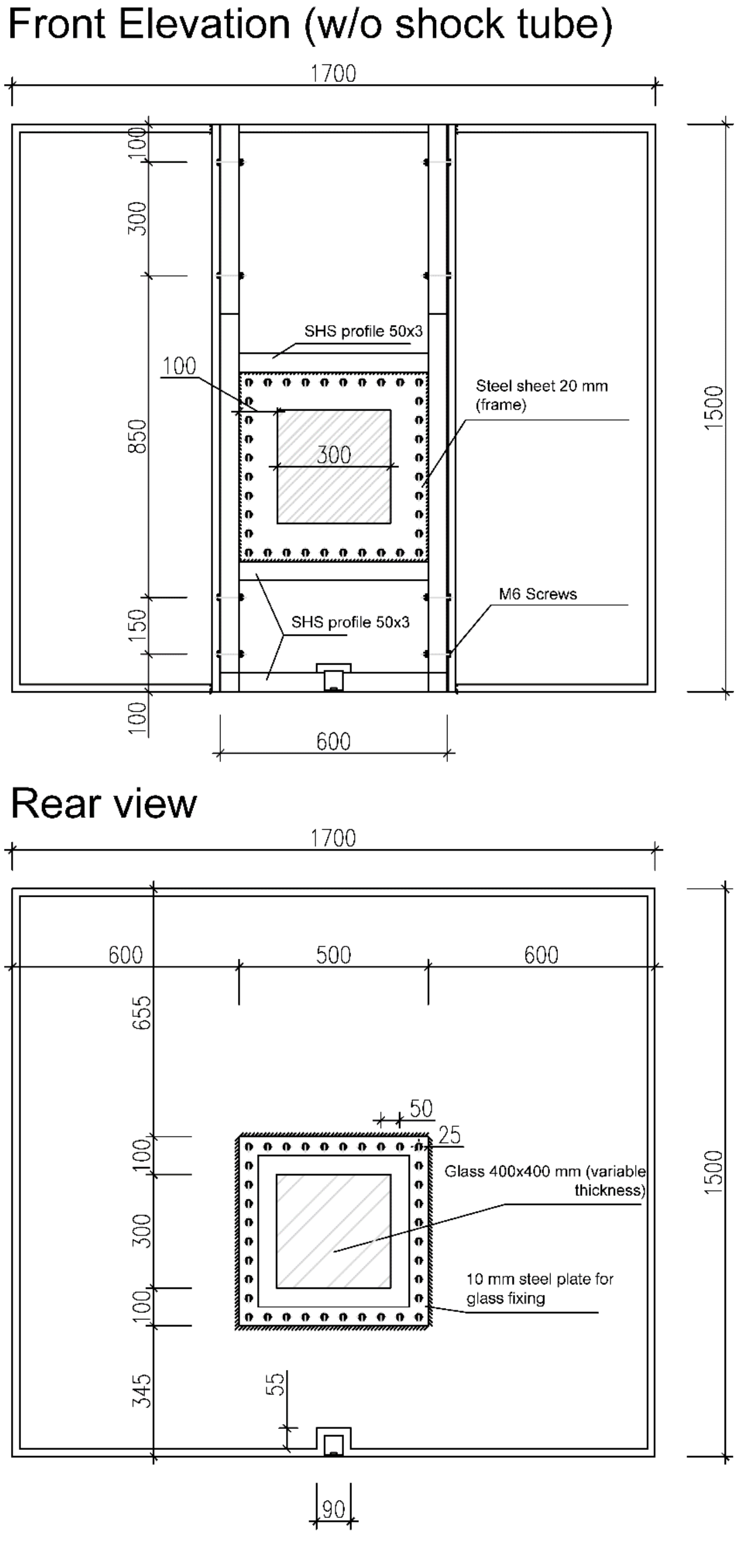

Figure 67: Front elevation and rear view of the structure holding the glass panels, scaled 1:20; all measurements are in millimeters

The fixation system is crucial for mitigating contact between the glass panel and its support structure, ensuring that poor connections do not compromise the experimental results, by using a rubber layer. The steel plate is attached to the support structure using 10 mm diameter threaded steel rods, as depicted in **Figure 68** and **69**. In this experimental setup, a 10 mm thick mobile steel plate, shown in **Figure 70**, was used to secure the glass panel along all four edges.

These threaded rods are equipped with two nuts: one secures the rod to the mobile steel plate, and the other attaches it to a 20 mm steel frame, which is welded to the base structure. This assembly, described in subchapter 2.2.2 is referred to as a mechanical system utilizing bolted supports. The final configuration of this system is illustrated in **Figure 71**.

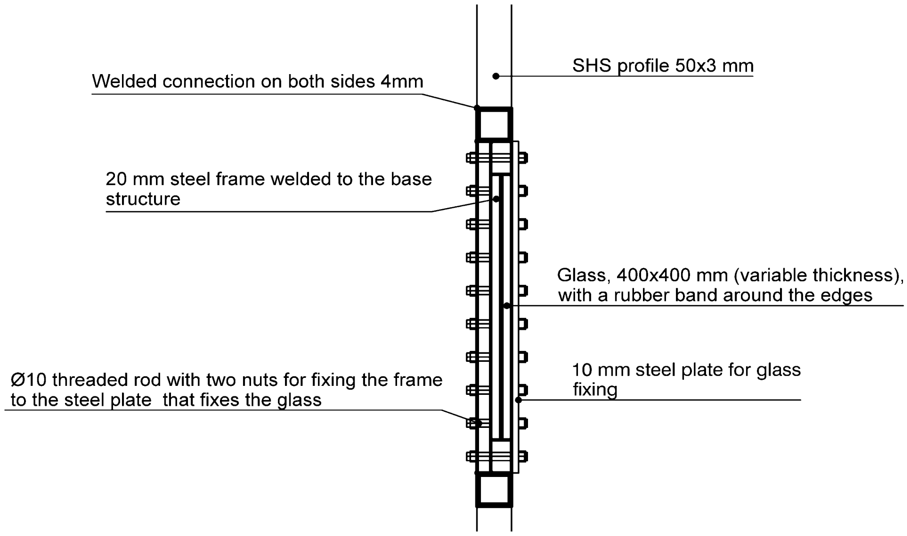

Figure 68: Lateral view of the fixation system at a scale of 1:10

Figure 69: Steel frame with threaded rods with the shock tube in the background

Figure 70: 10 mm thick mobile steel plate

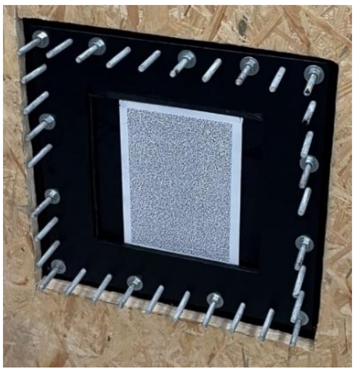

Figure 71: Final assembled system

As shown in **Figure 71**, a paper with a stochastic pattern is glued to the glass panel to enhance the accuracy of the data captured by high-speed cameras. This pattern features a predefined design that facilitates its identification in the images. Additionally, the side of the glass facing the shock tube was sprayed with black paint to prevent light from the explosion from affecting the camera recordings.

At the rear of the structure, two high-speed cameras (Photron FASTCAM Mini AX100) were used to capture the glass's behaviour during the explosion. The data from the cameras were processed using VIC-3D software, which is designed for measuring and visualizing full-field, three-dimensional shape, displacement, and strain based on the principle of digital image correlation (DIC) [81]. To ensure sufficient brightness in the images, a flicker-free spotlight, the BOXER model from Nyla, was utilized. This lighting system operates flicker-free at any frame rate with 100% output, and a transparent protection barrier was placed in front of the spotlight to absorb the shock wave [82], as shown in **Figure 72**.

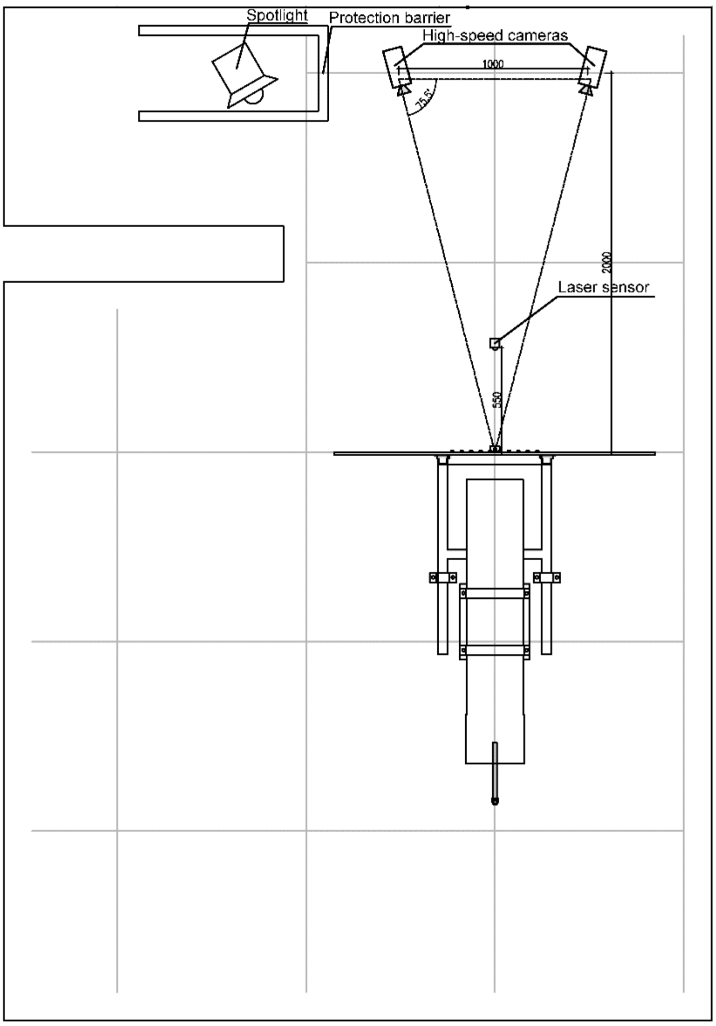

Figure 72: Layout of the structure, scaled 1:40; all measurements are in millimeters

The cameras were programmed to capture 20,000 frames per second at a resolution of 384 by 384 pixels, with an exposure duration of 1/40000 seconds to avoid "motion blur." Positioned at an angule to the setup, the cameras were strategically illuminated by the spotlight, as depicted in **Figure 73**, enabling accurate recording and analysis of the glass panels' behaviour during the explosion.

Figure 73: Ilumination and recording system

The cameras were divided into a main and a secondary unit. The secondary camera received synchronization and trigger inputs from the main camera via BNC connectors. It was also connected to a TP-Link 5-Port Gigabit Easy Smart Switch (TL-SG105E) using an RJ45 cable for high-speed data transfer of the high-frame-rate video files. The managed switch was connected to a power supply and subsequently linked to the junction box and the computer. The main camera was connected to the PXIe Platform, as described in the reflected pressure test in subchapter 4.1.1. The complete camera setup and connections are illustrated in **Figure 74** [83].

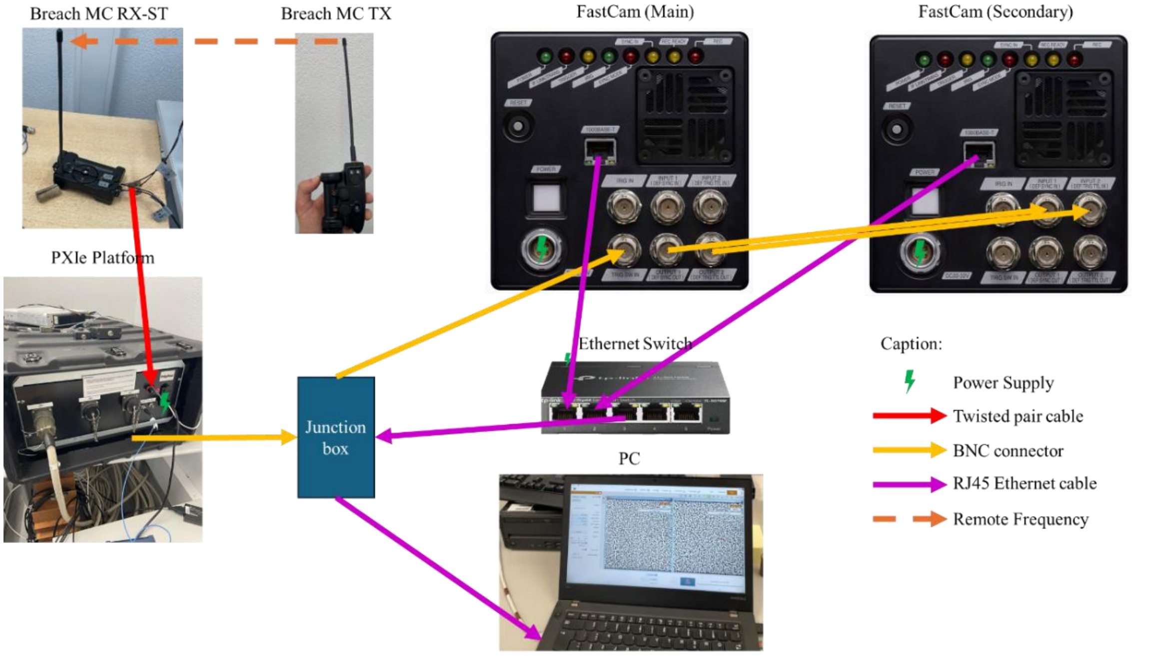

Figure 74: Scheme with a visual representation of connections for the cameras setup , some figures were adapted from [77,83]

The laser sensor used was the ILD 2310-50 by Micro-Epsilon, designed for accurate measurements within a 50 mm range, with a measuring rate adjustable via software, as shown in **Figure 75** [84].

Figure 75: Laser IDL 2310-50

To operate the laser sensor, it was connected via a PC2300-x/C-Box/RJ45, which serves as both a power supply and an output cable. This connection facilitated digital-to-analog conversion of the sensor's digital signal, providing an analog output through Ethernet, RS422, or USB. The entire system was connected to a computer via an RJ45 Ethernet cable, allowing operation through an Internet browser using a predefined IP address. Power was supplied by a UNO-PS/1AC/24DC/60W, a primary-switched power supply unit with worldwide compatibility, featuring short-circuit-proof and idling-proof capabilities [85]. This setup is depicted in **Figure 76**.

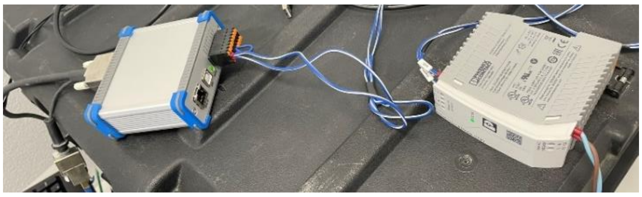

Figure 76: C-Box/2A and power supply

The diagram in **Figure 77** illustrates the complete laser setup, including all connections and components discussed above:

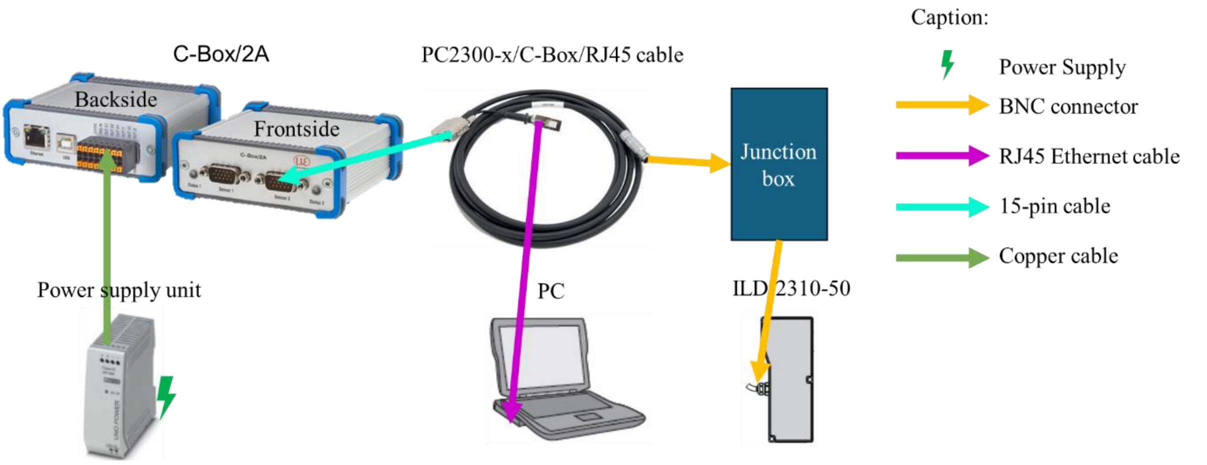

Figure 77: Scheme with a visual representation of connections for the laser setup, some figures were adapted from [84–86]

4.2.2. Obtained results

The following section presents both the quantitative and qualitative results of the conducted tests. To ensure the reliability of the experiment, each test was repeated at least twice. For the 88.4 laminated glass, four repetitions were conducted at the highest charge due to issues such as incomplete laser data recording and insufficient observed damage in some cases. Notably, for the 1010.4 laminated glass, damage was unexpectedly observed in the outer ply at the lowest charge (20g), even though all fragments remained attached, because of this only one test was done with a 30g charge. This unexpected result could potentially be due to pre-existing damage during transportation or assembly.

Table 8: Summary of the tests done

Glass	Charge weight (g)	Number of tests	Damage observed	Size of the Largest Fragment (cm)
66.4	**10**	2	No	
	20	2	No	
	30	2	(2/2) Outer ply broke (Most fragments remained attached) and inner ply got damaged, in both tests	1.5
88.4	**20**	2	No	
	30	2	No	
	40	4	1. (1/4) – Visible hole in the glass (through both glass plies and PVB) 2. (1/4) – Outer ply broke (Majority of fragments remained attached) 3. (1/4) – No damage 4. (1/4) – Outer ply mostly shattered (Majority of fragments detached), inner ply undamaged	2;1.5;4
1010.4	**20**	2	(1/2) – Outer ply shattered, all fragments remained attached, no damage to the inner ply	
	30	1	No	
	40	1	(1/1) – Visible hole in the glass (through both glass plies and PVB)	3.5

4.2.2.1 66.4 Laminated Glass

Figures **78** to **80** present data from all measurement systems and tests, including displacements and strains.

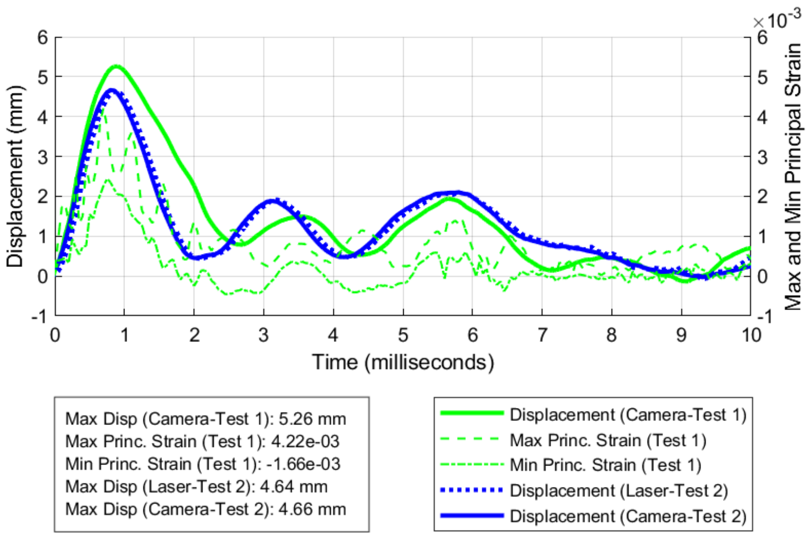

Figure 78: Data from the tests on the 66.4 laminated glass for a 10 g charge

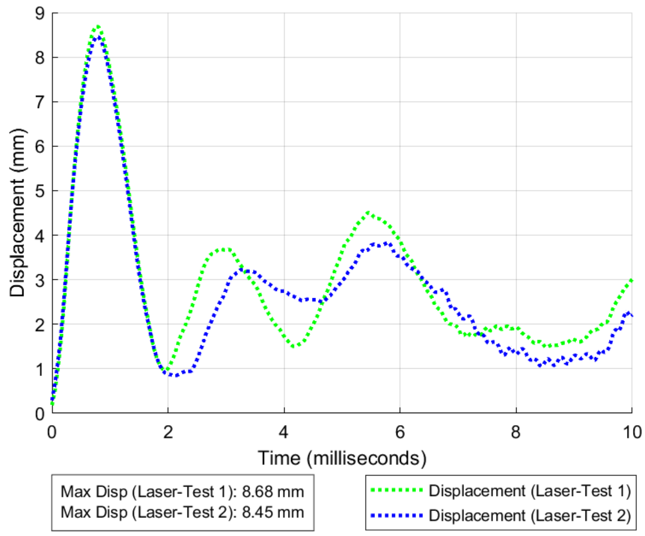

Figure 79: Data from the tests on the 66.4 laminated glass for a 20 g charge

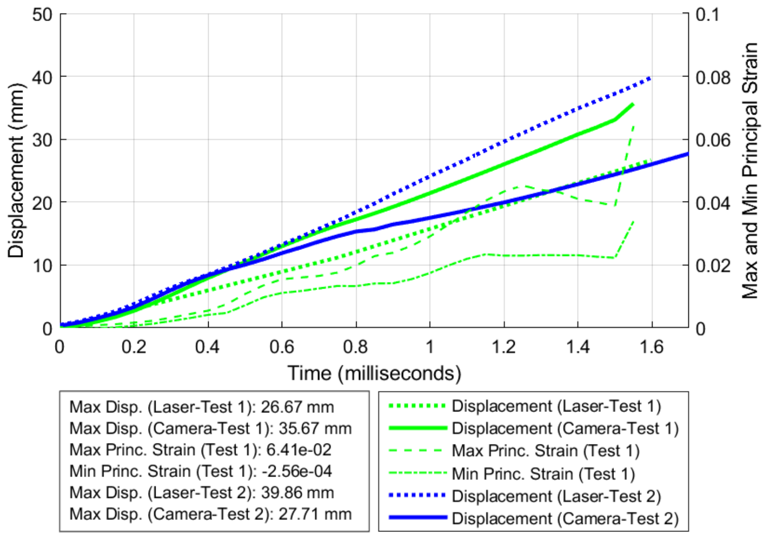

Figure 80: Data from the tests on the 66.4 laminated glass for a 30 g charge

As mentioned earlier, the 66.4 laminated glass only broke under a 30g charge. According to the average data from subchapter 4.2.1, this corresponds to a reflected pressure of 2.26 MPa and a reflected impulse of 1.04 MPa*msec. The damage associated with this charge is visible in the following figures. Most fragments remained attached to the glass, and the fixation system functioned effectively, with no permanent deformation at the points of attachment. This happened in the two tests done with this charge to this glass. However, **Figure 81** and **82** show a different structure holding the glass, with screws located on the side of the shock tube, creating additional difficulty in removing the glass. Then, the rest of the tests were done as described in the subchapter 4.2.1. In the **Figure 83** there is a time-lapse from the second test conducted for this glass and charge, the final results that can be compared to this are in **Figure 84** to **86**.

Figure 81: Laminated glass attached to the strucure after the test

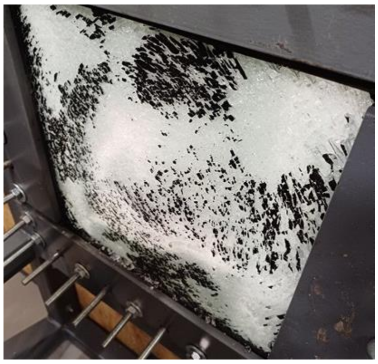

Figure 82: Back of the laminated glass attached to the strucutre after the test

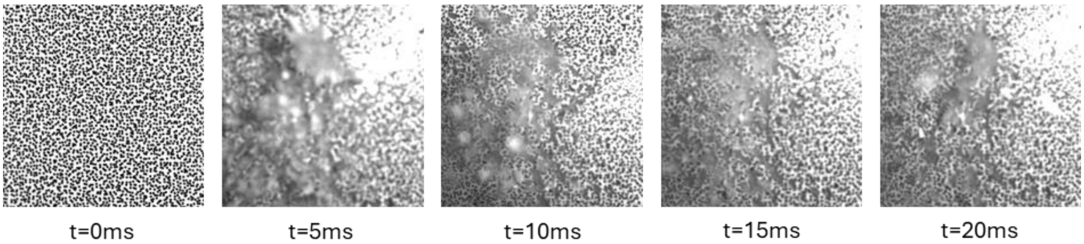

Figure 83: Time-lapse of the destructive test captured over a 5ms interval

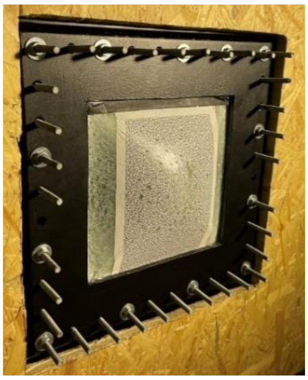

Figure 84: Laminated glass attached to the strucure after the test

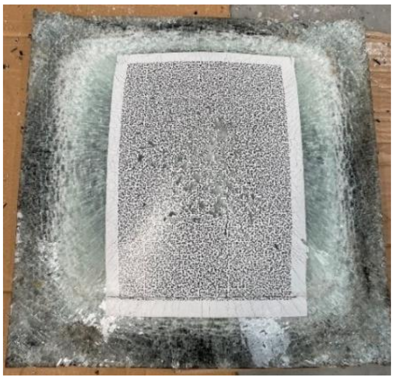

Figure 85: Laminated glass after removal from the structure

Figure 86: Largest fragment observed

To assess the displacement at the centre of the glass, where the maximum displacement is expected, data from the cameras and lasers were carefully analysed. **Table 9** presents a comparison of displacement values obtained from the cameras and lasers.

Table 9: Maximum displacement comparison for 66.4 laminated glass tests

Charge weight (g)	Test	Camera Data (mm)	Laser Data (mm)	Average Test (mm)	Average (mm)
10	Test1	5.260		5.260	4.956
	Test2	4.664	4.637	4.651	
20	Test1		8.681	8.681	8.568
	Test2		8.455	8.455	
30	Test1	Destructive			
	Test2				

4.2.2.2 88.4 Laminated Glass

Figures **87** to **90** show data from all measurement systems and tests, including displacements and strains. In **Figure 90** the glass did not break under a 40g charge, but the camera did not capture the strain and displacement data clearly.

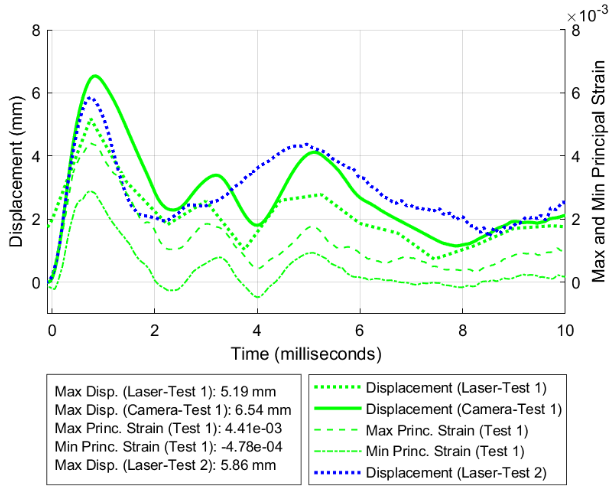

Figure 87: Data from the tests on the 88.4 laminated glass for a 20 g charge

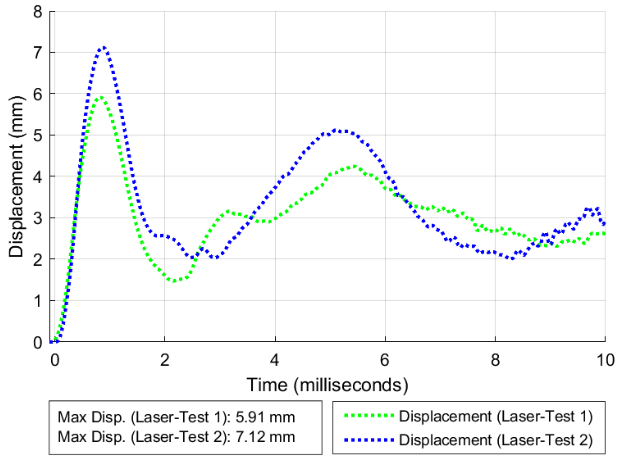

Figure 88: Data from the tests on the 88.4 laminated glass for a 30 g charge

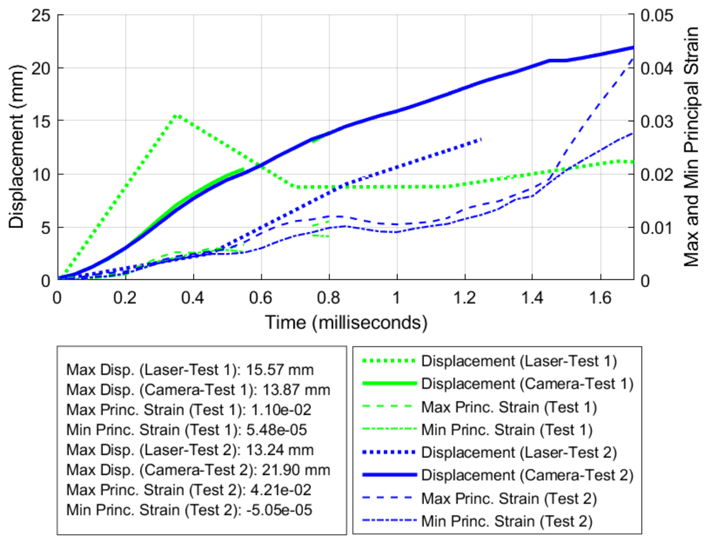

Figure 89: Data from the tests on the 88.4 laminated glass for a 40 g charge

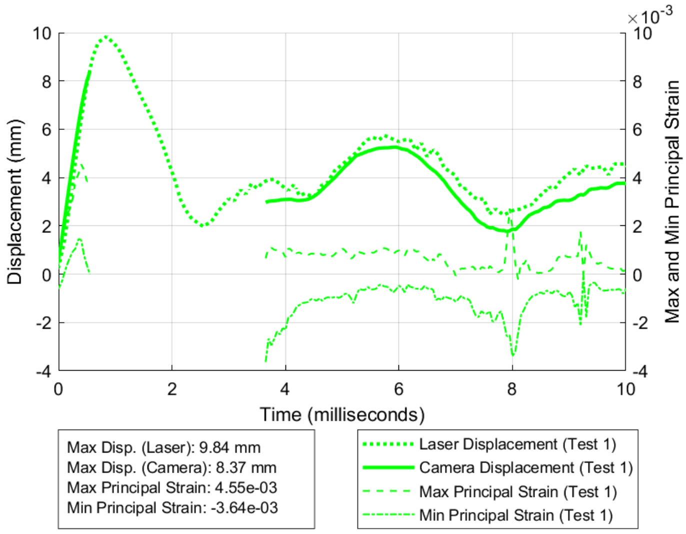

Figure 90: Data from the tests on the 88.4 laminated glass for a 40 g charge where the glass didn't break

As mentioned earlier, the 88.4 laminated glass only broke under a charge of 40g. According to the average data from subchapter 4.1.2, this corresponds to a reflected pressure of 3,12 MPa and a reflected impulse of 1.14 MPa*msec. The damage associated with the first destructive charge is visible in figures **91** to **95**, where most of the outer ply was shattered.

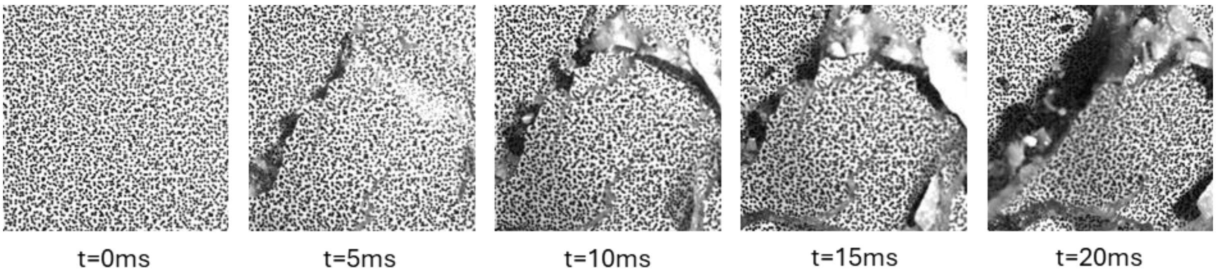

Figure 91: Time-lapse of the destructive test captured over a 5ms interval

Figure 92: Laminated glass attached to the strucure after the test

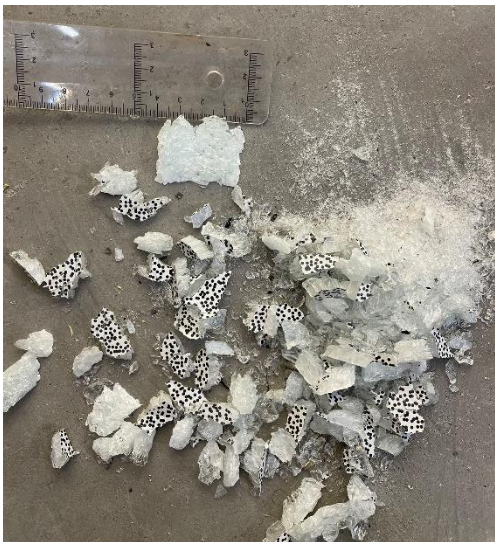

Figure 93: Largest fragment observed

Figure 94: Inner ply completely intact after removal from the structure

Figure 95: Lateral view clearly showing the difference between the shattered outer ply and the intact inner ply, with rubber bands still attached

In the second destructive test, the 40g charge caused a hole through the glass, penetrating both the outer and inner plies as well as the interlayer, in this case the cameras didn't capture the results along the time. The final result can be seen in figures **96** and **97**.

Figure 96: Laminated glass attached to the structure after the test, with a hole going through all layers

Figure 97: Largest fragment observed

In the third destructive test, no damage was observed, so the same glass was subjected to the same destructive charge again. In the fourth test, the outer ply shattered, as shown in figures **98** to **100**.

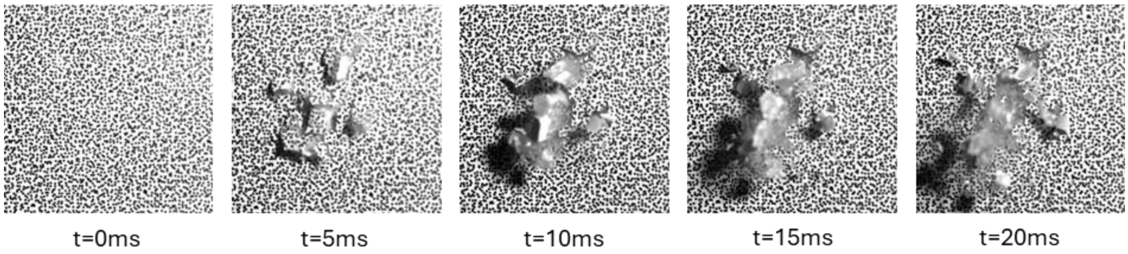

Figure 98: Time-lapse of the destructive test captured over a 5ms interval

Figure 99: Laminated glass attached to the structure after the test, outer ply shattered

Figure 100: Largest fragment observed

To assess the displacement at the centre of the glass, where maximum displacement is expected, data from the cameras and lasers were carefully analysed. **Table 10** compares displacement values obtained from the cameras and lasers results.

Table 10: Maximum displacement comparison for 88.4 laminated glass tests

Charge weight (g)	Test	Camera Data (mm)	Laser Data (mm)	Average Test (mm)	Average (mm)
20	Test1	6.539	5.189	5.864	5.860
	Test2		5.856	5.856	
30	Test1		5.911	5.911	6.516
	Test2		7.121	7.121	
40	Test1	Destructive			
	Test2				
	Test3	8.370	9.843	9.107	9.107
	Test4	Destructive			

4.2.2.3 1010.4 Laminated Glass

Figures **101** to **103** present data from all measurement systems and tests, including displacements and strains.

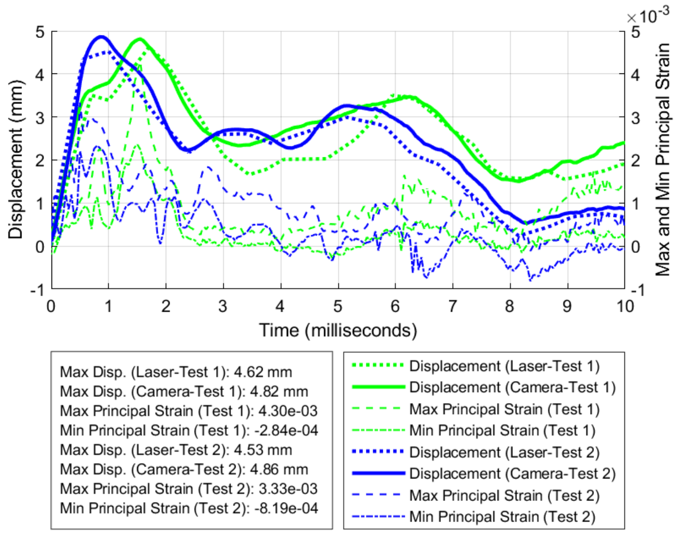

Figure 101: Data from the tests on the 1010.4 laminated glass for a 20 g charge, even thouh one of tests on the glass palnel fracture, it was still possible to capture data

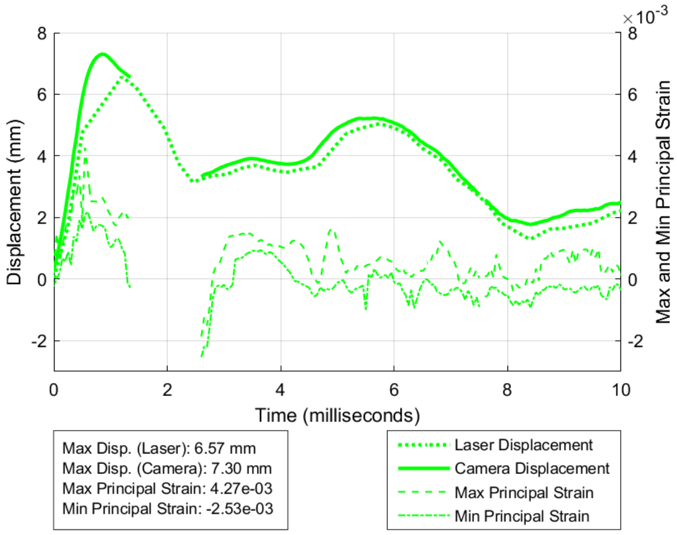

Figure 102: Data from the test on the 1010.4 laminated glass for a 30 g charge

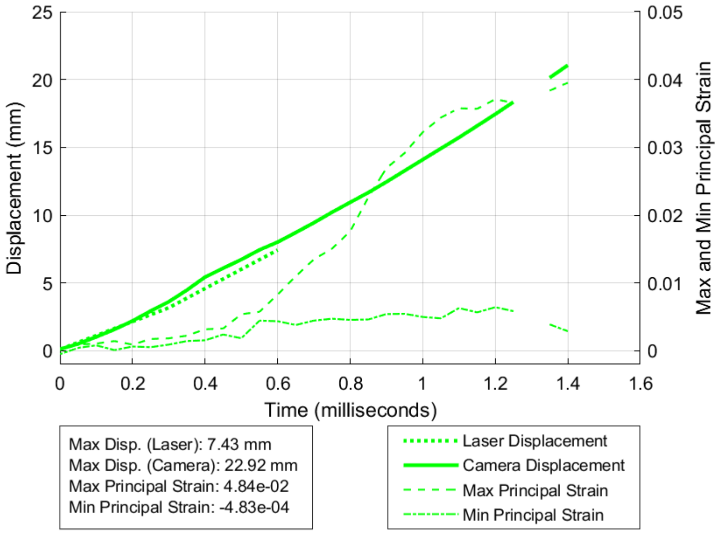

Figure 103: Data from the test on the 1010.4 laminated glass for a 40 g charge

As mentioned earlier, the 1010.4 laminated glass broke under a charge of 20g and 40g. According to the average data from subchapter 4.1.2, this corresponds to a reflected pressure of 3,12 MPa and a reflected impulse of 1.14 MPa*msec.

Figures **104** and **105** show the aftermath of a 20g charge. No fragments were visible, as the inner ply remained completely intact, and the outer ply appeared shattered, but no fragments fell off. As there were no fragments getting off the glass panel, the camera and the laser still capture the maximum displacement of the glass.

Figure 104: Laminated glass attached to the strucure after the test

Figure 105: Laminated glass after removal from the structure

Figures **106** to **108** demonstrate the effects of a 40g charge on the laminated glass, where a hole penetrated through all layers.

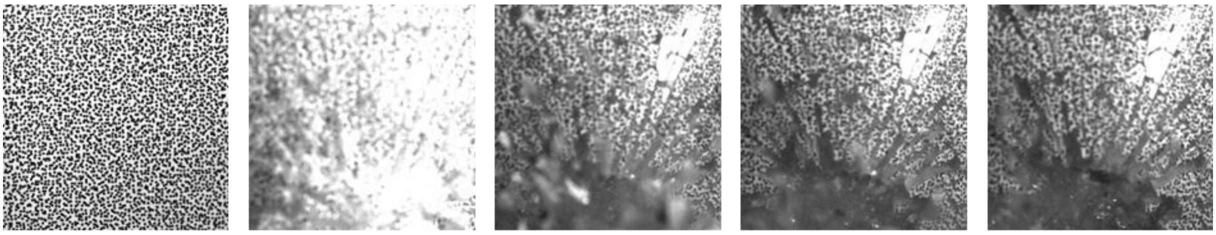

t=0ms t=5ms t=10ms t=15ms t=20ms

Figure 106: Time-lapse of the destructive test captured over a 5ms interval

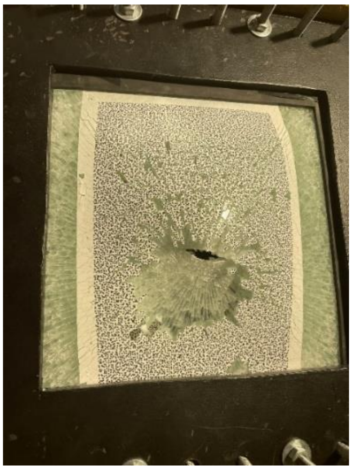

Figure 107: Laminated glass attached to the strucure after the test

Figure 108: Largest fragment observed

To assess the displacement at the centre of the glass, where maximum displacement is expected, data from the cameras and lasers were carefully analysed. **Table 11** compares displacement values obtained from the cameras and lasers results.

Table 11: Maximum displacement comparison for 1010.4 laminated glass tests

Charge weight (g)	Test	Camera Data (mm)	Laser Data (mm)	Average Test (mm)	Average (mm)
20	Test1	4.820	4.619	4.720	4.708
	Test2	4.862	4.527	4.695	
30	Test1	7.304	6.570	6.937	
40	Test1	Destructive			

When compiling the information from the experimental campaign and evaluating the maximum displacement of the glass under specific explosive charges, it is evident that increasing the charge results in greater displacement, as expected. Additionally, increasing the glass thickness reduces the maximum displacement, which is especially noticeable at the 20g charge, as seen in **Figure 109**.

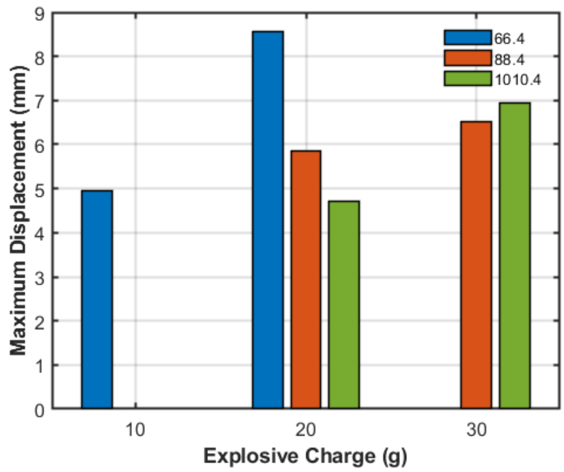

Figure 109: Maximum displacement for each laminated glass type and explosive charge (the 40g charge that resisted for the 88.4 glass was not considered)

5. Results and Discussion

Upon analysing the data obtained from both the experimental campaign and the numerical simulations, the results generally align with the desired objectives. For most tests, the experimental data falls within the range described in Chapter 3, specifically between the simply supported and fully fixed conditions, as shown in **Table 12** . The results are closer to the simply supported boundary condition, indicating that the fixation system used does not completely restrain the movements of the glass panel, allowing some freedom of rotation. This effect is more noticeable for the 66.4 and 88.4 laminated glass. However, for the 1010.4 glass, the locking mechanism seems to be more permissive to displacement. This discrepancy might be due to the limited experimental data available for this thickness, which could introduce some error, unlike the more consistent results observed with the other glasses.

For the 88.4 and 1010.4 laminated glass, the Zhou et al. [67] model was ineffective, requiring a higher strain rate failure criterion for the 30 g charge, resulting in no displacement data. The same issue occurred for the 88.4 laminated glass with the Zhang et al. [66] model under a 30 g charge. In **Table 12**, the Holmquist et al. [65] model closely matched the experimental data, while the fully fixed simple model had the highest average error at 71.76%. Other models showed errors between 15% and 20%, supporting the choice of the simply supported boundary for the final models.

Table 12: Comparison of the maximum displacement between the experimental data and the numerical simulations

Glass	Charge weight (g)	Experimental Data Average (mm)	Fully Fixed - Elastic (Error %)	Simply Supported - Elastic (Error %)	Set up Model (Error %)				
					Elastic	Hidallana et al. [64]	Holmquist et al. [65]	Zhang et al. [66]	Zhou et al. [67]
66.4	**10**	4.834	67.83	15.93	10.05	6.45	5.32	10.76	29.06
	20	8.568	64.64	8.33	11.81	10.14	9.15	14.65	31.99
88.4	**20**	5.860	72.70	10.53	1.98	5.56	6.62	1.60	14.81
	30	6.516	65.88	7.90	20.46	17.59	16.3		
1010.4	**20**	4.715	79.17	28.67	25.19	25.11	25.94	21.76	7.70
	30	6.916	80.35	32.42	27.76	28.53	29.27	25.46	
Average Error per model (%)			**71.76**	**17.30**	**16.21**	**15.56**	**15.43**	**16.15**	**19.59**

In figures **110** to **118** the displacement data from the experimental campaign is compared with the numerical simulation results over time. The figures highlight three key models: the Fully Fixed Elastic model and the Simply Supported Elastic model, which set the upper and lower boundaries for displacement (with the expectation that the experimental data should fall between them), and the Holmquist et al. [65] model, as it represents the best model in terms of displacement in comparison with the experimental data, which best matches the experimental displacement data. Other setup models are included but de-emphasized, as they exhibit similar behaviour over the observed time frame.

The models closely replicate the experimental displacement behaviour during the initial peak, representing maximum displacement. After this peak, results begin to diverge, possibly due to slight plastic deformation in the rubber layers, which may contribute to residual displacement even though the glass itself behaves elastically. To confirm that this residual displacement does not originate from any movement of the structure itself, the structure's position was measured by laser after each test and consistently remained in the same spot. This plasticity could help explain discrepancies in subsequent peaks, as permanent deformation is measured in the tests, which is not possible to obtain in the numerical simulations.

Additionally, there is a difference in oscillatory motion between the numerical models and the experimental data. The numerical models exhibit sustained oscillations, with the Fully Fixed model showing a higher frequency due to its more restrictive boundary conditions. This behaviour contrasts with the experimental data, where the oscillations appear more damped, indicated by a pronounced reduction in amplitude over time.

In destructive tests, numerical simulations showed shorter resistance times than experimental data. This might be because the camera continued recording displacement after the glass fractured, as the initial fracture was obscured by the paper with the stochastic pattern in front of the glass.

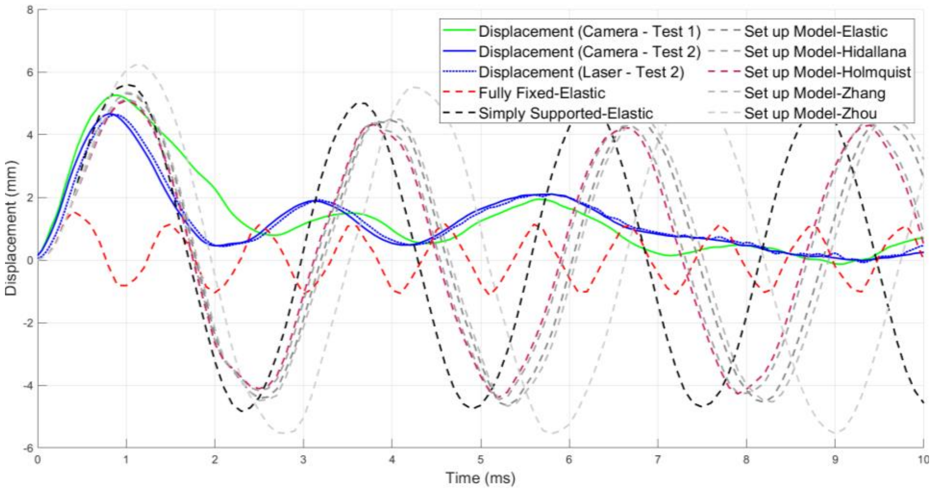

Figure 110: Experimental and numerical displacement analysis of 66.4 laminated glass with a 10g charge

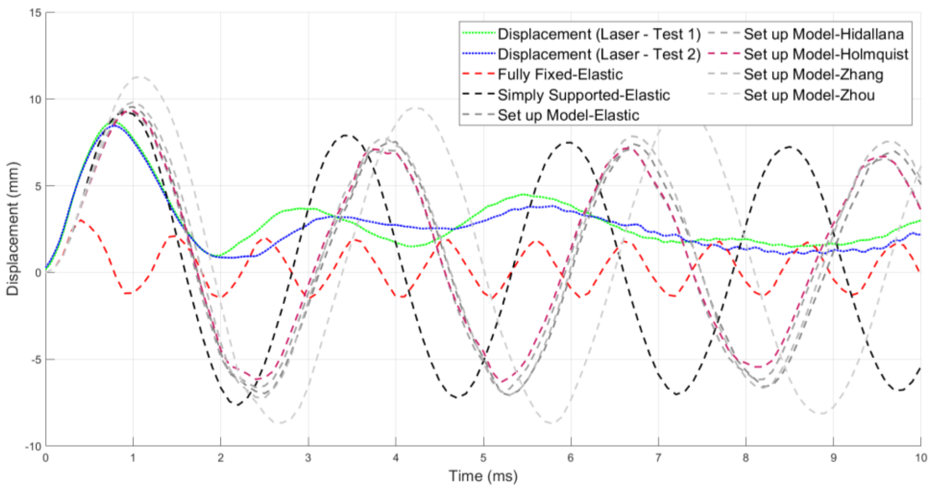

Figure 111: Experimental and numerical displacement analysis of 66.4 laminated glass with a 20g charge

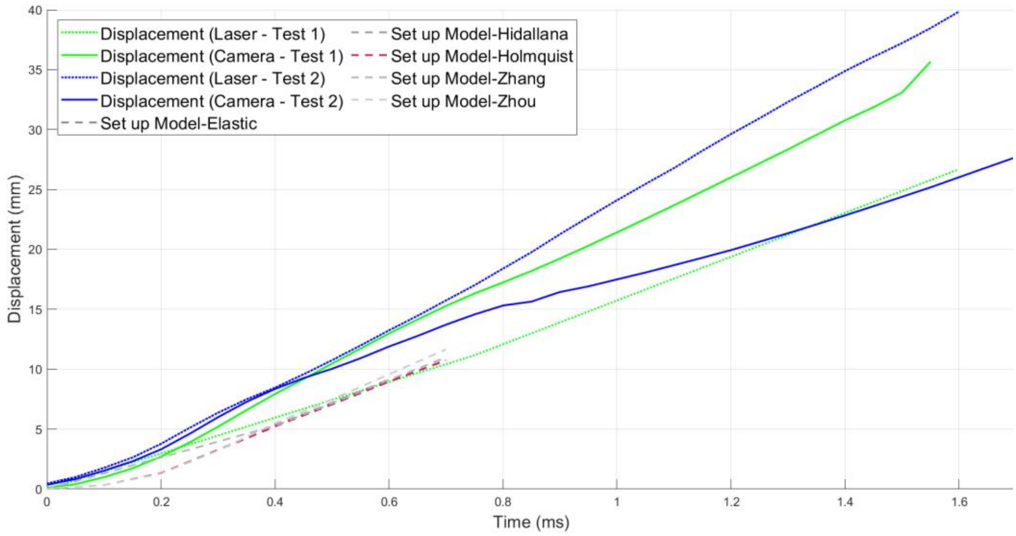

Figure 112: Experimental and numerical displacement analysis of 66.4 laminated glass with a 30g charge

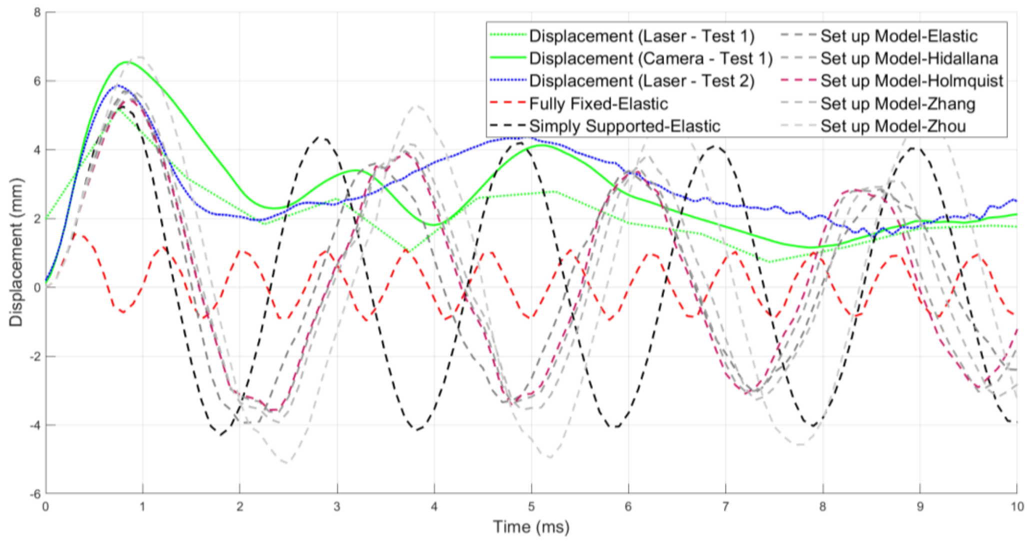

Figure 113: Experimental and numerical displacement analysis of 88.4 laminated glass with a 20g charge

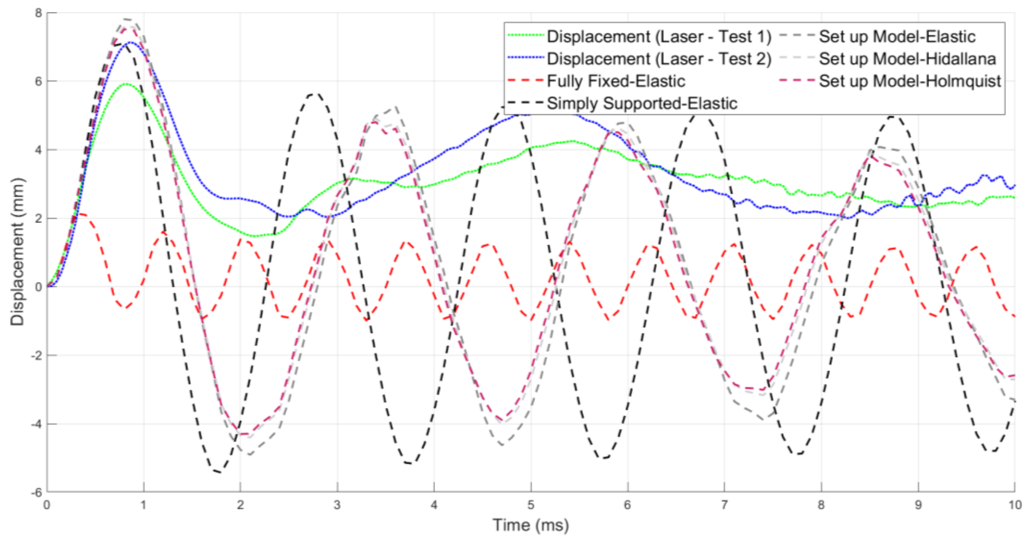

Figure 114: Experimental and numerical displacement analysis of 88.4 laminated glass with a 30g charge

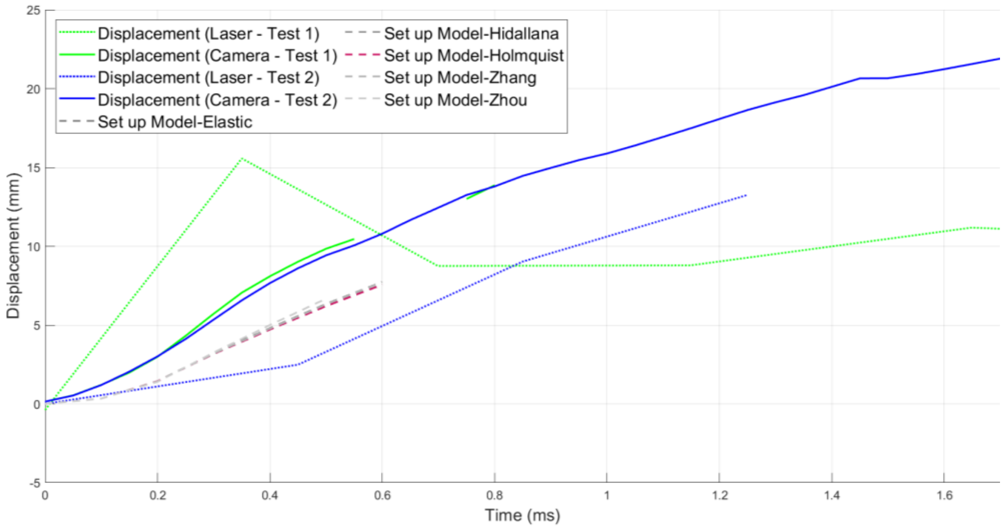

Figure 115: Experimental and numerical displacement analysis of 88.4 laminated glass with a 40g charge

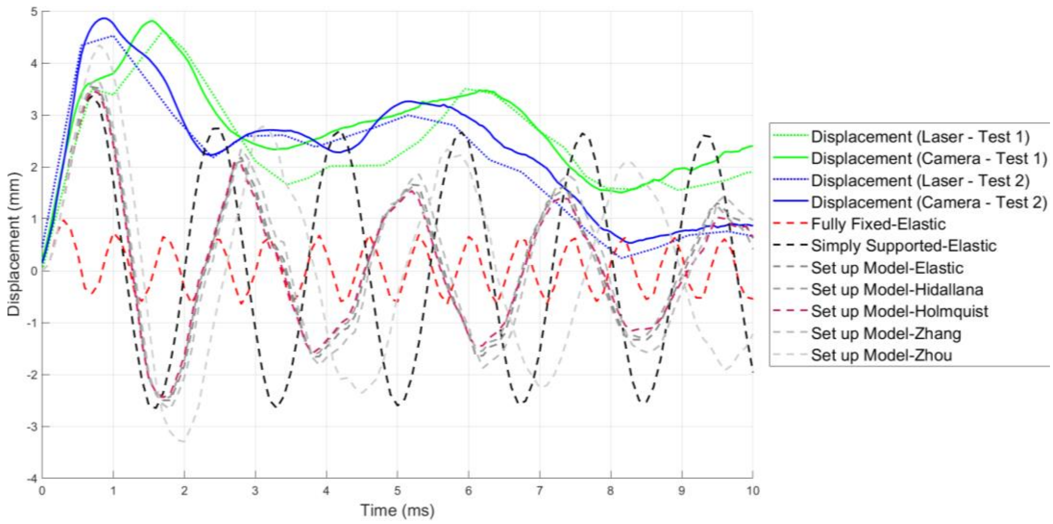

Figure 116: Experimental and numerical displacement analysis of 1010.4 laminated glass with a 20g charge

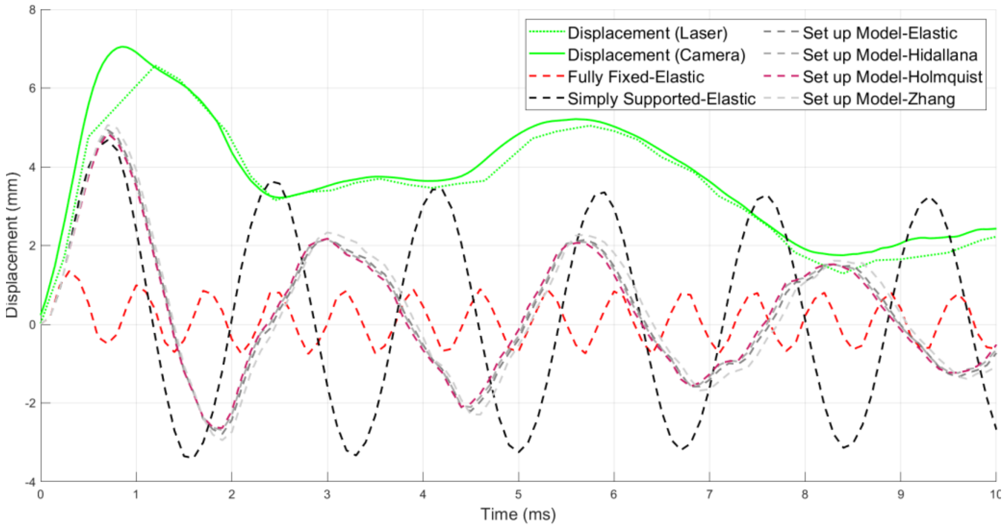

Figure 117: Experimental and numerical displacement analysis of 1010.4 laminated glass with a 30g charge

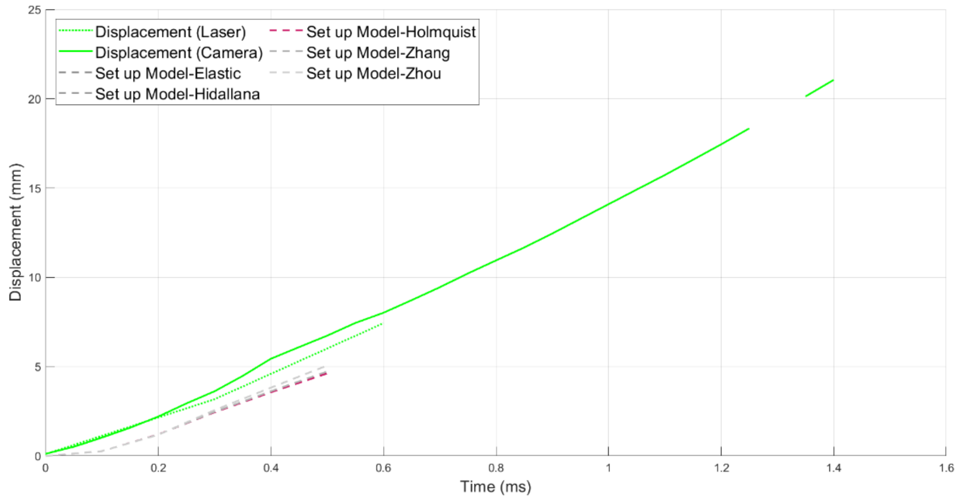

Figure 118: Experimental and numerical displacement analysis of 1010.4 laminated glass with a 40g charge

From the comparison in **Table 13**, the most accurate model in terms of strain prediction is the simple model with a fully fixed boundary. This may be due to the higher strains induced by the fixed boundary, which align more closely with the experimental strain measurements. In general, the strains in the numerical simulations are smaller than those obtained by the cameras in the experimental campaign. For the 66.4 glass with a 20 g charge and 88.4 glass with a charge of 30 g, there is no experimental data available for comparison.

Table 13: Comparison of the maximun principal strain between the experimental data and the numerical simulations

Glass	**Charge weight (g)**	**Experimental Data Average**	**Fully Fixed - Elastic (Error %)**	**Simply Supported - (Error %) Elastic**	**Set up Model (Error %)**				
					Elastic	**Hidallana et al.** [64]	**Holmquist et al.** [65]	**Zhang et al.** [66]	**Zhou et al.** [67]
66.4	**10**	0.00422	38.86	12.56	59.24	61.37	61.85	59.48	51.18
88.4	**20**	0.00441	19.05	28.57	45.12	48.75	48.98	45.80	31.75
1010.4	**20**	0.00382	20.16	26.49	55.76	56.28	56.81	53.93	41.62
	30	0.00427	39.34	58.08	44.03	44.26	43.09	40.52	28.57
Average Error per model (%)			**29.35**	**31.43**	**51.04**	**52.67**	**52.68**	**49.93**	**38.28**

The minimum principal strain shows the greatest difference between the experimental campaign and the numerical simulations, as seen in **Table 14**. This discrepancy is likely due to limitations in the experimental strain measurement process, as the cameras used might not accurately record negative strain values (compression), leading to variations when compared to the numerical simulations. The absolute error for the minimum principal strain is significantly higher, with values ranging from approximately 201% to 477%. This indicates a substantial discrepancy between the experimental and numerical results for compressive strains, suggesting that the models may need further refinement in capturing compressive behaviour or that the experimental measurement systems may have limitations. For the 66.4 glass with a 20 g charge and 88.4 glass with a charge of 30 g, there is no experimental data available for comparison.

Table 14: Comparison of the minimun principal strain between the experimental data and the numerical simulations

Glass	Charge weight (g)	Experimental Data Average	Fully Fixed - Elastic (Error %)	Simply Supported - Elastic (Error %)	Set up Model (Error %)				
					Hidallana et al. [64]	**Holmquist et al.** [65]	**Zhang et al.** [66]	**Zhou et al.** [67]	**Hidallana et al.** [64]
66.4	**10**	-0.00166	45.78	129.52	3.61	1.20	2.41	(5.42	33.73
88.4	**20**	-0.00048	608.33	979.17	481.25	408.33	427.08	529.17	814.58
1010.4	**20**	-0.00055	438.18	729.09	383.64	372.73	367.27	418.18	572.73
	30	-0.00364	30.77	70.33	22.53	23.08	20.60	19.78	8.52
Average Error per model (%)			**280.77**	**477.03**	**222.76**	**201.34**	**204.34**	**243.14**	**357.39**

As noted in Subchapter 4.2.2, the PVB only ruptured in some tests for 88.4 and 1010.4 glass, and not consistently. This could have happened due to a variety of reasons, such as the handling of the glass before the experimental campaign, the pressure applied to the locking system, or even the placement of the charge at the entrance of the shock tube (as explained before, the placement of the charge was centred and weighted but could vary slightly due to the volatility of the explosive).

The model that most closely reproduced the 66.4 laminated glass destructive test (30 g charge) was the Hidallana et al. [64] model, as seen in **Figure 38**. The damage patterns resembled those observed in the experimental campaign, with the damage on the ply nearest to the shock tube resembling the pattern in **Figure 82**, and the centred damage on the outer ply resembling the pattern in **Figure 81**.

For the 88.4 and 1010.4 laminated glass destructive tests (40g charge), no similar models accurately captured the damage, as the damage patterns for those tests was very dispersed.

Analysing the destructive tests from the experimental campaign in Subchapter 4.2.2 and the numerical results in Subchapter 3.5, it can be noted that the damage initiates from the centre and propagates towards the edges, with more damage concentrated at the centre. Notably, the rubber locking mechanism did not cause additional damage, which can be seen in almost all the models and is confirmed in **Figure 85** of the experimental campaign. Furthermore, there was significantly less fracture in the glass layer closest to the shock tube. This was one of the details that most supported the models, since in the experimental campaign, in most of the tests, the glass layer closest to the shock tube did not suffer significant damage. This behaviour was successfully replicated in the numerical simulations, indicating that the models are accurately capturing the essential aspects of the glass panel's response to blast loads.

Overall, the combination of experimental data and numerical simulations provides a comprehensive understanding of the behaviour of laminated glass under blast loading. The numerical models, particularly those using the Holmquist et al. [65] model with a simply supported boundary condition, show good agreement with experimental results in terms of displacement and strain patterns. While there are discrepancies in strain magnitudes, especially for minimum principal strains, the general trends and failure modes are well represented.

To further improve the study, a pressure-impulse diagram was created based on the Holmquist et al. [65] model, as it more closely resembled the experimental campaign. For this purpose, it was chosen not to use the Friedlander equation (2.6) but instead employed a simple triangular load, as mentioned in equation (2.8) for the blast load. This approach was adopted because it allowed for faster testing of multiple combinations, which also explains why the response given by the numerical simulations is not exactly equal to the previous analysis. The damage level considered was the first level, as explained in subchapter 2.3.7, meaning that failure was defined as the point when the glass first cracks. Tests were performed to multiple combinations of pressure and impulse and them the result of the criteria applied fitted to Friedlander equation (2.6) by non-linear least squares fit and the parameters obtained exposed in **Table 15**.

Based on this assessment and in the graph in the **Figure 119**, the 88.4 laminated glass was expected to be at the boundary of failure at a 30g charge, which would justify the tests showing fracture at that charge. However, the experimental results showed that the 88.4 glass did not fracture at 30g, but instead only broke at 40g. The difference could stem from several factors, such as the simplified triangular load applied in the simulations. Additionally, slight variations in the material properties or experimental setup (such as boundary conditions or glass positioning) could influence the actual fracture behaviour, resulting in the glass withstanding a higher charge than predicted.

The variables for the iso-damage curves are presented in **Table 15**, and the curves are shown in **Figure 119**. These curves provide an important reference for predicting glass failure under blast loads but must be interpreted with caution, as real-world behaviour can vary due to the complexities of blast interactions with laminated glass.

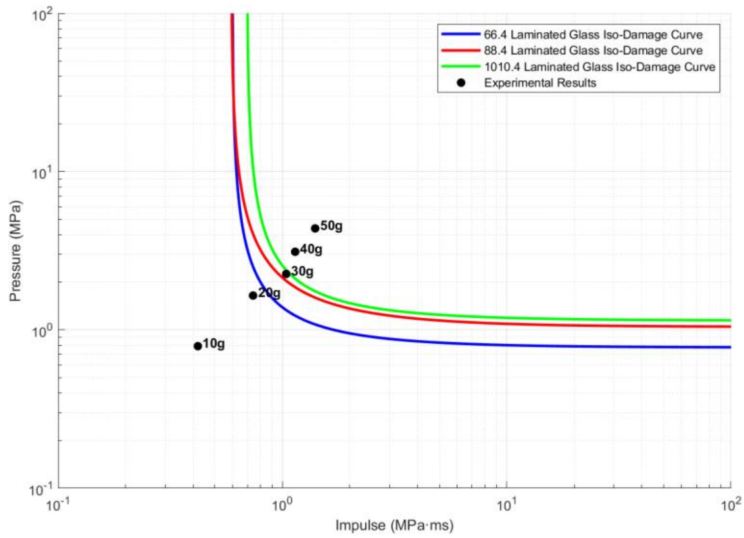

Figure 119: Iso-damage curves with a logarithmic scale

Table 15: Variables for the iso-damage curves

Glass	P_{cr} (MPa)	I_{cr} (MPa*msec)	α	β
66.4	0.849	0.608	9.066	12.200
88.4	1.045	0.590	0.508	0.601
1010.4	1.148	0.695	1.202	12.529

6. Conclusion and Future Work

This study aimed to analyse the behaviour of laminated glass panels under blast loading through both experimental campaigns and numerical simulations. Experimental results showed that the panels' response lay between the simply supported and fully fixed boundary conditions, tending towards the simply supported, suggesting the fixation system allows some rotational freedom.

The numerical simulations, especially those utilizing the Holmquist et al. [65], Hidallana et al. [64] and Zhang et al. [14] models with a simply supported boundary condition, showed good agreement with the experimental data in terms of displacement. However, divergencies were observed in the strain magnitudes, particularly for the minimum principal strains.

The Hidallana et al. [64] model satisfactorily replicated observed damage patterns, such as fractures initiating at the centre and propagating towards the edges, and the minimal damage to the glass layer closest to the shock tube for the 66.4 laminated glass. This validated the effectiveness of the model in capturing some aspects of laminated glass behaviour under blast loading for this type of glass. However, no definitive conclusion could be made regarding the 88.4 and 1010.4 laminated glass, as the experimental results for these glass types were more diverse.

Future work should focus on improving the understanding of the behaviour of glass post-rupture. Developing more sophisticated material models that accurately capture the fracture and post-fracture behaviour of glass would enhance the predictive capability of numerical simulations. Additionally, new structures for holding the glass should be explored, as the mechanism that supports the glass is a key variable affecting the results. For example, a suspended glass structure, where the glass is held by ropes, could improve the study by reducing the number of variables and allowing a clearer focus on the glass behaviour itself.

Moreover, if the goal is to study the evolution of crack patterns in the glass, it may not be feasible to use stochastic paper in front of the glass or dark paint on the ply that receives the shockwave, as these elements hinder the visibility of crack progression. Implementing high-speed imaging techniques without obstructions would enable better observation of crack initiation and growth.

A separate study for the PVB interlayer is also recommended, since the interlayer plays a significant role in the behaviour of laminated glass. One way to mitigate uncertainties related to its behaviour is to perform strain rate tests on the PVB material before it is applied in laminated glass. This would provide a better understanding of its mechanical properties under dynamic loading conditions and improve the accuracy of the simulations.

In conclusion, advancing the understanding of laminated glass behaviour under blast loading requires an approach that incorporates material characterization, experimental campaigns, and refined numerical modelling. Addressing these challenges will enhance the performance assessment of glass structures subjected to blast loads.

References

[1] M. Kozłowski, A. Malewski, V. Akmadžić, and A. Vrdoljak, 'Glass in Structural Applications', *Electron. Collect. Pap. Fac. Civ. Eng.*, pp. 47–55, Dec. 2019.

[2] G. C. Team, 'Iconic construction projects: The Shard', Go Construct. Accessed: Sep. 04, 2024. [Online]. Available: https://www.goconstruct.org/why-choose-construction/whats-happening-in-construction/iconic-construction-projects-the-shard/

[3] 'Louvre Pyramid | History, Description, & Facts | Britannica'. Accessed: Sep. 04, 2024. [Online]. Available: https://www.britannica.com/topic/Louvre-Pyramid

[4] P. A. Hooper, R. A. M. Sukhram, B. R. K. Blackman, and J. P. Dear, 'On the blast resistance of laminated glass', *Int. J. Solids Struct.*, vol. 49, no. 6, pp. 899–918, Mar. 2012, doi: 10.1016/j.ijsolstr.2011.12.008.

[5] D. Cormie, G. Mays, and P. Smith, *Blast Effects on Buildings*, 3rd ed. London: Institution of Civil Engineers, 2019.

[6] D. C. Smith, 'The Role of the Engineer Before and After Terrorist Bombings -The UK Experience', Security Facilities Executive,Special Services Group,St. Christopher House, Southwark Street, London, England, Aug. 1996.

[7] M. Larcher, G. Solomos, F. Casadei, and N. Gebbeken, 'Experimental and numerical investigations of laminated glass subjected to blast loading', *Int. J. Impact Eng.*, vol. 39, no. 1, pp. 42–50, Jan. 2012, doi: 10.1016/j.ijimpeng.2011.09.006.

[8] J. Pelfrene, J. Kuntsche, S. Van Dam, W. Van Paepegem, and J. Schneider, 'Critical assessment of the post-breakage performance of blast loaded laminated glazing: Experiments and simulations', *Int. J. Impact Eng.*, vol. 88, pp. 61–71, Feb. 2016, doi: 10.1016/j.ijimpeng.2015.09.008.

[9] ANSYS, 'LS-DYNA Keyword and Theory Manuals'. Livermore software technology, Sep. 28, 2021. [Online]. Available: www.lstc.com

[10] X. Zhang and H. Hao, 'Experimental and numerical study of boundary and anchorage effect on laminated glass windows under blast loading', *Eng. Struct.*, vol. 90, pp. 96–116, May 2015, doi: 10.1016/j.engstruct.2015.02.022.

[11] P. Kumar and A. Shukla, 'Dynamic response of glass panels subjected to shock loading', *J. Non-Cryst. Solids*, vol. 357, no. 24, pp. 3917–3923, Dec. 2011, doi: 10.1016/j.jnoncrysol.2011.08.009.

[12] S. Chen, X. Chen, G.-Q. Li, and Y. Lu, 'A theoretical study on the P-I diagram of framed monolithic glass window subjected to blast loading', *Eng. Struct.*, vol. 150, pp. 497–510, Nov. 2017, doi: 10.1016/j.engstruct.2017.07.055.

[13] X. Zhang, H. Hao, and Z. Wang, 'Experimental Investigation on Monolithic Tempered Glass Window Responses to Blast Loads', *Int. J. Prot. Struct.*, vol. 6, no. 2, pp. 287–309, Jun. 2015, doi: 10.1260/2041-4196.6.2.287.

[14] X. Zhang, H. Hao, and G. Ma, ‘Parametric study of laminated glass window response to blast loads’, *Eng. Struct.*, vol. 56, pp. 1707–1717, Nov. 2013, doi: 10.1016/j.engstruct.2013.08.007.

[15] S. Chen, X. Chen, G.-Q. Li, and Y. Lu, ‘Development of Pressure-Impulse Diagrams for Framed PVB-Laminated Glass Windows’, *J. Struct. Eng.*, vol. 145, no. 3, p. 04018263, Mar. 2019, doi: 10.1061/(ASCE)ST.1943-541X.0002258.

[16] S. P. Timošenko and S. Woinowsky-Krieger, *Theory of plates and shells*, 2nd ed. in Engineering societies monographs. Auckland Hamburg: McGraw-Hill, 20.

[17] M. Hejazi and A. Sari, ‘Numerical and experimental assessment of optimal modeling of laminated glass post-breakage response’, *Compos. Struct.*, vol. 330, p. 117822, Feb. 2024, doi: 10.1016/j.compstruct.2023.117822.

[18] P. Hála, P. Konrád, and P. Kheml, ‘Experimental analysis of freely-hanging laminated glass subjected to blast’, *Mater. Today Proc.*, vol. 93, pp. 658–661, 2023, doi: 10.1016/j.matpr.2023.04.594.

[19] M. J. Meyland and J. H. Nielsen, ‘Ongoing Research into the Failure of Glass at High Strain-Rates’, *Challenging Glass Conf. Proc.*, vol. 7, Sep. 2020, doi: 10.7480/cgc.7.4428.

[20] M. Patterson, *Structural Glass Facades and Enclosures*. Wiley, 2011. [Online]. Available: https://books.google.cz/books?id=qsqi2jdH7ecC

[21] M. Haldimann, A. Luible, and M. Overend, *Structural use of glass*. in Structural engineering documents, no. 10. Zürich: Association for Bridge and Structural Engineering, 2008.

[22] C. Morison, ‘The resistance of laminated glass to blast pressure loading and the coefficients for single degree of freedom analysis of laminated glass’, Cranfield university, Defence college of management and technology, 2010. [Online]. Available: https://books.google.cz/books?id=kVNU0AEACAAJ

[23] J. Wurm, *Glass structures: design and construction of self-supporting skins*. in Design and construction of self-supporting skins. Basel: Birkhäuser, 2007.

[24] W. Laufs and A. Luible, ‘Introduction on use of glass in modern buildings’, École Polytechnique Fédérale de Lausanne, Lausanne, 462, Apr. 2003. [Online]. Available: https://www.researchgate.net/publication/37455557

[25] C. O’Regan, *Structural use of glass in buildings*, 2nd ed. in The Institution of Structural Engineers. London: Institution of Structural Engineers, 2015.

[26] U.S. Army Material Command, *Engineering design handbook: Explosions in air, part one*. Alexandria, Virinia: U.S. Army Material Command Headquarters, 1974. [Online]. Available: https://books.google.cz/books?id=eXv3zwEACAAJ

[27] Y. Suzuki *et al.*, ‘Propagation of Avalanches in Mn 12 -Acetate: Magnetic Deflagration’, *Phys. Rev. Lett.*, vol. 95, no. 14, p. 147201, Sep. 2005, doi: 10.1103/PhysRevLett.95.147201.

[28] F. S. Baker and G. J. Privett, ‘Dynamic mechanical studies of nitrocellulose/nitroglycerine mixtures’, *Polymer*, vol. 28, no. 7, pp. 1121–1126, Jun. 1987, doi: 10.1016/0032-3861(87)90253-9.

[29] R. W. King, *Safety in the process industries*. Elsevier Scientific Pub. Co, 1990. [Online]. Available: https://www.sciencedirect.com/book/9780750610193/safety-in-the-process-industries

[30] S. Kundu, J. Zanganeh, and B. Moghtaderi, ‘A review on understanding explosions from methane–air mixture’, *J. Loss Prev. Process Ind.*, vol. 40, pp. 507–523, Mar. 2016, doi: 10.1016/j.jlp.2016.02.004.

[31] W. E. Baker, P. A. Cox, P. S. Westine, J. J. Kulesz, and R. A. Strehlow, *Explosion Hazards and Evaluation*, vol. 5, 16 vols. in Fundamental studies in engineering, no. 0 444 41756 7, vol. 5. Amsterdam: Elsevier Scientific Pub. Co, 1983.

[32] S. A. Formby and R. K. Wharton, ‘Blast characteristics and TNT equivalence values for some commercial explosives detonated at ground level’, *J. Hazard. Mater.*, vol. 50, no. 2–3, pp. 183–198, Oct. 1996, doi: 10.1016/0304-3894(96)01791-8.

[33] U. N. SaferGuard, ‘International Ammunition Technical Guideline (IATG)’, *Formulae Ammunit. Manag. UN 18p*, 2015.

[34] D. J. B. Rodrigues, ‘Demolição de edifícios de betão armado por métodos explosivos. O caso de estudo do edifício C5 do Hospital das Forças Armadas.’, Instituto Superior Técnico; Academia Militar.

[35] U.S. Army corps of engineers, Naval facilities engineering command, and Air force civil engineer support agency, *Unified Facilities Criteria (UFC) Structures to Resist the Effects of Accidental Explosions*. 2008.

[36] H. Draganić and V. Sigmund, ‘Blast Loading on Structures’, 2012, [Online]. Available: https://www.humanitarianlibrary.org/sites/default/files/2018/10/tv_19_2012_3_643_652.pdf

[37] E. Yandzio and M. Gough, *Protection of Buildings against Explosions*. Berkshire: The Steel Construction Institute, 2011. [Online]. Available: http://ndl.ethernet.edu.et/bitstream/123456789/9095/1/68.pdf

[38] G. F. Kinney and K. J. Graham, *Explosive Shocks in Air*, 2nd ed. Berlin: Springer Berlin Heidelberg, 1985. doi: 10.1007/978-3-642-86682-1.

[39] P. D. Smith and J. G. Hetherington, *Blast and ballistic loading of structures*. New York: Butterworth-Heinemann, 1994.

[40] Task Committee on Blast-Resistant Design of the Petrochemical Committee of the Energy Division of the ASCE, *Design of Blast-Resistant Buildings in Petrochemical Facilities*, 2nd ed. Reston, VA: American Society of Civil Engineers, 2010. doi: 10.1061/9780784410882.

[41] C. E. Needham, ‘The Rankine–Hugoniot Relations’, in *Blast Waves*, Berlin: Springer Berlin Heidelberg, 2010, pp. 9–15. doi: 10.1007/978-3-642-05288-0_3.

[42] A. T. Toy and B. Sevim, ‘Numerically and empirically determination of blasting response of a RC retaining wall under TNT explosive’, *Adv. Concr. Constr.*, vol. 5, no. 5, pp. 493–512, Oct. 2017, doi: 10.12989/ACC.2017.5.5.493.

[43] H. L. Brode, ‘Numerical Solutions of Spherical Blast Waves’, *J. Appl. Phys.*, vol. 26, no. 6, pp. 766–775, Jun. 1955, doi: 10.1063/1.1722085.

[44] J. Henrych, *The dynamics of explosion and its use*. in Developments in Civil Engineering, no. 1. Czechoslovak Academy of Sciences: Elsevier Scientific Pub. Co.

[45] C. N. Kingery, G. Bulmash, and U.S. Army Ballistic Research Laboratory, *Air blast parameters from TNT spherical air burst and hemispherical surface burst*. Aberdeen Proving Ground, MD: Ballistic Research Laboratories Aberdeen Proving Ground, MD, 1984.

[46] J. Shin, A. S. Whittaker, A. J. Aref, and D. Cormie, *Air-Blast Effects on Civil Structures*. New York: MCEER, 2014.

[47] D. Jeon, K. Kim, and S. Han, 'Modified Equation of Shock Wave Parameters', *Computation*, vol. 5, no. 3, Art. no. 3, Sep. 2017, doi: 10.3390/computation5030041.

[48] A. C. Courtney, L. P. Andrusiv, and M. W. Courtney, 'Oxy-acetylene driven laboratory scale shock tubes for studying blast wave effects', *Rev. Sci. Instrum.*, vol. 83, no. 4, p. 045111, Apr. 2012, doi: 10.1063/1.3702803.

[49] H. Ousji *et al.*, 'Parametric Study of an Explosive-Driven Shock Tube as Blast Loading Tool', *Exp. Tech.*, vol. 40, no. 4, pp. 1307–1325, Aug. 2016, doi: 10.1007/s40799-016-0128-3.

[50] Y. Wang *et al.*, 'Tightly Coupled Repetitive Blast-Induced Traumatic Brain Injury: Development and Characterization in Mice', *J. Neurotrauma*, vol. 28, no. 10, pp. 2171–2183, Oct. 2011, doi: 10.1089/neu.2011.1990.

[51] M. D. Alley, B. R. Schimizze, and S. F. Son, 'Experimental modeling of explosive blast-related traumatic brain injuries', *NeuroImage*, vol. 54, pp. S45–S54, Jan. 2011, doi: 10.1016/j.neuroimage.2010.05.030.

[52] J. Liu, Q. Yan, and J. Wu, 'Analysis of blast wave propagation inside tunnel', vol. 14, no. 5, pp. 358–362, Oct. 2008, doi: 10.1007/s12209-008-0061-3.

[53] V. Karlos and G. Solomos, 'Calculation of blast loads for application to structural components.', Joint Research Centre, European Comission, Italy, Technical Report 32253–2011, 2013. Accessed: Jun. 25, 2024. [Online]. Available: https://core.ac.uk/download/pdf/38628317.pdf

[54] General Service Administration, 'Standard test method for glazing and window systems subject to dynamic overpressure loadings', GSA, Washington,DC, 2003.

[55] Y. Shi, H. Hao, and Z.-X. Li, 'Numerical derivation of pressure–impulse diagrams for prediction of RC column damage to blast loads', *Int. J. Impact Eng.*, vol. 35, no. 11, pp. 1213–1227, Nov. 2008, doi: 10.1016/j.ijimpeng.2007.09.001.

[56] A. Harish, 'What is Convergence in Finite Element Analysis?', SimScale. Accessed: Jul. 11, 2024. [Online]. Available: https://www.simscale.com/blog/convergence-finite-element-analysis/

[57] M. Okereke and S. Keates, *Finite Element Applications*. in Springer Tracts in Mechanical Engineering. Cham: Springer International Publishing, 2018. doi: 10.1007/978-3-319-67125-3.

[58] M. Teotia and R. K. Soni, 'Applications of finite element modelling in failure analysis of laminated glass composites: A review', *Eng. Fail. Anal.*, vol. 94, pp. 412–437, 2018, doi: https://doi.org/10.1016/j.engfailanal.2018.08.016.

[59] 'LS-PREPOST', DYNAmore GmbH. Accessed: Jul. 11, 2024. [Online]. Available: https://www.dynamore.de/en/products/pre-and-postprocessors/prepost

[60] T. P. Slavik, ‘A coupling of empirical explosive blast loads to ALE air domains in LS-DYNA®’, *IOP Conf. Ser. Mater. Sci. Eng.*, vol. 10, p. 012146, Jun. 2010, doi: 10.1088/1757-899X/10/1/012146.

[61] G. Dhatt, G. Touzot, E. Lefrançois, and G. Dhatt, *Finite element method*. in Numerical methods series. London: ISTE Ltd, 2012.

[62] A. Haufe, K. Schweizerhof, and P. Dubois, ‘Properties & Limits: Review of Shell Element Formulations’, Sep. 24, 2013. doi: 10.13140/RG.2.2.28097.35688.

[63] G. R. Johnson and T. J. Holmquist, ‘An improved computational constitutive model for brittle materials’, in *AIP Conference Proceedings*, Colorado Springs, Colorado (USA): AIP, 1994, pp. 981–984. doi: 10.1063/1.46199.

[64] T. J. Holmquist, G. R. Johnson, C. M. Lopatin, D. E. Grady, and J. Hertel, ‘High strain rate properties and constitutive modeling of glass’, Sandia National Lab. (SNL-NM), Albuquerque, NM (United States), SAND-95-0379C; CONF-950537-2, Mar. 1995. doi: 10.2172/41367.

[65] H. D. Hidallana-Gamage, D. P. Thambiratnam, and N. J. Perera, ‘Numerical modelling and analysis of the blast performance of laminated glass panels and the influence of material parameters’, *Eng. Fail. Anal.*, vol. 45, pp. 65–84, Oct. 2014, doi: 10.1016/j.engfailanal.2014.06.013.

[66] X. Zhang, H. Hao, and G. Ma, ‘Dynamic material model of annealed soda-lime glass’, *Int. J. Impact Eng.*, vol. 77, pp. 108–119, Mar. 2015, doi: 10.1016/j.ijimpeng.2014.11.016.

[67] X.-Q. Zhou, M.-Y. Wang, and L.-X. Li, ‘Dynamic damage assessment of float glass under blast loading’, *Adv. Struct. Eng.*, vol. 22, no. 11, pp. 2517–2529, Aug. 2019, doi: 10.1177/1369433219845691.

[68] G. R. Johnson and W. H. Cook, ‘Fracture characteristics of three metals subjected to various strains, strain rates, temperatures and pressures’, *Eng. Fract. Mech.*, vol. 21, no. 1, pp. 31–48, Jan. 1985, doi: 10.1016/0013-7944(85)90052-9.

[69] Exército Português, ‘Ficha de Material. Explosivo Plástico Tipo PE-4A’, Portugal.

[70] Exército Português, ‘Ficha de Material. Detonador elétrico N.º8 instantâneo’, Portugal.

[71] Kern, ‘Operating manual Precision balances’, KERN & Sohn GmbH, Balingen, Jun. 2019. [Online]. Available: https://www.kern-sohn.com/manuals/files/English/PLJ_N-BA-e-0930.pdf

[72] PCB Piezotronics, ‘Model 113B22 ICP Pressure Sensor Installation and Operating Manual’, Mar. 2013.

[73] PCB Piezotronics, ‘Model 113B24 ICP Pressure Sensor Installation and Operating Manual’, Jun. 2024.

[74] PCB Piezotronics, ‘Model 482C15 - Installation and Operating Manual’, 38410, Oct. 2019.

[75] Chemring Technology Solutions, ‘Breach MC - Lightweight Multi-Circuit RF Firing System’. 2021. Accessed: Aug. 06, 2024. [Online]. Available: https://cdn.shopify.com/s/files/1/0405/0881/7558/files/Breach_MC_Datasheet_V1_4.pdf?v=1637597450

[76] National Instruments, ‘Device specifications - NI 6361’, Sep. 2015.

[77] Photron, ‘Mini AX FastCam’, Feb. 2017.

[78] ‘Photron Fastcam Mini AX50 and AX100’. Accessed: Aug. 07, 2024. [Online]. Available: https://www.mengelengineering.dk/photron-fastcam-mini-ax50-and-ax100.html

[79] ‘A Empresa’, Vidreira Algarvia. Accessed: Aug. 22, 2024. [Online]. Available: https://vidreira-algarvia.pt/empresa/

[80] SAINT-GOBAIN GLASS, *Manual do Vidro*. Santa Iria de Azóia, 2008. [Online]. Available: www.saint-gobain-glass.com

[81] ‘VIC-3D’, Correlated Solutions Digital Image Correlation. Accessed: Sep. 07, 2024. [Online]. Available: https://www.correlatedsolutions.com/vic-3d

[82] ‘Boxer’, Nila. Accessed: Aug. 29, 2024. [Online]. Available: https://www.nila.com/boxer

[83] ‘5-Port Gigabit Easy Smart Switch’. Accessed: Aug. 29, 2024. [Online]. Available: https://www.tp-link.com/pt/business-networking/easy-smart-switch/tl-sg105e/

[84] Micro-Epsilon, ‘Laser Triangulation Displacement Sensors’, Ortenburg. Accessed: Aug. 29, 2024. [Online]. Available: http://www.micro-epsilon.pl/download/dax--optoncdt-2310--en.pdf

[85] Phoenix contact GmbH & Co. KG, ‘Primary-switched power supply unit’, Blomberg.

[86] Micro-Epsilon, ‘Operating Instructions C-Box/2A’, Ortenburg.

[87] M. Yang and C. Geng, ‘Parameter Optimization of Hyperelastic Constitutive Model of Rail Shock Absorber’, *Transp. Technol.*, vol. 10, no. 1, pp. 11–19, 2021, doi: 10.12677/OJTT.2021.101002.

Appendix

Table 16: Constants for the incident peak overpressure for Z ∈ 0.05 to 40 m/kg$^{1/3}$ for a free-air burst, adapted from [33,46,47]

K_0	K_1	C_0	C_1
−0.214362789151	1.35034249993	2.661368669	−1.69012801396
C_2	**C_3**	**C_4**	**C_5**
0.00804973591951	0.336743114941	−0.00516226351334	−0.0809228619888
C_6	**C_7**	**C_8**	
−0.00478507266747	0.00793030472242	0.0007684469735	

Table 17: Constants for the reflected peak overpressure for Z ∈ 0.05 to 40 m/kg1/3 for a free-air burst, adapted from [33]

K_0	K_1	C_0	C_1
−0.214362789151	1.35034249993	3.22958031387	− 2.21400538997
C_2	**C_3**	**C_4**	**C_5**
0.035119031446	0.657599992109	0.0141818951887	- 0.243076636231
C_6	**C_7**	**C_8**	**C_9**
− 0.0158699803158	0.0492741184234	0.00227639644004	- 0.003971262761

Table 18: Sets of input parameters for the Johnson-Holmquist material model

Variable	Description	Holmquist et al. [64]	Hidallana-Gamage et al. [65]	Zhang et al. [66]	Zhou et al. [67]
RO [kg/mm^3]	Density	2.53E-06	2.53E-06	2.53E-06	2.53E-06
G [Gpa]	Shear modulus	30.4	29.5	26.9	21
A [-]	Intact normalized strength parameter	0.93	0.93	0.75	0.7
B [-]	Fractured normalized strength parameter	0.2	0.2	0.2	0.2
C [-]	Strength parameter (for strain rate dependence)	0.003	0.003	0.035	0.035
M [-]	Fractured strength parameter (pressure exponent)	1	1	1	1
N [-]	Intact strength parameter (pressure exponent)	0.77	0.77	0.72	0.72
EPSI [-]	Quasi-static threshold strain rate	1	1	1	1
T [GPa]	Maximum tensile pressure strength	0.200	0.200	0.200	0.200
SFMAX [-]	Maximum normalized fractured strength	0.5	0.5	0.5	0.5
HEL [GPa]	Hugoniot elastic limit	5.95	5.95	1.003	4.5
PHEL [GPa]	Pressure component at the Hugoniot elastic limit	2.92	2.92	0.334	2.4
BETA [-]	Fraction of elastic energy loss converted to hydrostatic energy	1	1	1	1
D1 [-]	Parameter for plastic strain to fracture	0.043	0.043	0.043	0.043
D2 [-]	Parameter for plastic strain to fracture (exponent)	0.85	0.85	0.85	0.85
K1 [Gpa]	First pressure coefficient (equivalent to the bulk modulus)	45.4	45.4	43.2	30.5
K2 [Gpa]	Second pressure coefficient	-138	-138	-67.2	-17.3
K3 [Gpa]	Third pressure coefficient	290	290	153.2	103

Table 19: Constants for Johnson–Cook model

Variable	Description	Hooper et al. [4]
RO [kg/mm^3]	Mass density	1.10E-06
E [Gpa]	Young's modulus	0.53
PR [-]	Poisson's ratio	0.485
A [GPa]	Material Constants	0.00672
B [GPa]		0.0106
N [-]		0.303
C [-]		0.248

Table 20: Constants for Mooney-Rivlin model

Variable	Description	Yang et Geng [87]
RO [kg/mm^3]	Mass density	1.10E-06
PR [-]	Poisson's ratio	0.4997
A [-]	Material Constants	8.05E-04
B [-]		1.94E-04